

2003

Applications of POD studies and robust design to electromagnetic NDE

Zhiwei Zeng
Iowa State University

Follow this and additional works at: <https://lib.dr.iastate.edu/rtd>

 Part of the [Electrical and Electronics Commons](#)

Recommended Citation

Zeng, Zhiwei, "Applications of POD studies and robust design to electromagnetic NDE " (2003). *Retrospective Theses and Dissertations*. 1408.

<https://lib.dr.iastate.edu/rtd/1408>

This Dissertation is brought to you for free and open access by the Iowa State University Capstones, Theses and Dissertations at Iowa State University Digital Repository. It has been accepted for inclusion in Retrospective Theses and Dissertations by an authorized administrator of Iowa State University Digital Repository. For more information, please contact digirep@iastate.edu.

INFORMATION TO USERS

This manuscript has been reproduced from the microfilm master. UMI films the text directly from the original or copy submitted. Thus, some thesis and dissertation copies are in typewriter face, while others may be from any type of computer printer.

The quality of this reproduction is dependent upon the quality of the copy submitted. Broken or indistinct print, colored or poor quality illustrations and photographs, print bleedthrough, substandard margins, and improper alignment can adversely affect reproduction.

In the unlikely event that the author did not send UMI a complete manuscript and there are missing pages, these will be noted. Also, if unauthorized copyright material had to be removed, a note will indicate the deletion.

Oversize materials (e.g., maps, drawings, charts) are reproduced by sectioning the original, beginning at the upper left-hand corner and continuing from left to right in equal sections with small overlaps.

**ProQuest Information and Learning
300 North Zeeb Road, Ann Arbor, MI 48106-1346 USA
800-521-0600**

UMI[®]

Applications of POD studies and robust design to electromagnetic NDE

by

Zhiwei Zeng

**A dissertation submitted to the graduate faculty
in partial fulfillment of the requirements for the degree of
DOCTOR OF PHILOSOPHY**

Major: Electrical Engineering (Communications and Signal Processing)

**Program of Study Committee:
Lalita Udpa (Major Professor)
Satish S. Udpa
Shanker Balasubramaniam
Aleksandar Dogandžić
Huaiqing Wu
Yushi Sun**

**Iowa State University
Ames, Iowa
2003**

Copyright © Zhiwei Zeng, 2003. All rights reserved.

UMI Number: 3085961

UMI[®]

UMI Microform 3085961

**Copyright 2003 by ProQuest Information and Learning Company.
All rights reserved. This microform edition is protected against
unauthorized copying under Title 17, United States Code.**

**ProQuest Information and Learning Company
300 North Zeeb Road
P.O. Box 1346
Ann Arbor, MI 48106-1346**

**Graduate College
Iowa State University**

**This is to certify that the doctoral dissertation of
Zhiwei Zeng
has met the dissertation requirements of Iowa State University**

Signature was redacted for privacy.

Major Professor

Signature was redacted for privacy.

For the Major Program

TABLE OF CONTENTS

LIST OF FIGURES	vi
LIST OF TABLES	x
ABSTRACT	xi
CHAPTER 1. INTRODUCTION	1
1.1 Problem Statement	1
1.2 Scope of the Dissertation	4
CHAPTER 2. PRINCIPLES OF NDE TECHNIQUES	5
2.1 Introduction	5
2.2 Methods of Nondestructive Testing	6
2.2.1 Ultrasonic NDE	6
2.2.2 Radiographic NDE	7
2.2.3 Electromagnetic NDE	8
2.3 Principles of Electromagnetic NDE	8
2.3.1 Magnetic Flux Leakage Methods	8
2.3.2 Eddy Current Methods	11
2.3.3 Differential Coil Eddy Current Methods	14
2.3.4 Remote Field Eddy Current Methods	16
2.3.5 Magnetic Particle Inspection	17
2.3.6 Magneto-Optic/Eddy Current Imaging	20
CHAPTER 3. NUMERICAL MODELING IN ELECTROMAGNETIC NDE	21
3.1 Introduction	21
3.2 Boundary Value Problems	22
3.3 Numerical Methods in Electromagnetics	23
3.3.1 Integral Equation Method	23
3.3.2 Finite Element Method	25
3.3.3 Hybrid Method	25
3.3.4 Meshless Method	26
3.4 Finite Element Methods	29
3.4.1 Introduction	29
3.4.2 Governing Equations/Formulations	30
3.4.2.1 Scalar Potential Formulations	31
3.4.2.2 Vector Potential Formulations	32
3.4.3 General Procedure of Finite Element Modeling	38
3.5 Multigrid methods	47

3.5.1 Introduction	47
3.5.2 Basic Elements of Multigrid Methods	48
3.5.3 Basic Strategies of Multigrid Methods	52
3.5.3.1 Correction Methods	53
3.5.3.2 Nested Iteration Methods	55
3.5.4 Algebraic Multigrid Method	56
3.5.4.1 Setup Phase	57
3.5.4.2 Coarsening Scheme	58
3.5.4.3 Interpolation Operator	61
CHAPTER 4. POD MODELS AND TAGUCHI METHODS	63
4.1 Introduction	63
4.2 POD Models	64
4.2.1 Introduction	64
4.2.2 Sources of Variability	64
4.2.3 POD Concepts	65
4.2.4 Selection of Thresholds	67
4.2.5 POD Models	69
4.2.6 POD Evaluation Based on Functional Model	70
4.2.7 Confidence Bounds of POD Estimates	72
4.2.8 Discussions	74
4.3 Taguchi Methods	76
4.3.1 Introduction	76
4.3.2 Experiment Design	78
4.3.2.1 Fractional Factorial Design	78
4.3.2.2 Orthogonal Array	79
4.3.2.3 Inner Array and Outer Array	80
4.3.3 Analyses	81
4.3.3.1 <i>S/N</i> Analysis	82
4.3.3.2 Main Effects	83
4.3.3.3 Analysis of Variance	85
4.3.4 Response-Model Approach	89
CHAPTER 5. APPLICATION TO NATURAL GAS TRANSMISSION PIPELINE INSPECTION	91
5.1 Introduction	91
5.2 Finite Element Modeling	94
5.2.1 Formulations	94
5.2.2 Nonlinear Calculation	98
5.2.3 Procedure of Modeling	101
5.3 Application of POD Model	102
5.3.1 POD with respect to radial liftoff	102
5.3.2 POD with respect to magnetization level	105
5.3.3 POD with respect to sensor spacing	109
5.4 Application of Taguchi Methods	113

5.4.1 Design and Conduct Experiments	113
5.4.2 Analyses	117
5.4.2.1 Optimal Parameters	117
5.4.2.2 Main Effects	117
5.4.2.3 Analysis of Variance	118
CHAPTER 6. APPLICATION TO MAGNETO-OPTIC/EDDY CURRENT IMAGING	121
6.1 Introduction	121
6.2 Principles of MOI	123
6.3 Finite Element Modeling	127
6.3.1 Formulations	127
6.3.2 Simulation Results	129
6.3.2.1 Radial Crack	129
6.3.2.2 Fastener-to-Fastener Crack	130
6.3.2.3 Circumferential Crack	132
6.4 Coefficient of Skewness for MOI Applications	138
6.5 Parametric Studies on the Performance of MOI	140
6.5.1 Effect of Crack Size on Skewness	140
6.5.2 Effect of Tear Strap on Skewness	142
6.5.3 Effect of Frequency on Skewness	143
6.6 Application of POD Model	145
6.6.1 POD Calculation for MOI Applications	146
6.6.2 POD with respect to Threshold	147
6.6.3 POD with respect to Current Frequency	148
6.7 Application of Taguchi Methods	150
6.7.1 Experiment Design and Simulation	152
6.7.2 Analysis of Main Effects	154
6.7.3 Analysis of Variance	157
6.7.4 Response-Model Approach	157
CHAPTER 7 CONCLUSTIONS AND FUTURE WORK	162
7.1 Summary of Accomplishments	163
7.2 Future Work	164
BIBLIOGRAPHY	165
ACKNOWLEDGEMENTS	184

LIST OF FIGURES

Figure 2.1 A generic NDE system	5
Figure 2.2 Typical magnetization curve	9
Figure 2.3 Magnetic flux leakages	10
Figure 2.4 Impedance plane trajectory of a coil over a non-ferromagnetic specimen	13
Figure 2.5 Impedance plane trajectory of a coil over a ferromagnetic specimen	13
Figure 2.6 Differential coil eddy current tubing inspection	13
Figure 2.7 Impedance plane trajectory	13
Figure 2.8 User interface of the software for eddy current tubing inspection	15
Figure 2.9 Remote field eddy current technique in tube inspection	16
Figure 2.10 User interface of the MPI software (Visual C++)	18
Figure 2.11 User interface of the MPI software (Matlab)	19
Figure 3.1 Solution domain and boundary	22
Figure 3.2 2-D Finite elements	38
Figure 3.3 3-D Finite elements	39
Figure 3.4 Mesh generation of artificial heart valve using hexahedral elements	39
Figure 3.5 Grid levels	48
Figure 3.6 Correction methods	53
Figure 3.7 Nested iteration methods	55
Figure 3.8 Setup phase	58
Figure 3.9 Illustration of coarsening scheme	60

Figure 4.1 Decision process of NDE system	64
Figure 4.2 Typical distributions of flaw/no flaw signals	66
Figure 4.3 A typical ROC curve	67
Figure 4.4 Procedure for generating conditional probability density functions	70
Figure 4.5 Taguchi and conventional loss function	77
Figure 4.6 Representation of the Taguchi approach	77
Figure 4.7 Main effects	84
Figure 5.1 Conceptual diagram of a natural gas pipeline system	91
Figure 5.2 Cutaway view of a MFL “pig”	92
Figure 5.3 Structure of MFL pig	92
Figure 5.4 MFL defect detection	93
Figure 5.5 A typical initial magnetization curve of pipe wall	99
Figure 5.6 Procedure of finite element modeling for pipeline inspection	100
Figure 5.7 Axial component of a typical signal	101
Figure 5.8 Signal magnitudes for different liftoffs, with $B_r=1.6 T$	102
Figure 5.9 pdf of signal magnitudes with mean liftoff 0.05”	103
Figure 5.10 POD and PDF curves for different liftoffs, with $T = 280$ Gauss	104
Figure 5.11 POD curves for different liftoffs, with $PFA = 5\%$	104
Figure 5.12 ROC curve, with liftoff = 0.1”	104
Figure 5.13 Signal magnitudes for different magnetization levels, with 0.02” liftoff	106
Figure 5.14 Magnitude difference between signals with flaw and without flaw	106
Figure 5.15 pdf of signal magnitudes with mean magnetization level 1.5T	107
Figure 5.16 POD and PDF curves for different magnetization levels,	

with $T = 300$ Gauss	108
Figure 5.17 POD curves for different magnetization levels, with $PFA = 5\%$	108
Figure 5.18 ROC curve, with $B_r = 1.5T$	108
Figure 5.19 Illustration of sensor spacing and perturbation	109
Figure 5.20 1-D Signal interpolation in the circumferential direction	110
Figure 5.21 pdf of signal magnitudes with mean sensor spacing 3"	111
Figure 5.22 POD and PDF curves for different sensor spacing, with $T = 116$ Gauss	112
Figure 5.23 POD for different sensor spacing, with $PFA = 5\%$	113
Figure 5.24 ROC curve, with 3" sensor spacing	113
Figure 5.25 2-D signals in the surface perpendicular to the axial direction at the center of the flaw	116
Figure 5.26 pdf of signal magnitudes with and without flaw when $B_r = 0.8T$, sensor spacing is 1", radial liftoff equals 0.05", and zero circumferential shift	116
Figure 5.27 Main effects for S/N analysis	118
Figure 6.1 Faraday rotation effect	123
Figure 6.2 Schematic of MOI instrument	124
Figure 6.3 Induced currents, normal magnetic fields, and corresponding images	125
Figure 6.4 Geometry and mesh with radial crack	129
Figure 6.5 Predicted B_z with radial crack, crack length 5mm, frequency 3000Hz	131
Figure 6.6 Predicted binary MO images with radial crack, crack length 5mm	131
Figure 6.7 Geometry and mesh with fastener-to-fastener crack	133
Figure 6.8 Predicted B_z with fastener-to-fastener crack, current in y direction, frequency 3000Hz	134
Figure 6.9 Predicted binary MO image, current in y direction, frequency 3000Hz, threshold 35% of peak value	134

Figure 6.10 Predicted B_z with fastener-to-fastener crack, current in x direction, frequency 3000Hz	135
Figure 6.11 Predicted binary MO image, current in x direction, frequency 3000Hz, threshold 50% of peak value	135
Figure 6.12 Geometry and mesh with circumferential crack	136
Figure 6.13 Predicted B_z with 90° circumferential crack, frequency 3000Hz	136
Figure 6.14 Predicted binary MO images without crack	137
Figure 6.15 Predicted binary MO images with 45° circumferential crack	137
Figure 6.16 Predicted binary MO images with 90° circumferential crack	137
Figure 6.17 Predicted binary MO images with 180° circumferential crack	138
Figure 6.18 Effect of crack size and threshold on skewness, frequency 3000Hz	141
Figure 6.19 Tear straps under aluminum plates	141
Figure 6.20 Effect of tear strap and threshold on skewness, crack length 5mm, frequency 3000Hz	142
Figure 6.21 Effect of frequency and threshold on skewness	144
Figure 6.22 pdf of crack signal and degree of certainty of rejection	145
Figure 6.23 Predicted binary MO images with radial crack	146
Figure 6.24 Skewness and POD vs. threshold, frequency 3000Hz	149
Figure 6.25 Skewness and POD vs. threshold, frequency 6000Hz	149
Figure 6.26 Coefficients of skewness for multiple frequencies and POD vs. frequency	151
Figure 6.27 Main effects	156
Figure 6.28 Interaction A×C	156
Figure 6.29 Interaction A×D	160

LIST OF TABLES

Table 4.1 Comparison of Factorial Design and Taguchi Design	79
Table 4.2 Orthogonal Array $L_4(2^3)$	79
Table 4.3 Example of inner and outer orthogonal arrays	81
Table 4.4 Example of test data	83
Table 4.5 Main Effects	84
Table 5.1 Polynomial coefficients of the functional model for liftoff	103
Table 5.2 Polynomial coefficients of the functional model for magnetization level	107
Table 5.3 Factors and levels	114
Table 5.4 Experiment design and results	115
Table 5.5 Main Effects for S/N analysis	118
Table 5.6 ANOVA table without pooling	119
Table 5.7 ANOVA table with pooling	119
Table 6.1 Material properties	129
Table 6.2 Factors and levels	153
Table 6.3 Orthogonal array $L_9(3^4)$	153
Table 6.4. Summary of simulation results	153
Table 6.5 Main effects	156
Table 6.6 ANOVA table	157
Table 6.7 Orthogonal Array $L_{18}(2^1 \times 2^3)$	158

ABSTRACT

Numerical techniques, such as finite element methods (FEM), have been widely used in predicting defect signatures in nondestructive evaluation (NDE). The test conditions in the numerical models are deterministic in nature. However, signals generated by identical flaws are usually different under practical testing conditions. This affects the reliability of NDE methods. A considerable amount of attention has been focused towards quantifying the reliability of a variety of NDE methods, which has led to development of models for evaluating probability of detection (POD). Sources of variabilities that influence POD in NDE systems vary due to different testing modalities. POD models not only help in improving accuracy in flaw detection but also help in optimizing operational parameters. The Taguchi method, also called robust design in literature, is a well-established technique for optimizing the design parameters in an experiment.

This dissertation presents a comprehensive POD model for quasi-static electromagnetic NDE. Applications of Taguchi methods as well as POD models in magnetic flux leakage (MFL) and magneto-optic/eddy current imaging inspections are investigated in this research.

CHAPTER 1. INTRODUCTION

1.1 Problem Statement

Nondestructive evaluation (NDE) is the inspection and evaluation of a test specimen without adverse impairment of their properties and serviceability. Recent years have witnessed an increasing application of NDE techniques in industries, such as gas transmission pipelines, nuclear electric plants, airplane frames, etc. Recent advances in NDE techniques have increased the possibility of detecting potentially hazardous defects in specimens. Such defects could cause failure during service and lead to disastrous consequences. Generally most defects are in the form of cracks, which may result from environmental attack, manufacturing in welds or castings, or intensive workload.

A variety of nondestructive testing (NDT) techniques including the use of electromagnetics, ultrasonics, radiography, and thermography, have evolved to cater to various applications. A typical NDT system consists of a specimen under test, an energy source interacting with the specimen, and a receiving transducer picking up the response of the interaction. A generic NDT signal is the response of energy-material interaction. Examples of electromagnetic NDT signals include potential drop, magnetic flux leakage (MFL), impedance change of an eddy current (EC) coil, and impedance difference of a pair of differential EC coils. NDT signals are further analyzed using signal/image processing techniques and inverse techniques to obtain the location, shape, depth, and other useful information about the defect.

Magnetic flux leakage methods and eddy current methods are most commonly used electromagnetic inspection techniques. In MFL methods, an active or residual flux leakage is established by magnetizing a ferromagnetic material. The discontinuities of magnetic permeability, caused by the presence of a defect, affect the distribution of the lines of induced magnetic flux. The lines of flux are highly distorted across the crack and “leak” out of the body. The leakage field is detected by scanning the specimen’s surface with a flux-sensitive transducer or by applying magnetic powder particles onto the sample surface in magnetic particle inspection (MPI). The leakage field profile provides valuable information regarding inhomogeneities and surface or near surface cracks in the material. In EC methods, a time-varying field is established by coils or foils carrying alternating currents. Eddy current is induced in the conducting specimen. Output signals in EC inspection systems can be magnetic flux densities associated with induced EC (MOD), gradient information of magnetic flux densities (used in the integrity evaluation of artificial heart valve), or impedance difference of an absolute or a pair of differential coils (steam generator tubing inspection).

Theoretical models are needed for the training and validation of automated testing equipments as well as for studying the basic field/flaw interactions in order to obtain a fuller understanding of NDT phenomena. The modeling involves solving the partial differential equations underlying the physics of field/flaw interaction. Modeling methods solving the governing equations can be classified into two categories: analytical and numerical. Analytical approaches to modeling of electromagnetic NDT phenomena are in general not possible due to the complex shapes of defect geometries, especially in three dimensions. Simplifying assumptions are needed for obtaining solutions to these problems. Numerical modeling is becoming increasingly popular with the revolutionary advances in computer

technology and computation methods. Finite element method (FEM) is one of the most popular numerical methods and its use for characterizing NDE phenomena was pioneered by Lord [1, 2, 3]. FEM is flexible and capable of modeling complicated sample and defect geometries, as well as nonlinear material properties.

The test conditions in numerical models are deterministic in nature. However, signals generated by identical flaws are usually different under practical testing conditions due to a number of variabilities acting on the testing system. A considerable amount of attention has been focused towards quantifying the reliabilities of NDE methods, which has led to development of models for evaluating the probability of detection (POD) of a critical flaw. Sources of variabilities that influence POD in NDE systems vary due to different testing methodologies. POD models not only help in improving accuracy in flaw detection but also help in optimizing testing parameters.

Approaches for estimating the POD of a flaw can be experimental or model based. Experiment based POD evaluation is time consuming and expensive, because it requires an extensive set of measurements to obtain statistically sound estimates. Model based POD evaluation relies on computer simulation. The flaw signal and the effect of the variabilities are predicted using computer simulation.

The Taguchi method, also called robust design, is a well-established technique for optimizing the design parameters in an experiment. POD is the quality characteristic in the applications of the Taguchi method to NDE systems. The Taguchi method is a very useful tool for fractional factorial experiment/simulation design, which involves selecting a limited number of experiments that produce the most information available in full (all possible)

experiments/simulations. The influence of the sources of variabilities on the POD and optimum testing conditions can be found using robust design techniques.

Applications of the POD model and robust design to two typical NDE techniques are discussed in this dissertation. One is the natural gas transmission pipeline inspection, which is an automated and magnetostatic NDE technique; the other is the magneto-optic/eddy current imaging, which is an image-based and quasi-static electromagnetic NDE technique.

1.2 Scope of the Dissertation

This dissertation deals with the problem of optimizing electromagnetic NDE systems using numerical modeling and statistical methods. Chapter 2 introduces the different types of NDE techniques currently in practice and then focuses on the principles of electromagnetic NDE techniques. Chapter 3 discusses the finite element modeling of the electromagnetic NDE phenomena. As a fast solution scheme for numerical modeling, multigrid methods are also discussed. Chapter 4 presents the model based POD evaluation method and the Taguchi methods for experiment design and optimization. Chapter 5 discusses the applications of POD model and robust design to the natural gas transmission pipeline inspection. Chapter 6 discusses the applications of POD model and robust design to the magneto-optic/eddy current imaging technique. Chapter 7 gives some concluding remarks and identifies areas for future research activity.

CHAPTER 2 PRINCIPLES OF NDE TECHNIQUES

2.1 Introduction

In order to achieve better quality and reliability of materials and parts, a wide variety of nondestructive inspection schemes have been developed. Nondestructive inspection is particularly beneficial to industries as long as the results are reliable and the inspection is cost-effective.

Figure 2.1 shows a generic NDE system. The excitation transducer couples the energy source into the test specimen. The receiving transducer picks up the response of the field/flaw interaction and generates an output signal. The output signal is then processed, and passed through an inversion block. The inversion block performs defect characterization, which involves the estimation of defect dimensions, location, and shape.

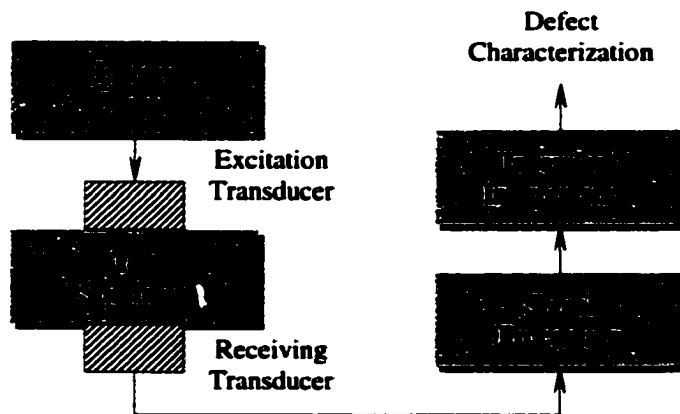


Figure 2.1 A generic NDE system

2.2 Methods of Nondestructive Testing

A variety of nondestructive testing methods are used in practice. They are generally classified according to the form of probing energy source. Some of the most commonly used NDE techniques, ultrasonic, radiographic, and electromagnetic methods, are described briefly below. Electromagnetic methods will then be discussed in more detail in the next section.

2.2.1 Ultrasonic NDE

The ultrasonic method is probably one of the oldest NDE techniques. In this method, the probing source is ultrasound, whose frequency is above the audible frequency range (10 ~ 2000 Hz). The ultrasonic waves are coupled into the test specimen via a coupling medium. In the most common situation, this energy propagates as quasi-plane-wave beams traveling through the body of the material [4]. Whenever a material discontinuity is encountered, the wave is reflected and picked up by the transducer. Hence the received signal contains reflections due to front wall, the defect, and the back wall. The time elapsed between the incident and the reflected signals is referred to as the time of flight. The amplitude of the signal provides information of the flaw size and the time of flight is a measure of the distance of the flaw from the specimen surface.

The reliability of ultrasonic methods is dependent on many factors, such as probe type and excitation frequency, couplant method, scanning surface condition, and floor coating.

2.2.2 Radiographic NDE

Radiographic NDT is widely used for finding internal, non-planar defects. The radiation source emits energy traveling in straight lines and penetrating the test specimen. The energy pattern received on the opposite side is then analyzed to obtain useful information about the condition of the test sample. The radiation source can be gamma rays or X-rays. Both of them are in the high frequency end of the spectrum with wavelengths of the order of 10^{-9} to 10^{-13} meters. Gamma rays are generated by transition of radioactive nuclei from a high energy level to a more stable lower energy level. X-rays are produced when high-speed electrons strike a target wherein the kinetic energy of the electrons is converted to electromagnetic radiation [5]. Because of the high energy levels involved X-rays and gamma rays have high penetrating power and are capable of traveling through most materials. The intensity of the beam of energy transmitted through the object is reduced according to the thickness traversed by the beam and can be expressed as

$$I_t = I_0 e^{-\lambda t} \quad (2.1)$$

where t is the thickness of the material, I_0 and I_t are the incident and transmitted energies respectively, and λ is the linear absorption coefficient that depends on the material properties. After passing through the test specimen, the radiation energy is recorded on a photographic film and analyzed to determine the condition of the specimen.

The reliability of radiographic methods is dependent on a variety of parameters, such as energy of the beam, size and shape of the beam source, source to film distance, type of film, and exposure time.

2.2.3 Electromagnetic NDE

Electromagnetic NDE methods are used widely for characterizing materials on the basis of their electric and magnetic properties (conductivity and permeability). The energy source in these methods is electric and magnetic fields. Eddy current methods have both industrial and biomedical applications, such as evaluation of condition of artificial heart valve implants [7] and magnetic resonance imaging (MRI) [8, 9, 10]. In this dissertation, the magnetostatic and quasi-static fields are used. The principles of these methods are discussed in the following section.

2.3 Principles of Electromagnetic NDE

2.3.1 Magnetic Flux Leakage Methods

Magnetic flux leakage methods are widely used for testing ferromagnetic materials, which are capable of being magnetized very strongly by an external magnetic field. When removed from the field, they retain a considerable amount of their magnetization. The constitutive relation

$$\mathbf{B} = \mu(\mathbf{B})\mathbf{H} \quad (2.2)$$

relates the magnetic flux density \mathbf{B} and the magnetic field intensity \mathbf{H} via the magnetic permeability μ . In the case of ferromagnetic materials μ is a nonlinear function of \mathbf{B} .

The magnetic property of ferromagnetic material is characterized by the magnetization curve, as shown in Figure 2.2. At any point on the curve, μ is given by the ratio B/H . As H is increased due to increase in current, from O to maximum applied field intensity H_{\max} , curve OP is produced. This curve is referred to as the virgin or initial magnetization curve. Beyond

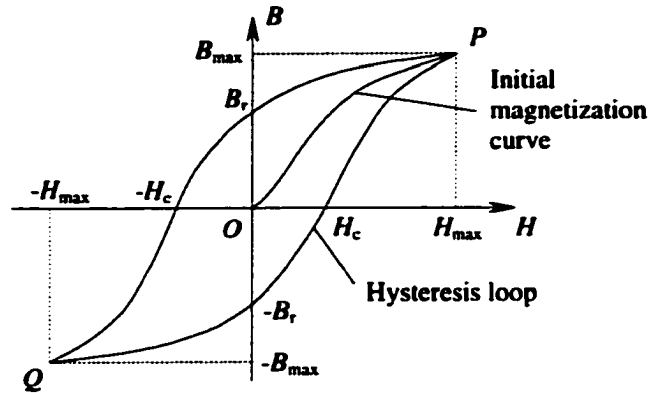


Figure 2.2 Typical magnetization curve

P , further increase in the excitation current causes the material to be saturated. If H is decreased, B does not follow the initial curve but lags behind H . If H is reduced to zero, B is not reduced to zero but to B_r , the remanent flux density. If H increases negatively, B becomes zero when H becomes $-H_c$. H_c is known as the coercive field intensity. Further variation in H to reach P gives a closed curve named hysteresis loop.

The advantage of using magnetic flux leakage methods to detect localized inhomogeneities such as surface or near-surface cracks in ferritic steels and other ferromagnetic materials, is the high degree of certainty of detection when the magnetizing fields are properly applied. The technique offers a high sensitivity when testing for small surface cracks, even on rough surfaces, than any other conventional NDE techniques.

With magnetic flux leakage methods, the object being tested is magnetized and a magnetic field is established inside the object. The distribution of the resultant lines of magnetic flux is determined by the values of magnetic permeability within the region of interest. The discontinuities of magnetic permeability, caused by the presence of a slot simulating a defect in a magnetized ferromagnetic bar, affect the distribution of the lines of

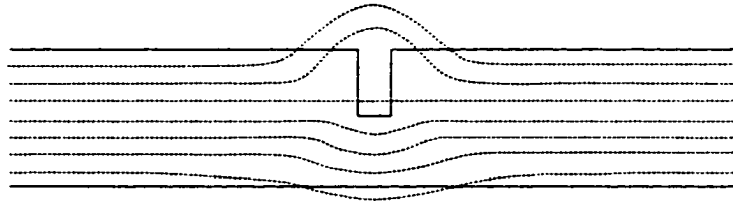


Figure 2.3 Magnetic flux leakages

induced magnetic flux in the manner as shown in Figure 2.3. North and south magnetic poles appear on the opposite sides of the slot. The lines of flux are highly distorted across the crack and “leak’ out of the body. This is known as the magnetic leakage field. It has been observed that flux leakage takes place not only at the surface containing the slot but also at the opposite surface, where the leaked flux densities have lower amplitude. Some of the fluxes pass through the slot. Flux leakage can be detected by magnetic particles, magnetic tape, or flux-sensitive coils and probes.

A typical inspection would involve magnetizing the specimen either by passing a current or using a permanent magnet or electromagnet. The specimen surface is then scanned using a Hall element probe to detect leakage fields. Another approach that is commonly used in industry is to sprinkle iron filings on the specimen and observing the pattern on the surface. This method is called the magnetic particle inspection (MPI) and will be discussed later in this chapter.

Leakage field measurement performed when the magnetizing field is present, it is called active leakage field methods. When the magnetizing current is switched off, all the magnetic domains within the specimen do not revert back to their normal randomly oriented state. This causes the walls of the defect to act as poles of a permanent magnet and a magnetic field is established across the defect. This field is referred to as the residual leakage field. Residual

leakage field can also be used to detect defects in a material. Such methods tend to be highly sensitive to surface-breaking defects.

A typical application of MFL methods is the inspection of natural gas transmission pipeline, which will be presented in Chapter 5.

2.3.2 Eddy Current Methods

Eddy current NDE techniques are based on the phenomena of electromagnetic induction. Consider a simple coil excited by an alternating current. Since the coil is carrying an alternating current, an alternating magnetic field is set up in accordance with Maxwell-Ampere Law:

$$\nabla \times \mathbf{H} = \mathbf{J} \quad (2.3)$$

in the differential form or

$$\oint_C \mathbf{H} \cdot d\mathbf{l} = \iint_S \mathbf{J} \cdot d\mathbf{S} \quad (2.4)$$

in the integral form, where the displacement currents have been neglected. If the coil is taken close to a non-ferromagnetic test specimen, the time varying field causes an electromotive force (emf) to be induced in the specimen in accordance with Maxwell-Faraday Law:

$$\nabla \times \mathbf{E} = -\frac{\partial \mathbf{B}}{\partial t} \quad (2.5)$$

in the differential form or

$$\oint_C \mathbf{E} \cdot d\mathbf{l} = -\frac{\partial}{\partial t} \iint_S \mathbf{B} \cdot d\mathbf{S} \quad (2.6)$$

in the integral form. The emf causes currents, referred to as eddy currents, to flow in the specimen. The induced current, in turn, generates a field (induced or secondary field), whose

direction is opposite to that of the primary field established by the coil, according to the Lenz's Law. This causes the net flux linking the coil to decrease. The inductance of a coil is defined as the net flux linkages per Ampere, i.e.,

$$L = \frac{N\Phi}{I} \quad (2.7)$$

where L is the inductance, N is the number of turns of the coil, Φ is the flux going through the area encircled by the coil, and I is the source current. The effective inductance of the coil decreases when it is taken close to the conducting specimen. In addition, the I^2R power loss incurred due to the flow of eddy currents in the specimen manifests itself as a net increase in the terminal resistance of the coil. Figure 2.4 illustrates this phenomenon.

In the presence of a flaw in the test specimen, the distribution of the eddy current is interrupted by the flaw. The eddy current is reduced due to the material discontinuity. The reduction of the induced eddy current leads to the reduction of the changes of the inductance and resistance of the excitation coil, as shown in Figure 2.4.

The process is more complicated when the test specimen is ferromagnetic. Accompanying the decrease in inductance due to the influence of eddy currents is an increase in inductance due to the higher permeability of the material. The latter effect is more predominant and hence when the coil is taken close to a ferromagnetic specimen the overall inductance of the coil increases along with an increase in its resistance [11]. Again, the presence of a flaw in the specimen reduces the changes in coil inductance and resistance, as shown in Figure 2.5.

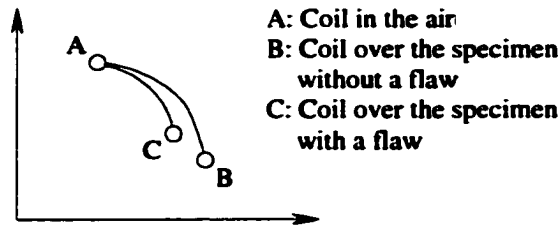


Figure 2.4 Impedance plane trajectory of a coil over a non-ferromagnetic specimen

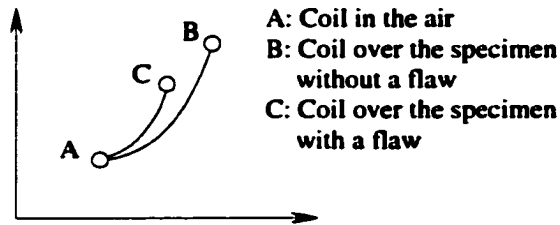


Figure 2.5 Impedance plane trajectory of a coil over a ferromagnetic specimen

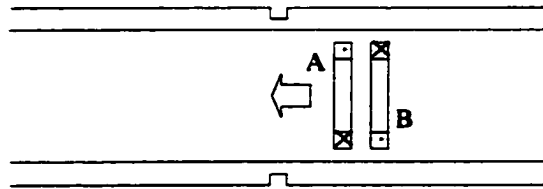


Figure 2.6 Differential coil eddy current tubing inspection

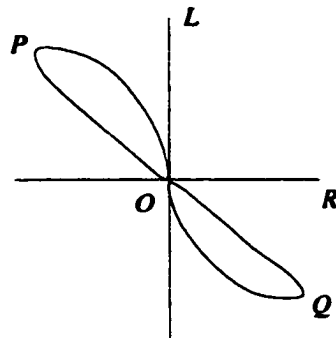


Figure 2.7 Impedance plane trajectory

2.3.3 Differential Coil Eddy Current Methods

Consider the situation as shown in Figure 2.6, where two coils A and B are located within a non-ferromagnetic tube containing a defect and connected in a differential mode, i.e., currents in the two coils have the same strength but opposite directions. When the coils are far away from the defect, the net impedance is zero (Point *O* is Figure 2.7). As the probe moves from right to left, the leading coil (Coil A in Figure 2.6) encounters the defect first. Consequently the inductance of Coil A increases and the resistance decreases. Since the fields are very local, the impedance of the trailing coil (Coil B in Figure 2.6) remains unchanged. Hence the differential impedance traces the trajectory *OP* in Figure 2.7. When Coil A leaves the defect area, and Coil B moves close to the defect, the net differential inductance decreases and the net resistance increases. When the defect is exactly in the middle of the two coils, the differential impedance becomes zero since Coils A and B are affected equally. The trajectory *PO* in Figure 2.7 is thus traced. As Coil B moves closer to the defect, the trajectory *OQ* is traced. When Coil B leaves the defect area, the trajectory *QO* is traced.

The shape and orientation of the impedance plane trajectory is determined by the defect profile, the host material electrical properties, excitation frequency, distance between the two coils, the size and shape of the coil, and the lift off, etc.

A software for predicting impedance trajectory in eddy current tubing inspection has been developed by the author of this dissertation. The software visualizes the process of moving the differential coils through the tube and obtaining the real part, imaginary part and complex trajectory of the differential impedance, as shown in Figure 2.8. An important feature of this

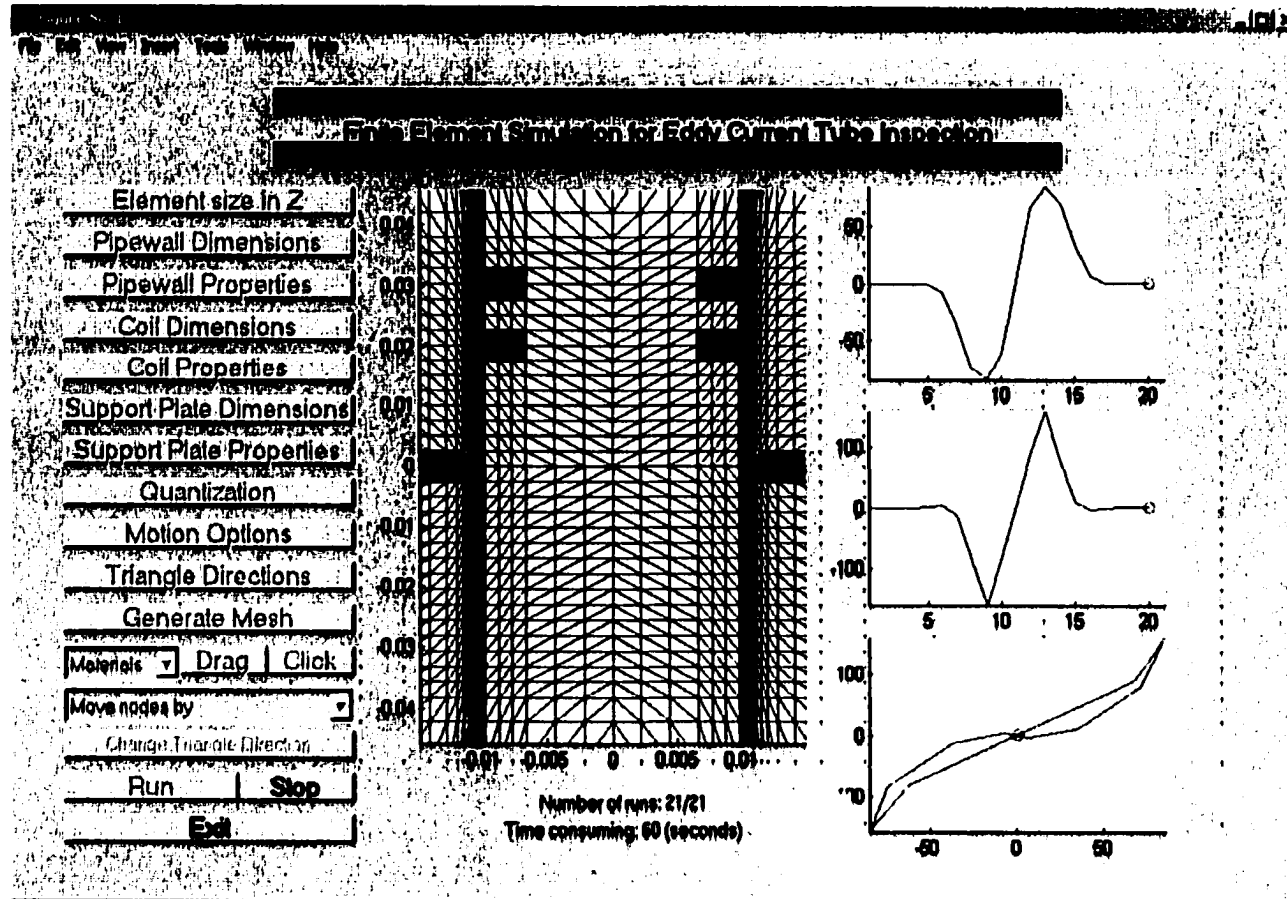


Figure 2.8 User interface of the software for eddy current tubing inspection

software is that it is very easy to change materials of the elements, move nodes and change the directions of the triangles, which makes it convenient to define indents as well as defects with arbitrary shape (regular or irregular).

2.3.4 Remote Field Eddy Current Methods

The remote field eddy current (RFEC) techniques are characterized by their high sensitivity to material discontinuities at large depths. These methods gained popularity because they are equally sensitive to any discontinuity, irrespective of its location (inner or outer diameter in the tube wall) [12]. In detecting residual stress in infrastructures, which is becoming more and more of concern, the RFEC techniques are probably more useful than conventional EC techniques.

The RFEC techniques were first introduced for tube inspection, as shown in Figure 2.9. A coil excited by an alternating current is placed in a pipe, the energy diffuses along two different paths: direct path and indirect path. It has been shown that the energy diffusing via the direct path attenuates very rapidly, because it is restricted by eddy current in the pipe wall. When a pickup coil is located at a certain distance away from the excitation coil, the

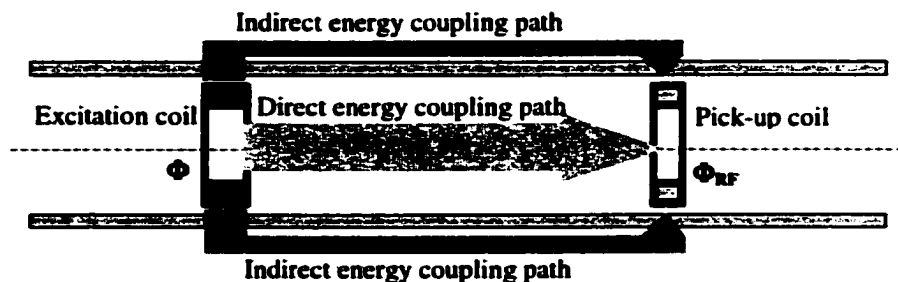


Figure 2.9 Remote field eddy current technique in tube inspection

received signal is primarily due to the energy diffusing via the indirect path. This portion of the energy passes the pipe wall twice before arriving at the pickup coil. So the received signal is closely related to the thickness, conductivity, permeability, and other wall conditions. And its phase is linearly proportional to the wall thickness.

Recently, the RFEC technique has been successfully applied to detect compressive residual stress in carbon steel specimens of flat geometries [13].

The reliabilities of the NDE techniques described above are influenced by a number of parameters. A POD model is needed to quantify the reliabilities of these techniques for a given NDE problem.

2.3.5 Magnetic Particle Inspection

Magnetic particle inspection (MPI) is a non-destructive technique for testing surface or near-surface defects in ferromagnetic materials. MPI has successful applications in a variety of industries ranging from inspection of engine components in aircrafts to steel billets during manufacturing. Major advantages of magnetic particle inspection come from its simplicity, economy, sensitivity, and accuracy [14].

MPI consists of two major steps, namely, magnetizing the sample for establishing an active or residual leakage field and detection of leakage field using magnetic powder particles. The implementation procedure for magnetic particle inspection include: careful preparation of the sample surface, such as removing grease and other substances likely to affect the mobility and visibility of the particles; magnetization of sample using either permanent magnets or electric current; application of magnetic particles onto the sample

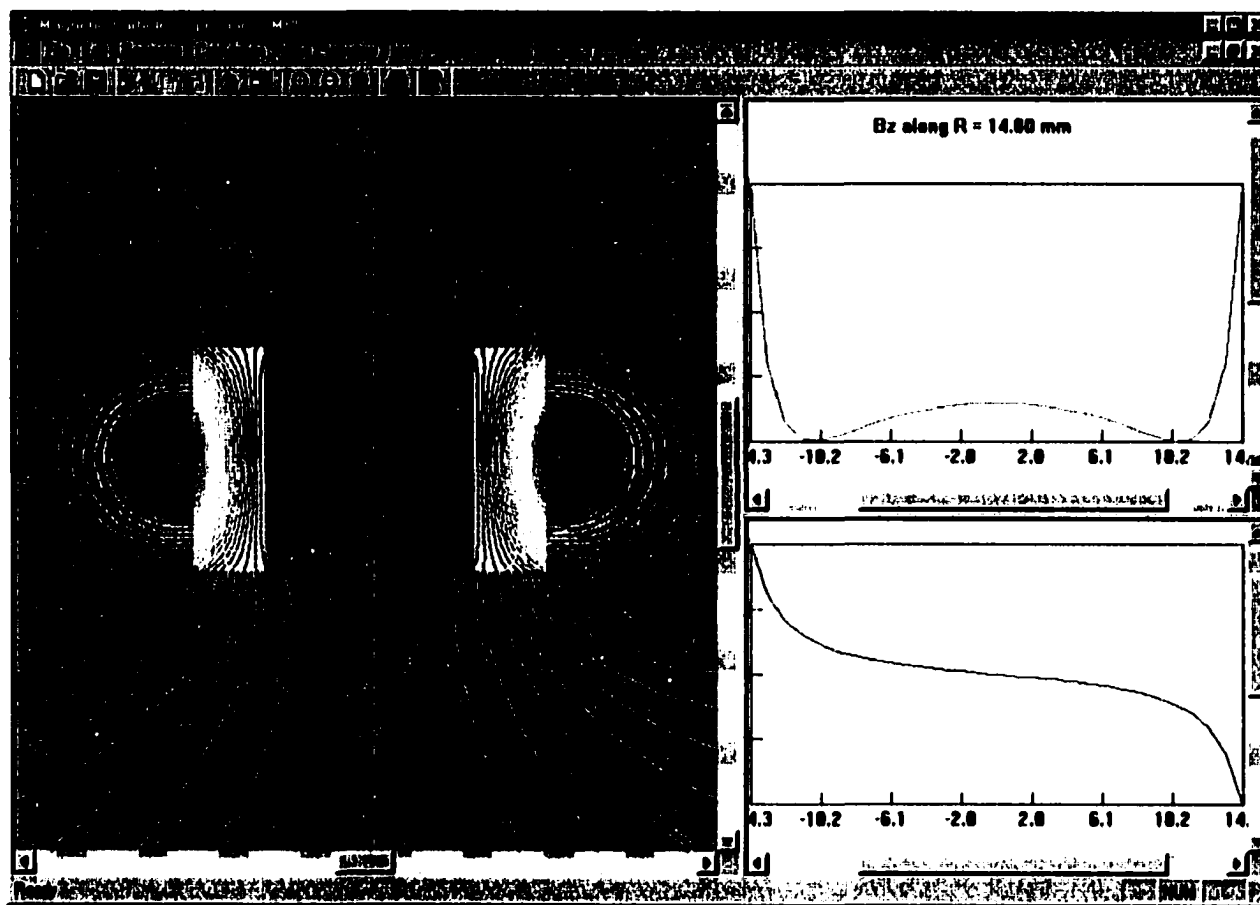


Figure 2.10 User interface of the MPI software (Visual C++)

surface using dry method or wet method; illuminating the sample surface and inspecting the particle pattern; and demagnetizing the sample [15].

The sensitivity of MPI is affected by excitation frequency, properties of magnetic powder particles and magnetization current waveforms, etc.

Two packages of MPI software (Visual C++ version for Windows platform, as shown in Figure 2.10, and Fortran/Matlab version for Unix platform, as shown in Figure 2.11) have been developed by the author of this dissertation and his colleagues to predict magnetic fluxes and study the effects of various current waveforms [17] using finite element method.

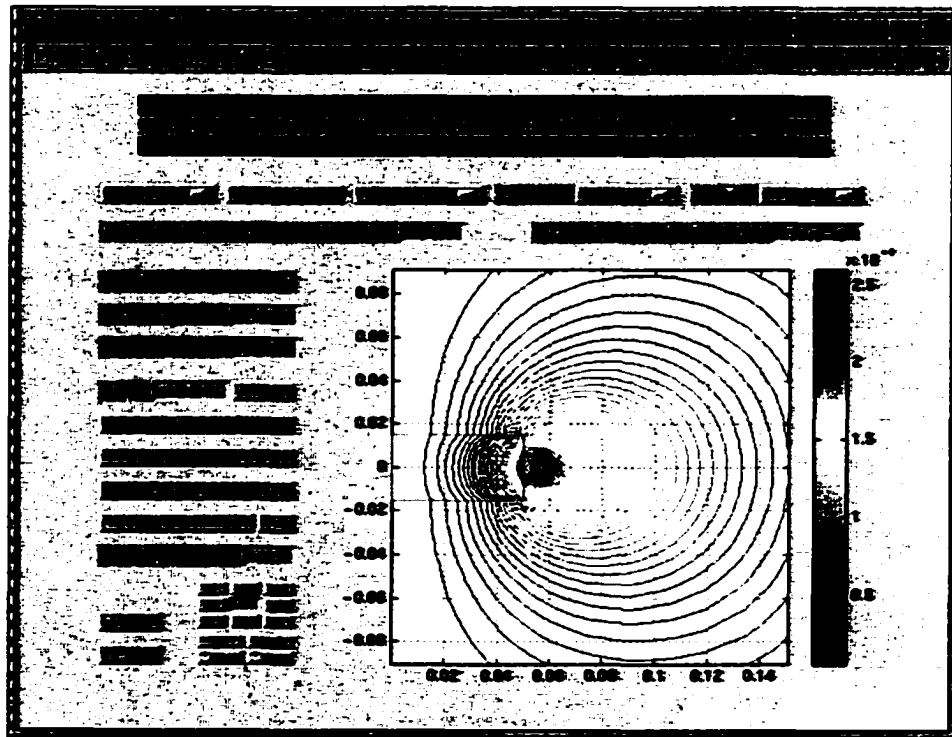


Figure 2.11 User interface of the MPI software (Matlab)

2.3.6 Magneto-Optic/Eddy Current Imaging

The Magneto-optic Imaging (MOI) is a relatively new non-destructive evaluation (NDE) technique of detecting subsurface cracks and corrosions in aircraft skin structures. The technique involves inducing eddy currents into the test specimen and detecting the magnetic flux associated with cracks in the specimen by exploiting the Faraday rotation effect. If the test specimen is homogeneous, the associated magnetic flux is tangential to the specimen surface. Anomalies in the specimen result in the generation of a normal component of the magnetic flux density. The magneto-optic sensor then produces an easy-to-interpret and real-time binary-valued image reflecting the anomalies of the magnetic fields. More details about the principles of MOI will be presented in Chapter 6.

To evaluate the performance of a MOI system under given measurement conditions, the concept of skewness is introduced to quantify the strength of the field/flaw interaction represented in the binary MO image. The skewness of binary MO image is affected by a number of test parameters such as threshold, excitation current value and frequency.

CHAPTER 3. NUMERICAL MODELING IN ELECTROMAGNETIC NDE

3.1 Introduction

Theoretical models of the forward problem are necessary for the training and validation of automated testing equipments and essential for studying the basic field/ flaw interactions in order to obtain a fuller understanding of NDT phenomena. Theoretical models generate defect signatures that are expensive to replicate experimentally. The modeling involves solving the partial differential equations underlying the physics. Inputs to the models are excitation source, specimen and defect geometries, and test conditions. Outputs of the models are predicted signals.

Modeling methods solving the governing equations can be classified into two categories: analytical and numerical. Although analytical approaches offer closed form solution, they are generally not possible to obtain largely due to the complex sample and defect geometries, especially in three dimensions. Numerical methods, however, are flexible and are capable of taking into account awkward defect geometries and nonlinearities in material properties. Numerical modeling is becoming more and more popular with advances in computer technology and computation methods.

A brief review of numerical solutions of partial differential equations is given in the following sections.

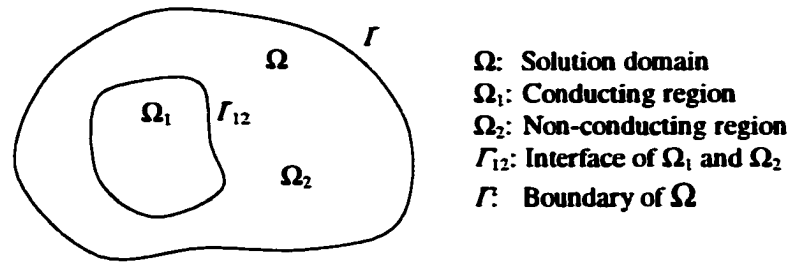


Figure 3.1 Solution domain and boundary

3.2 Boundary Value Problems

The solution of boundary value problems has been a major research activity in the mathematical modeling of physical systems for a long time. A typical boundary value problem in electromagnetic NDE can be described by a governing differential equation in a domain Ω , as shown in Figure 3.1:

$$Lu = f \quad (3.1)$$

and the boundary conditions on the boundary Γ enclosing the domain. In (3.1), L is the linear differential operator, u is the unknown, and the right hand side f is the excitation or forcing function. The boundary conditions are defined as

$$u = g \quad \text{on } \Gamma_1 \quad (3.2)$$

$$\frac{\partial u}{\partial n} = h \quad \text{on } \Gamma_2 \quad (3.3)$$

where g and h are functions defined on Γ_1 and Γ_2 respectively and $\Gamma = \Gamma_1 \cup \Gamma_2$ is the boundary of Ω . n is the outward unit normal. In electromagnetic NDE phenomena, (3.1) is generally an elliptic equation.

Ideally one desires to obtain analytical solutions of boundary value problems. However, analytical solutions are available in only a few simple situations. Over the years, various numerical methods have been developed, for solving boundary value problems in general.

3.3 Numerical Methods in Electromagnetics

In this section, four numerical methods for modeling electromagnetic phenomena will be described: integral equation (IE), finite element method (FEM), hybrid method, and meshless method.

3.3.1 Integral Equation Method

Integral Equation Method (IEM) has been successfully used in solving electromagnetic problems. An integral equation (IE) can be derived for the electric or magnetic fields or the potentials. When the unknowns are based on volume integration in the conductor the associated integral equation is called the volume integral equation, whereas when the unknowns are based on surface integration on surfaces of the conductor the associated integral equation is called the surface integral equation (or boundary integral equation). We can convert the integral equation into a matrix equation by discretizing the unknowns. In discretization when this method is employed, the surface and inside of the conductor are divided into elements.

Since Harrington first proposed the method of moments (MoM) in 1967, MoM has become one of the most important numerical methods using the integral equation approach in computational electromagnetics. The MoM transforms a functional operator equation describing the physical problem into a matrix equation by first approximating the unknown

functions by a set of expansion functions and a set of unknown coefficients. A scalar (or symmetric) product is then performed on the operator equation with selected testing functions. Consider the deterministic equation (3.1). Let f be represented by the linear combination of a set of functions $\{u_1, u_2, u_3, \dots\}$ in the domain of L :

$$u = \sum_j \alpha_j u_j \quad (3.4)$$

where the α_j are scalars to be determined. The u_j are called expansion functions or basis functions. Substituting (3.4) into (3.1) and using the linearity of L , we have

$$\sum_j \alpha_j Lu_j = f \quad (3.5)$$

Define a set of testing functions or weighting functions $\{w_1, w_2, w_3, \dots\}$ in the domain of L . Take the inner product of (3.5) with each w_i , and use the linearity of the inner product to obtain

$$\sum_j \alpha_j \langle w_i, Lu_j \rangle = \langle w_i, f \rangle \quad (3.6)$$

This set of equations can be written in matrix form as

$$L\alpha = f \quad (3.7)$$

The entries of L , α , and f are as follows:

$$L_{ij} = \langle w_i, Lu_j \rangle \quad (3.8)$$

$$\alpha_j = \alpha_j \quad (3.9)$$

$$f_j = \langle w_i, f \rangle \quad (3.10)$$

If L is nonsingular, α is given by

$$\alpha = L^{-1} f \quad (3.11)$$

The solution of u is then given by (3.4).

The integral equation method has found some applications in modeling eddy current NDE [18-21]. The major advantage of IEM is that it does not need to divide free space into many elements except in structures. However the resultant system matrix is not sparse and symmetric, as is the finite element method. Also the formulations of IEM is quite complicated if the defect geometry is complex.

3.3.2 Finite Element Method

The finite element method, also referred to as finite element analysis (FEA), has been widely used in various fields including mechanics, structural analysis, and electromagnetics.

The principle of the FEM is to replace an entire continuous domain by a number of subdomains (elements) in which the unknown function is represented by simple interpolation functions with unknown coefficients. Then a set of algebraic equations are obtained by applying the Ritz variational or Galerkin procedure. Finally, solution of the boundary value problem is achieved by solving the system of equations.

The finite element method is attractive because it has a relatively simple formulation, it is ideally suited for modeling complex geometries, and more important, it results in sparse and banded matrices that can be efficiently stored and solved.

The finite element method will be discussed in more detail later in this chapter.

3.3.3 Hybrid Method

In solving open boundary problems, which is generally the case in electromagnetic NDE, the finite element method usually leads to dividing the free space into several elements, and

hence results in solving very large-scale matrix equations. The substructure-Frontal method [22], the data base method [23, 24], and zoom-in technique [25], and the geometrical transformation method [27] have been developed to overcome this difficulty. A more popular scheme for addressing this issue is the hybrid method [28-36], which is a combination of the finite element method and the boundary integral equation method.

In the hybrid method, a fictitious boundary is introduced to enclose the structures. The finite element method is used to formulate the fields interior to the boundary. The boundary integral equation method is used to represent the fields in the exterior region. The fields in the two regions are then coupled at the fictitious boundary via field continuity conditions. The magnetic field at an arbitrary point can then be calculated using the integral equations.

Using the hybrid or FEM-IEM method, it is not necessary to model the free space; however the matrix associated with FEM-IEM formulation is full and non-symmetric.

3.3.4 Meshless Method

Although the finite element method has found wide applications in electromagnetic NDE, it is wasteful when modeling defects with very complex shapes or very small width. Particularly in solving inverse problems, it is tedious to re-mesh the geometries in each iteration. The meshless method, however, provides a possible solution to the above difficulty. In the meshless method, the domain of interest is discretized using only nodes and no elements are required. The meshless method is based on the moving least square (MLS) technique as described below.

The central idea of the MLS method is that a global approximation can be achieved by going through a “moving” process. These approximations are constructed from three

components: a weight function associated to each node, a basis, usually a polynomial one, and a set of coefficients that depend on the position. In the moving least square technique, the approximation $u^h(\mathbf{x})$ is expressed as the inner product of a vector of the polynomial basis, $\mathbf{p}(\mathbf{x})$, and a vector of the coefficients, $\mathbf{a}(\mathbf{x})$.

$$\mathbf{u}^h(\mathbf{x}) = \mathbf{p}^T(\mathbf{x})\mathbf{a}(\mathbf{x}) = \sum_{i=1}^m p_i(\mathbf{x})a_i(\mathbf{x}) \quad (3.12)$$

where $\mathbf{p}(\mathbf{x}) \in \mathbb{R}^m$, $\mathbf{a}(\mathbf{x}) \in \mathbb{R}^m$ and m is the number of monomials in the polynomial bases. The local character of the moving least square approximation, i.e., the “moving” part, arises from the dependence of \mathbf{a} on \mathbf{x} . (3.12) can be viewed as a generalization of the traditional least square approximation in which the vector \mathbf{a} is not a function of \mathbf{x} .

In order to determine the form of $\mathbf{a}(\mathbf{x})$, a weighted discrete error norm,

$$J(\mathbf{x}) = \sum_{I=1}^n w_I(\mathbf{x}) \left[\mathbf{p}^T(\mathbf{x}_I)\mathbf{a}(\mathbf{x}) - u_I \right]^2 \quad (3.13)$$

is constructed and minimized. Here, $w_I(\mathbf{x})$ denotes the weight function, $w_I(\mathbf{x}) \equiv w(\mathbf{x} - \mathbf{x}_I)$, associated with node I , and the quantity in the brackets is the difference between the local approximation at node I and the data at node I , u_I ; n is the number of nodes in the support of $w_I(\mathbf{x})$. (3.13) can be viewed as a generalization of the familiar least square error norm, in which the weight functions are unity throughout the entire domain. Compact support of the weight functions give the moving least square method its local character.

The minimization of (3.13),

$$\frac{\partial J(\mathbf{x})}{\partial \mathbf{a}(\mathbf{x})} = \mathbf{0} \quad (3.14)$$

results in the linear system

$$A(\mathbf{x})\mathbf{a}(\mathbf{x}) = B(\mathbf{x})\tilde{\mathbf{u}} \quad (3.15)$$

where $\tilde{\mathbf{u}}$ is a vector containing the nodal data, $\tilde{\mathbf{u}} = [u_1, u_2, \dots, u_n]$, and

$$A(\mathbf{x}) = \sum_{l=1}^n w_l(\mathbf{x}) \mathbf{p}(\mathbf{x}_l) \mathbf{p}^T(\mathbf{x}_l) \quad (3.16)$$

$$B(\mathbf{x}) = [w_1(\mathbf{x})\mathbf{p}(\mathbf{x}_1) \ w_2(\mathbf{x})\mathbf{p}(\mathbf{x}_2) \ \dots \ w_n(\mathbf{x})\mathbf{p}(\mathbf{x}_n)] \quad (3.17)$$

where $A(\mathbf{x}) \in \mathbb{R}^{m \times m}$, $B(\mathbf{x}) \in \mathbb{R}^{m \times n}$. Substitution of the solution of (3.15) into the global approximation (3.12), completes the least square approximation.

$$u^h(\mathbf{x}) = \underbrace{\mathbf{p}^T(\mathbf{x}) A^{-1}(\mathbf{x}) B(\mathbf{x})}_{N^k(\mathbf{x})} \tilde{\mathbf{u}} \quad (3.18)$$

Here, the spatial dependence has been lumped into one row matrix, $N^k(\mathbf{x})$, and the approximation therefore takes the form of a product of a matrix of shape functions with a vector of nodal data. The superscript k is the order of the polynomial basis.

In comparison with the FEM, which naturally handles the physical discontinuities at interfaces, a plain use of meshless methods is smoothing the solution because of its higher regularity [42]. [38, 42, 44] present several schemes dealing with interface discontinuity, such as the Lagrange multipliers method.

Another major difficulty in the implementation of meshless method is the non-interpolatory character of the approximation, that is, the approximation does not pass through the nodal parameter values. As a consequence, the imposition of boundary conditions on the dependent variable is quite awkward. Several approaches [38, 42, 44, 48, 50] have been used to solve this problem, one of which couples the meshless method to the FEM.

The meshless method, particularly in the current state of development, is still not as fast as the finite element method. Therefore, it is desirable to use the meshless model only in

those sub-domains where their greater versatility is needed. Since the MLS formulation becomes a finite element approximation when the domain of influence coincides with the element, by setting the domains of influence in the meshless domain adjacent to the finite element domain to coincide with virtual elements, a consistent coupling can be developed. Belytschko et al. used blending functions to combine the finite element and meshless approximations on the interface zone [42, 48]. Liu et al. combined finite element and meshless approximations in the interface domain by enforcing that the approximation be consistent [50].

The two major methods of discretization in the numerical implementation of the meshless method are collocation method and Galerkin method. In collocation method, the discrete equations are obtained by forcing the equation on all the nodes, except for the boundary nodes. Similar to the finite element method, the implementation of the Galerkin scheme in the meshless method requires a weak form or variational principle and is referred to as the element-free Galerkin (EFG) method.

The element-free Galerkin method has been successfully used in eddy current inspection by Xuan et al [56, 57].

3.4 Finite Element Methods

3.4.1 Introduction

The finite element method is a numerical technique for obtaining approximate solutions to boundary value problem. Since it was first proposed in the 1940s, the method has been developed and applied very extensively to structural analysis and other fields.

The finite element method was popularized in the area of electromagnetic NDT by Lord et al. Lord and Hwang first used the FEM for modeling active magnetic leakage files [1, 2]. Lord, Yen [3] and Udpa [62] developed a two-dimensional model for predicting the residual leakage fields. Lord and Palanisamy [63] developed a two dimensional axisymmetric model to study eddy current phenomena. Lord and Ida [66, 67] developed a three-dimensional FE model for magnetostatic and eddy current NDT problems.

3.4.2 Governing Equations/Formulations

The Maxwell's equations in differential form are given by

$$\nabla \times \mathbf{E} = -\frac{\partial \mathbf{B}}{\partial t} \quad (3.19)$$

$$\nabla \times \mathbf{H} = \mathbf{J}_c + \mathbf{J} + \frac{\partial \mathbf{D}}{\partial t} \quad (3.20)$$

$$\nabla \cdot \mathbf{B} = 0 \quad (3.21)$$

$$\nabla \cdot \mathbf{D} = \rho \quad (3.22)$$

with the constitutive relations:

$$\mathbf{B} = \mu \mathbf{H} \quad (3.23)$$

$$\mathbf{D} = \epsilon \mathbf{E} \quad (3.24)$$

$$\mathbf{J} = \sigma \mathbf{E} \quad (3.25)$$

In Equations (3.19) through (3.25),

\mathbf{E} = Electric field intensity (volts/meter)

\mathbf{D} = electric flux density (coulombs/square meter)

\mathbf{H} = magnetic field intensity (amperes/meter)

B = magnetic flux density (webers/square meter)

J_s = source current density (amperes/square meter)

J = conduction current density (amperes/square meter)

ρ = electric charge density (coulombs/cubic meter)

μ = permeability (henrys/peter)

ϵ = permittivity (farads/meter)

σ = conductivity (siemens/meter)

3.4.2.1 Scalar Potential Formulations

In the electrostatic problem, (3.19) reduces to

$$\nabla \times \mathbf{E} = \mathbf{0} \quad (3.26)$$

which means that the electric field intensity is curl free. So \mathbf{E} can be expressed as

$$\mathbf{E} = -\nabla \phi \quad (3.27)$$

where ϕ is any scalar function. With appropriate boundary conditions applied, ϕ is equivalent to the scalar potential in electric field. In the charge free region, (3.22) reduces to

$$\nabla \cdot \mathbf{D} = 0 \quad (3.28)$$

Substituting (3.27) together with (3.24) into (3.28), the following Laplacian equation is obtained.

$$\nabla^2 \phi = 0 \quad (3.29)$$

(3.29) is the governing equation of electrostatic problem in terms of the electric scalar potential.

In the magnetostatic problem, (3.20) in current free region reduces to

$$\nabla \times \mathbf{H} = 0 \quad (3.30)$$

Here, the magnetic field intensity is curl free, and can be expressed as

$$\mathbf{H} = -\nabla \psi \quad (3.31)$$

where ψ is called the magnetic scalar potential. Substituting (3.31) together with (3.23) into (3.21), the following Laplacian equation is obtained.

$$\nabla^2 \psi = 0 \quad (3.32)$$

(3.32) is the governing equation of magnetostatic problem in terms of the magnetic scalar potential.

3.4.2.2 Vector Potential Formulations

A - v Formulation

From (3.21), the magnetic flux density is divergence free and can be expressed as the curl of a vector, i.e.,

$$\mathbf{B} = \nabla \times \mathbf{A} \quad (3.33)$$

where \mathbf{A} is called the magnetic vector potential. The magnetic field intensity can also be expressed in terms of \mathbf{A} , as

$$\mathbf{H} = \frac{1}{\mu} \nabla \times \mathbf{A} \quad (3.34)$$

Substituting (3.33) into the Faraday's Law (3.19), we get

$$\nabla \times \mathbf{E} = -\nabla \times \frac{\partial \mathbf{A}}{\partial t} \quad (3.35)$$

or

$$\nabla \times \left(\mathbf{E} + \frac{\partial \mathbf{A}}{\partial t} \right) = 0 \quad (3.36)$$

Then the electric field intensity can be expressed as

$$\mathbf{E} = -\frac{\partial \mathbf{A}}{\partial t} - \nabla \phi \quad (3.37)$$

(3.37) tells us that the electric field intensity \mathbf{E} can be expressed in terms of the magnetic vector potential \mathbf{A} and the scalar function ϕ . Substituting (3.37) into (3.25) leads to

$$\mathbf{J} = -\sigma \frac{\partial \mathbf{A}}{\partial t} - \sigma \nabla \phi \quad (3.38)$$

In the conventional eddy current testing where the excitation frequency is less than a few megacycles per second, the displacement current density ($\partial \mathbf{D} / \partial t$) is much smaller than the conduction current density and can be neglected for all practical purposes. That is, (3.20) reduces to

$$\nabla \times \mathbf{H} = \mathbf{J}_s + \mathbf{J} \quad (3.39)$$

The following governing equation for eddy current problem is obtained by substituting (3.34) and (3.38) into (3.39):

$$\nabla \times \left(\frac{1}{\mu} \nabla \times \mathbf{A} \right) = \mathbf{J}_s - \sigma \frac{\partial \mathbf{A}}{\partial t} - \sigma \nabla \phi \quad (3.40)$$

Using the vector identity

$$\nabla \times \nabla \times \mathbf{A} = \nabla(\nabla \cdot \mathbf{A}) - \nabla^2 \mathbf{A} \quad (3.41)$$

with the Coulomb gauge

$$\nabla \cdot \mathbf{A} = 0 \quad (3.42)$$

(3.40) reduces to

$$\frac{1}{\mu} \nabla^2 \mathbf{A} = -\mathbf{J}_s + \sigma \frac{\partial \mathbf{A}}{\partial t} + \sigma \nabla \phi \quad (3.43)$$

if the permeability is piecewise constant.

In (3.43), there are four scalar unknowns: ϕ and three components of \mathbf{A} , but only three scalar equations: one for each component of \mathbf{A} . So one more equation is needed for solving the problem. Commonly, the divergence-free condition of \mathbf{J}

$$\nabla \cdot \mathbf{J} = 0 \quad (3.44)$$

is chosen. Substituting (3.38) into (3.44), we have

$$\nabla \cdot \sigma \left(\frac{\partial \mathbf{A}}{\partial t} + \nabla \phi \right) = 0 \quad (3.45)$$

(3.43) and (3.45) together are the governing equations for quasi-static problem, and is called the \mathbf{A} , ϕ - \mathbf{A} formulation or \mathbf{A} , ν - \mathbf{A} formulation, or \mathbf{A} , ν formulation for short.

In the case of time harmonic variation, (3.43) and (3.45) become

$$\frac{1}{\mu} \nabla^2 \mathbf{A} = -\mathbf{J}_s + \sigma j \omega \mathbf{A} + \sigma \nabla \phi \quad (3.46)$$

$$\nabla \cdot \sigma (j \omega \mathbf{A} + \nabla \phi) = 0 \quad (3.47)$$

where ω is the angular frequency.

\mathbf{A}^* Formulation

Defining the modified vector potential \mathbf{A}^* as

$$\mathbf{A}^* = \mathbf{A} + \int \nabla \phi dt \quad (3.48)$$

(3.43) reduces to

$$\frac{1}{\mu} \nabla^2 \mathbf{A}^* = -\mathbf{J}_s + \sigma \frac{\partial \mathbf{A}^*}{\partial t} \quad (3.49)$$

or

$$\frac{1}{\mu} \nabla^2 \mathbf{A}^* = -\mathbf{J}_s + \sigma j \omega \mathbf{A}^* \quad (3.50)$$

for time harmonic variation. (3.49) is called the \mathbf{A}^* formulation. With both formulations (3.43) and (3.49), the magnetic flux density \mathbf{B} is the same:

$$\mathbf{B} = \nabla \times \mathbf{A}^* = \nabla \times \mathbf{A} \quad (3.51)$$

The advantages of the \mathbf{A}^* formulation are that it reduces the matrix size and it is simpler to implement. However, by defining (3.48), (3.37) becomes

$$\mathbf{E} = -\frac{\partial \mathbf{A}^*}{\partial t} \quad (3.52)$$

The modified vector potential \mathbf{A}^* takes over a special feature of the electric field intensity \mathbf{E} . That is, \mathbf{A}^* is continuous only in the tangential directions of the interface of two materials with different conductivity and has no normal continuity. Error, or non-physical, solutions have been found at some local places where conductor surfaces have complex shapes, such as concave corners.

A - v - ψ Formulation

Besides the \mathbf{A}^* formulation, another way to save computer resource requirements is to minimize the region where the A - v formulation is applied. And scalar potentials, the total scalar potential ψ or the reduced scalar potential, or both, are utilized where the curl free condition of \mathbf{H} is met.

The solution domain Ω is partitioned into two regions, as shown in Figure 3.1: Ω_1 , including all conductors where $A - v$ is applied, and Ω_2 , the non-conducting region where only ψ is defined. The governing equations for the two regions are

$$\Omega_1: \quad \frac{1}{\mu} \nabla^2 A = -J_s + \sigma \frac{\partial A}{\partial t} + \sigma \nabla \phi \quad (3.53)$$

$$\nabla \cdot \sigma \left(\frac{\partial A}{\partial t} + \nabla \phi \right) = 0 \quad (3.54)$$

$$\Omega_2: \quad \nabla \cdot \mu \nabla \psi = 0 \quad (3.55)$$

(3.55) is obtained by substituting (3.31) and (3.23) into (3.21). (3.53) through (3.55) are called the $A - v - \psi$ formulation.

$T - \Omega$ Formulation

Instead of using the combination of the magnetic vector potential A , and the electric scalar potential ϕ , the $T - \Omega$ formulation is an alternative approach for representing electromagnetic problems. T is called the electric vector potential and Ω is a scalar function.

From the divergence free condition of J (3.44), J can be expressed as

$$J = \nabla \times T \quad (3.56)$$

Comparing (3.56) with the Ampere's law

$$\nabla \times H = J \quad (3.57)$$

we can write

$$H = T - \nabla \Omega \quad (3.58)$$

Replacing E by J/σ , and substituting into (3.19), together with (3.56) and (3.58), we have

$$\nabla \times \frac{1}{\sigma} \nabla \times \mathbf{T} = -\mu \frac{\partial}{\partial t} (\mathbf{T} - \nabla \Omega) \quad (3.59)$$

Use the vector identity (3.41) and the Coulomb gauge

$$\nabla \cdot \mathbf{T} = 0 \quad (3.60)$$

(3.59) reduces to

$$\frac{1}{\sigma} \nabla^2 \mathbf{T} = \mu \frac{\partial}{\partial t} (\mathbf{T} - \mu \nabla \Omega) \quad (3.61)$$

Similar to the $\mathbf{A} - \nu$ formulation, one more scalar equation is needed to complete the four variable per node formulation. The divergence-free condition of the magnetic flux density \mathbf{B} (3.21) is used. Substituting (3.58) and (3.23) into (3.21), we get

$$\nabla \cdot \mu (\mathbf{T} - \nabla \Omega) = 0 \quad (3.62)$$

(3.61) and (3.62) are called the $\mathbf{T} - \Omega$ formulation.

Theoretically, Ω could be any scalar function with first order of continuity. However, the best choice is $\Omega = \psi$, because it can be extended to the air region without any discontinuity on the interfaces.

The major advantage of the $\mathbf{T} - \Omega$ formulation over the $\mathbf{A} - \nu$ and $\mathbf{A} - \nu - \psi$ formulations is that a continuous scalar potential Ω is used in the whole solution domain. This makes the $\mathbf{T} - \Omega$ formulation simpler than the $\mathbf{A} - \nu - \psi$ formulation because one less potential is used there and no special condition is needed at the interfaces.

Observing (3.56), one can directly obtain \mathbf{J} once \mathbf{T} is solved. So the $\mathbf{T} - \Omega$ formulation is recommended if \mathbf{J} is the quantity of interest to be computed. From (3.33), \mathbf{B} can be directly obtained once \mathbf{A} is solved. Therefore, the $\mathbf{A} - \nu$ or $\mathbf{A} - \nu - \psi$ formulation is preferred if \mathbf{B} is of interest.

3.4.3 General Procedure of Finite Element Modeling

Step 1. Domain Discretization

Domain discretization may be the most important step in any finite element analysis because the manner of domain discretization affects the computer storage requirements, the computation time, and the accuracy of the numerical results [68]. In this step, the whole solution domain is subdivided into a finite number of small domains, referred to as subdomains or elements, denoted as Ω^e ($e = 1, 2, 3, \dots, M$) where M is the number of subdomains.

Figure 3.2 shows three types of elements used in 2-D FE modeling: triangular, rectangular, and quadrilateral elements. Triangular elements are preferred since they can be used to discretize any arbitrary geometry. When using triangular elements, one should avoid the generation of narrow elements (with small inner angle), because the error in finite element solution is inversely proportional to the sine of the smallest inner angle [68]. The advantage of the rectangular element is that the corresponding shape function (which will be discussed later) is simple. Rectangular element is widely used in edge-based FEM.

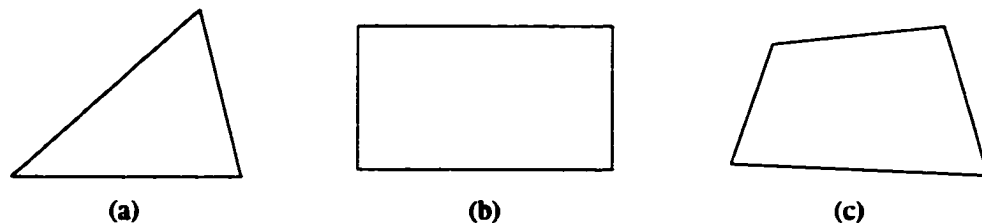


Figure 3.2 2-D Finite elements
(a) Triangular element (b) Rectangular element (c) quadrilateral element

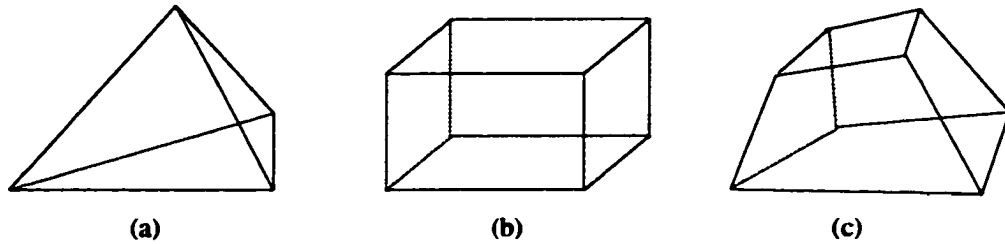


Figure 3.3 3-D Finite elements
 (a) Tetrahedral element (b) Rectangular brick element (c) Hexahedral element

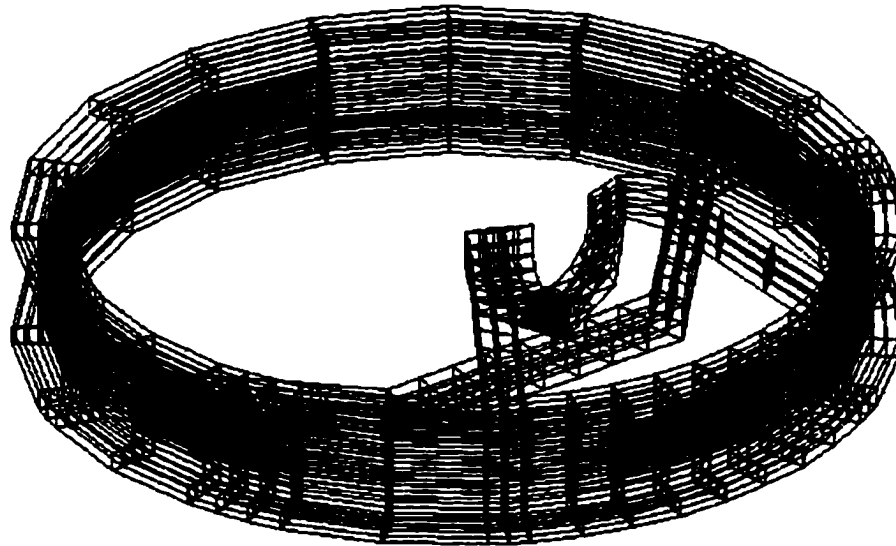


Figure 3.4 Mesh generation of artificial heart valve using hexahedral elements
 (only the metal part is shown)

Rectangular element and quadrilateral element can be transformed into square element via coordinate transformation.

The commonly used elements in 3-D applications are tetrahedral element, rectangular brick element, and hexahedral element, as shown in Figure 3.3. The tetrahedral element is, of course, most versatile in discretizing complex geometries. The rectangular brick element has simple shape functions. The hexahedral element can be transformed into cubic element via

coordinate transformation. Figure 3.4 is an example of mesh generation of artificial heart valve using hexahedral elements.

In each of the above element, nodes are numbered both globally and locally. A connectivity table is built to maintain correspondence between elements and nodes.

To save computational resource requirements as well as obtain desired computation accuracy, mesh density varies over the solution domain. Mesh density is higher in regions of large field gradient and lower in regions of slowly varying fields.

Step 2. Selection of Basis Functions

The second step of a FEA is to select a basis, trial, expansion, or an interpolation function that provides an approximation of the unknown solution within an element. Usually the polynomial function is chosen, because it is easy to differentiate and integrate and it can approximate any function if the polynomial contains enough terms. In most cases, a linear (first order) polynomial

$$u(x, y) = \alpha_1 + \alpha_2 x + \alpha_3 y \quad (3.63)$$

in 2-D case or

$$u(x, y) = \alpha_1 + \alpha_2 x + \alpha_3 y + \alpha_4 z \quad (3.64)$$

in 3-D case is used. In the above two equations, α_1 , α_2 , α_3 , (and α_4 in 3-D case) are coefficients to be determined. It is assumed that the potential varies linearly depending on the coordinates and the field strength is uniform in an element.

Substituting the nodal values and coordinates on the vertices into (3.63) or (3.64) and solving the resultant set of equations, the coefficients are determined. The expression for the unknown solution in element e is given by

$$u(x, y) = \sum_{k=1}^n N_k^e u_k^e = \{N^e\}^T \{u^e\} \quad (3.65)$$

where n is the number of nodes in the element, u_k^e the value of u at node k of the element, N_k^e the interpolation function, also referred to as shape function. (3.65) simply states that the function u within an element is a linear combination of the shape functions and the nodal values on the vertices of the element.

Step 3. Formulation of Local System of Equations

The local system of equations can be formulated via either the Ritz variational method or the Galerkin method.

Formulation via Ritz Variational Method

In the Ritz variational method, the boundary value problem is formulated in terms of a variational expression (functional), whose minimum corresponds to the governing differential equation under the given boundary conditions.

Define the inner product as

$$\langle u, w \rangle = \int_{\Omega} u w^* d\Omega \quad (3.66)$$

in which $*$ denotes the complex conjugate. It has been shown that if the operator L in (3.1) is self-adjoint, i.e.,

$$\langle Lu, w \rangle = \langle u, Lw \rangle \quad (3.67)$$

and positive definite, i.e.,

$$\langle Lu, u \rangle = \begin{cases} > 0 & u \neq 0 \\ = 0 & u = 0 \end{cases} \quad (3.68)$$

then the solution to (3.1) can be obtained by minimizing the functional

$$F(\hat{u}) = \frac{1}{2} \langle L\hat{u}, \hat{u} \rangle - \frac{1}{2} \langle \hat{u}, f \rangle - \frac{1}{2} \langle f, \hat{u} \rangle \quad (3.69)$$

with respect to \hat{u} , where \hat{u} denotes the trial function. Substituting (3.65) into (3.69), we obtain

$$F = \frac{1}{2} \{u^e\}^T \int_{\Omega} \{N^e\}^T \{N^e\} d\Omega \{u^e\} - \{u^e\}^T \int_{\Omega} \{N^e\} f d\Omega \quad (3.70)$$

To minimize the functional we let the partial derivatives of (3.70) with respect to u_i^e vanish, which results in a set of linear algebraic equations

$$\begin{aligned} \frac{\partial F}{\partial u_i^e} &= \frac{1}{2} \sum_{k=1}^n u_k^e \int_{\Omega} (N_i^e L N_j^e + N_j^e L N_i^e) d\Omega - \int_{\Omega} N_i^e f d\Omega \\ &= 0 \quad i = 1, 2, \dots, n \end{aligned} \quad (3.71)$$

in which n is the number of vertices of element e . (3.71) can also be written in matrix form

$$[s^e] \{u^e\} = \{p^e\} \quad (3.72)$$

where $[s^e]$, $\{u^e\}$, and $\{p^e\}$ are local system matrix (or stiffness matrix), unknown vector, and local load vector respectively, with the elements in $[s^e]$ given by

$$s_{ij} = \frac{1}{2} \int_{\Omega} (N_i^e L N_j^e + N_j^e L N_i^e) d\Omega \quad (3.73)$$

and the elements in $\{p^e\}$ given by

$$b_i = \int_{\Omega} N_i^e f d\Omega \quad (3.74)$$

Obviously $[S^e]$ is a symmetric matrix. Using the self-adjoint property of L , S_{ij} can be written as

$$S_{ij} = \int_{\Omega} N_i^e L N_j^e d\Omega \quad (3.75)$$

(3.72) is the local system of equations and the entries can be evaluated using Gaussian quadrature.

Formulation via Galerkin Method

Galerkin method is a member of the family of weighted residual methods, for calculating approximate solution of differential equations. Assuming \hat{u} to be an approximate solution of (3.1), then the residual is defined as

$$r = L\hat{u} - f \quad (3.76)$$

The best approximation of u reduces the residual to the least value at all points in the solution domain or subdomain in FEM. Hence the weighted residual methods enforce the condition

$$R_i^e = \int_{\Omega} w_i^e r d\Omega \quad (3.77)$$

where R_i^e is the weighted residual integral of element e and w_i^e is a chosen weighting function. In Galerkin method, the weighting function is selected to be the same as those used for the expansion of the approximate solution. That is,

$$w_i^e = N_i^e \quad i = 1, 2, \dots, n \quad (3.78)$$

So (3.77) becomes

$$R_i^e = \int_{\Omega} (N_i^e L \{N^e\} \{u^e\} - N_i^e f) d\Omega \quad i = 1, 2, \dots, n \quad (3.79)$$

This leads to the same local matrix equation as given in (3.72). The matrix $[S^e]$ is symmetric if the operator L is self-adjoint.

Step 4. Formulation of Global System of Equations

After obtaining all the elemental matrix equations, the element matrix equation at every node of the solution domain are assembled to form a system (or global) matrix equation

$$[S]\{u\} = \{b\} \quad (3.80)$$

where $[S]$ is a sparse, banded, symmetric, and positive definite matrix with order $N \times N$, with N denoting the total number of nodes in the solution domain. $[S]$ is referred to as system matrix, global matrix, or stiffness matrix. $\{u\}$ is the unknown column vector of order N . $\{b\}$, a column vector with order N , is called the global load vector.

The procedure of assembling local matrix and vector into global matrix and vector is quite straightforward. It can be verified that

$$[S] = \sum_{e=1}^M [\bar{S}^e] \quad (3.81)$$

and

$$\{b\} = \sum_{e=1}^M \{\bar{b}^e\} \quad (3.82)$$

where $[\bar{S}^e]$ and $\{\bar{b}^e\}$ are augmented or expanded from $[S^e]$ and $\{b^e\}$ respectively, M is the total number of elements in the domain. The general rule for this process is to add S_{ij}^e to $S_{np(e,i),np(e,j)}$ and add b_i^e to $b_{np(e,i)}$, where np is the connectivity array with $np(e,i)$ denotes the global node index of the i th node of element e .

Step 5. Imposition of Boundary Conditions

The field equations, formulated in terms of finite elements in (3.80), can be solved provided a correct set of boundary conditions is specified. The boundary conditions include Dirichlet boundary conditions (3.2) and Neumann boundary conditions (3.3). In the finite element analysis of magnetostatic or quasi-static problems, the Neumann boundary conditions are natural (or implicit) in the formulation in (3.80) and need not to be specified [66]. It is convenient to specify Dirichlet boundary conditions since (3.80) can accommodate the function value easily.

A commonly used technique of imposing Dirichlet boundary conditions is called blasting technique. This technique involves the replacement of the diagonal entry in the stiffness matrix corresponding to a boundary node by a very large number and the multiplication of the corresponding entry in the load vector with the same large number. This will ensure that the off diagonal terms in that row can be neglected as they are very small compared to the diagonal entry and hence the boundary node is tied down to the boundary value specified.

Step 6. Solution of the System of Equations

With a correct set of boundary conditions specified, the global system of equations is ready to be solved for unknowns. Two classes of methods: direct methods and iterative methods, are available to solve the linear algebraic equations.

The direct methods are usually based on Gaussian elimination (GE) and they yield an exact solution (theoretically) of the system. The fact that the stiffness matrix is symmetric and banded tells us that only a fixed band of the matrix entries located around the main

diagonal need to be stored. Hence the LU factorization algorithms incorporating banded matrix storage are popular in the finite element analysis. Proper numbering scheme is necessary to make the bandwidth as small as possible. Some FEM codes use Cholesky decomposition with the skyline storage scheme.

The direct methods often do not fully exploit the sparsity of the system matrix. Moreover the direct methods for sparse systems are difficult to adapt to parallel-architecture computers. A wide variety of iterative methods have been developed, which start with an initial guess and then minimize the residual error through an iterative procedure. Usually they yield an approximate solution with a prescribed accuracy. The iterative methods are suitable for solving the system of equations in FEM, especially in 3-D case. Commonly used iterative methods are Jacobi iteration, Gauss-Seidel iteration, and conjugate gradient (CG) methods. To obtain good accuracy, the grid or mesh is typically made very fine, which in turn make computation expensive. Multigrid methods, which will be discussed in the next section, are specially designed to overcome this problem.

Step 7. Post Processing

The solution of the above step in FEM is usually in terms of scalar potentials or vector potentials or both. However the quantities of interest are the electric field, magnetic field, current distribution, or coil impedance. Furthermore since the potentials are not physical and hence not measurable, they can not be compared with experimental data. So post processing is necessary to compute other measurable quantities to interpret the results.

3.5 Multigrid methods

3.5.1 Introduction

Numerical methods for many problems in electromagnetics as well as in other engineering fields usually result in solving a set of linear algebraic equations, which can be written compactly as

$$Au = f \quad (3.83)$$

in which A is the system matrix, u represents the unknown vector that is to be determined, and f represents the known vector or right hand side.

The methods for solving linear algebraic equations or matrix equations can be categorized into two groups: direct methods and iterative methods. In general for solving a linear systems of equations, direct methods, based on Gaussian elimination, are preferred. However, many numerical methods, such as finite element methods and meshless methods, usually result in a sparse matrix and direct methods do not fully exploit the sparsity. Iterative methods are efficient for solving sparse matrix equations. Popular iterative methods include Jacobi iteration, Gauss-Seidel iteration, and conjugate gradient methods. In order to obtain good accuracy, the grid or mesh is made very fine, which in turn makes the computation procedure expensive. Multigrid methods are specially designed to overcome this problem.

Error components of a numerical computation can be thought of, in Fourier space, as waves made up of linear combinations of scaled sine and cosine functions. A long wave (low frequency) on a fine grid becomes a shorter wave (higher frequency) when represented on the scale of a coarser grid, as shown in Figure 3.5. It has been observed that for a particular level

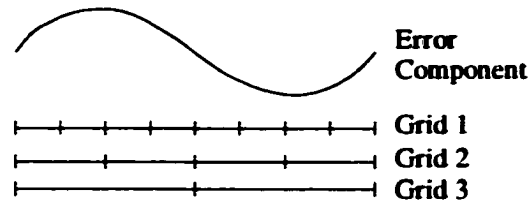


Figure 3.5 Grid levels

of grid, high frequency components (oscillatory modes) are damped fast, while low frequency components (smooth modes) are damped slowly. This is the key idea in multigrid methods. [73] has shown a set of numerical experiments illustrating this phenomenon.

When relaxation begins to stall after some iterations, it means that smooth error modes become predominant. The fact that smooth modes on a fine grid look less smooth on a coarse grid suggests that it is advisable to move the relaxation to a coarse grid, on which the smooth error modes appear more oscillatory and relaxation will be more effective. The fundamental idea underlying multigrid methods is to combine computations done on different levels, using results from one level to obliterate the error components of another.

Multigrid methods are known to be optimal in the sense that the number of iterations required to reach a fixed accuracy is independent of the mesh size [77]. This property together with their high convergence rate makes the multigrid methods attractive for solving large systems of algebraic equations.

3.5.2 Basic Elements of Multigrid Methods

Glossary

Multigrid methods have developed their own terminology as summarized below:

- (1) Smoother: an iterative or direct solver.
- (2) Correction step: correction obtained from the next coarser grid by solving a related problem.
- (3) Pre-smoother: solver used before the correction step.
- (4) Post-smoother: solver used after the correction step.
- (5) Restriction: projection method for transferring data from a fine grid to a coarse grid.
- (6) Prolongation: interpolation procedure for transferring data from a coarse grid to a fine grid.

Residual Equation and Residual Correction

The residual equation is the first important issue in multigrid methods as well as in other iterative techniques. In solving the linear algebraic equations (3.83), we define error or algebraic error as

$$e = u - \hat{u} \quad (3.84)$$

in which \hat{u} is the approximation to u . Substituting \hat{u} into (3.83) and subtracting the left hand side from the right hand side lead to the quantity called residual r , a computable measure of how well \hat{u} approximates u , given by

$$r = f - A\hat{u} \quad (3.85)$$

From (3.83) and (3.84) it is easy to derive the residual equation:

$$Ae = r \quad (3.86)$$

An intimate connection between the original (3.83) and the residual (3.86) equations motivates the use of the residual equation: relaxation on (3.83) with an arbitrary initial guess

\hat{u} is equivalent to relaxing on the residual equation (3.86) with the specific initial guess $e = 0$.

It is obvious from (3.84) that the exact solution u is the sum of the approximation \hat{u} and the error term e . Unfortunately e is just as inaccessible as the exact solution itself. A feasible way to improve the approximation \hat{u} is to compute the residual, solve the residual equation (3.86) for e and then compute a new approximation using the definition of error or written as

$$u = \hat{u} + e \quad (3.87)$$

This procedure is called residual correction.

Restriction and Prolongation

Restriction is a projection method for transferring data from a fine grid to a coarse grid. It is denoted as I_h^{2h} or I_h^H . Given fine grid variables \hat{u}^h , coarse grid variables \hat{u}^{2h} can be found by

$$\hat{u}^{2h} = I_h^{2h} \hat{u}^h \quad (3.88)$$

There are two commonly used restriction methods: injection and full weighting.

In injection method, values on coarse grid points are equal to values on the corresponding points on the next finer grid. This method can be expressed as

$$\hat{u}_j^{2h} = \hat{u}_{2j}^h \quad 1 \leq j \leq \frac{N}{2} - 1 \quad (3.89)$$

where N is the number of grid points on the fine grid.

In full weighting method, points on the fine grid that also show up on the coarse grid contribute half to the corresponding points on the coarse grid; points on the fine grid that do

not show up on the coarse grid contribute quarter to their “corresponding neighbors” on the coarse grid. This method can be expressed as

$$\hat{u}_j^{2h} = \frac{1}{4}(\hat{u}_{2j-1}^h + 2\hat{u}_{2j}^h + \hat{u}_{2j+1}^h) \quad 1 \leq j \leq \frac{N}{2} - 1 \quad (3.90)$$

Prolongation is an interpolation procedure for transferring data from a coarse grid to a fine grid, denoted as I_{2h}^h or I_H^h . Given coarse grid variables \hat{u}^{2h} , fine grid variables \hat{u}^h can be found by

$$\hat{u}^h = I_{2h}^h \hat{u}^{2h} \quad (3.91)$$

The most popular prolongation scheme is the well-known linear interpolation, which can be expressed as

$$\begin{cases} \hat{u}_{2j}^h = \hat{u}_j^{2h} \\ \hat{u}_{2j+1}^h = \frac{1}{2}(\hat{u}_j^{2h} + \hat{u}_{j+1}^{2h}) \end{cases} \quad 0 \leq j \leq \frac{N}{2} - 1 \quad (3.92)$$

That is, points on the fine grid that also show up on the coarse grid just take over the values of their corresponding points on the coarse grid; points on the fine grid that do not show up on the coarse grid take the average values of their corresponding neighbors on the coarse grid.

Galerkin Formula

In residual correction, the solution on coarse grid u^{2h} is interpolated to fine grid as the correction term e^h , i.e.,

$$e^h = I_{2h}^h u^{2h} \quad (3.93)$$

Left multiply (3.93) by the fine grid operator, we obtain

$$A^h e^h = A^h I_{2h}^h u^{2h} \quad (3.94)$$

The left hand side of (3.94) is nothing but the residual on the fine grid. So (3.94) can be rewritten as

$$A^h I_{2h}^h u^{2h} = r^h \quad (3.95)$$

Restrict the residual to the coarse grid, i.e., left multiply the restriction operator on both sides of (3.95), we obtain

$$I_h^{2h} A^h I_{2h}^h u^{2h} = I_h^{2h} r^h \quad (3.96)$$

The right hand side of (3.96) is actually the residual on the coarse grid r^{2h} . Denoting $I_h^{2h} A^h I_{2h}^h$ as A^{2h} , (3.96) reduces to

$$A^{2h} u^{2h} = r^{2h} \quad (3.97)$$

which is nothing but the coarse grid version of the original problem (3.83). And

$$A^{2h} = I_h^{2h} A^h I_{2h}^h \quad (3.98)$$

is called Galerkin formula. (3.98) tells us that the coarse grid operator can be obtained from the fine grid operator with restriction and prolongation operators.

3.5.3 Basic Strategies of Multigrid Methods

There are two basic flavors of multigrid methods: correction methods and nested iteration methods. Correction methods start at the finest level (K) and use the coarser levels $k < K$ solely to compute a correction, which is added to the approximate solution on level K . Nested iteration methods generate initial guesses on coarser levels and frequently reuse the coarser levels for corrections. When a good initial guess is available, correction algorithms work well. Otherwise nested iteration methods that generate initial guesses are recommended.

3.5.3.1 Correction Methods

Correction methods use the residual equation to relax on the error. First relax on the fine grid until the convergence deteriorates, then restrict the residual to a coarser grid and relax the residual equation to obtain an approximation to the error itself. The error approximation is then interpolated to the fine grid to correct the approximation obtained previously.

Figures 3.6 (a) and (b) illustrate the two commonly used correction methods: V cycle and W cycle. In the V cycle (Figure 3.6 (a)), the problem is relaxed on the finest grid Ω^h for ν_1 times and an approximation \hat{u}^h is obtained. The residual r^h is calculated and restricted to the next coarser grid Ω^{2h} . Relax the problem on Ω^{2h} and obtain the approximation \hat{u}^{2h} , calculate the residual r^{2h} and restrict it to the next coarser grid Ω^{4h} . This process continues until it reaches the coarsest grid (Ω^{8h} in Figure 3.6 (a)). Solve the problem on Ω^{8h} using either iterative method or direct method and obtain the error e^{8h} . Interpolate e^{8h} to the next finer grid Ω^{4h} and obtain e^{4h} . Use e^{4h} to correct the approximation \hat{u}^{4h} obtained previously and get a better approximation $\hat{u}^{4h} = \hat{u}^{4h} + e^{4h}$. Relax the problem on Ω^{4h} for ν_2 times. \hat{u}^{4h} is then interpolated to Ω^{2h} . This process continues until it reaches the finest grid Ω^h . This procedure

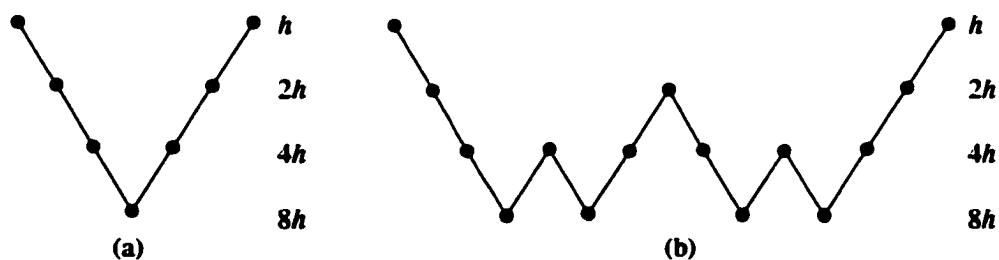


Figure 3.6 Correction methods
(a) V cycle (b) W cycle

can be summarized as taking another V cycle on the next coarser grid. The simplest case of the correction methods is called the two-grid algorithm, which is the case when there are only two grid levels. W cycle (Figure 3.6 (b)) is similar to V cycle except that it takes two, instead of one, V cycles on the next coarser grid.

The recursive definition of V cycle and W cycle is given as:

$$\hat{u}^h \leftarrow M\mu^h(\hat{u}^h, f^h)$$

in which the first \hat{u}^h as output is the approximation and the second \hat{u}^h as input is the initial guess.

(1) Relax ν_1 times on $A^h u^h = f^h$ with a given initial guess \hat{u}^h ;

(2) If $\Omega^h =$ coarsest grid, then go to 4,

$$\text{Else } f^{2h} \leftarrow I_h^{2h}(f^h - A^h \hat{u}^h)$$

$$\hat{u}^{2h} \leftarrow M\mu^{2h}(\hat{u}^h, f^{2h}) \mu \text{ times;}$$

(3) Correct $\hat{u}^h \leftarrow \hat{u}^h + I_{2h}^h \hat{u}^{2h}$;

(4) Relax ν_2 times on $A^h u^h = f^h$ with initial guess \hat{u}^h .

In practice, only $\mu = 1$ (which gives the V cycle) and $\mu = 2$ (which gives the W cycle) are used.

For many problems, a W cycle is considered more robust and easier to analyze theoretically than a V cycle. However, W cycles are much harder to parallelize efficiently because they spend more time on the coarser levels [75].

In both V cycle and W cycle, the coarsest grid is chosen to be sufficiently coarse to make the cost of solving the problem there negligible, while the finest grid is chosen to provide some desired degree of accuracy.

3.5.3.2 Nested Iteration Methods

The second basic strategy of multigrid methods is nested iteration methods (NIC), also referred to as full multigrid (FMG). NIC uses coarser grids to generate improved initial guesses. If there is no good initial guess, algorithm NIC will work better than correction methods.

The simplest NIC is the so-called one-way multigrid (OWMG), as shown in Figure 3.7 (a). OWMG begins with solving the problem on the coarsest grid (Ω^{8h} in Figure 3.7 (a)) with initial guess θ . The approximation \hat{u}^{8h} is interpolated to the next coarser grid Ω^{4h} and obtain \hat{u}^{4h} . \hat{u}^{4h} is then used as the initial guess for solving the problem on Ω^{2h} . The process continues until the problem on the finest grid is solved.

A more complicated NIC algorithm is the commonly used nested iteration V cycle, also called full multigrid V cycle (FMV), as shown in Figure 3.7 (b). Similar to OWMG, the nested iteration begins with solving the problem on the coarsest grid (Ω^{8h} in Figure 3.7 (b)) with initial guess θ . The approximation \hat{u}^{8h} is interpolated to the next coarser grid Ω^{4h} and

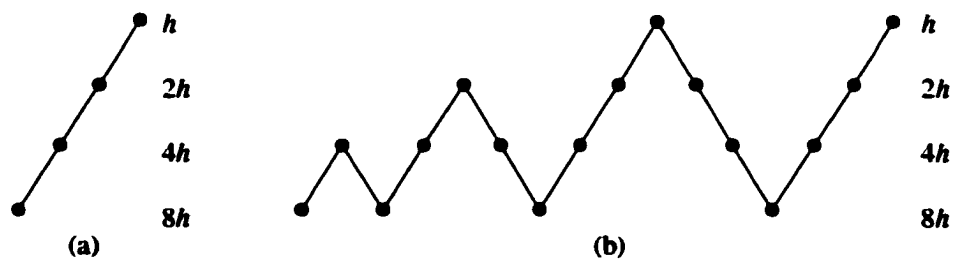


Figure 3.7 Nested iteration methods
(a) One-way Multigrid (b) Nested iteration V cycle

obtain \hat{u}^{4h} . \hat{u}^{4h} is then used as the initial guess for a V cycle on Ω^{4h} . The process continues until the V cycle on the finest grid is solved.

The recursive definition of FMV is given as:

$$\hat{u}^h \leftarrow FMV^h(\hat{u}^h, f^h)$$

(1) If $\Omega^h =$ coarsest grid, then go to 3,

$$\text{Else } f^{2h} \leftarrow I_h^{2h}(f^h - A^h \hat{u}^h)$$

$$\hat{u}^{2h} \leftarrow FMV^{2h}(0, f^{2h});$$

(2) Correct $\hat{u}^h \leftarrow \hat{u}^h + I_{2h}^h \hat{u}^{2h};$

(3) $\hat{u}^h \leftarrow MV^h(\hat{u}^h, f^h).$

Step 3 is the recursive definition of V cycle given above.

As seen from the above recursive definition and Figure 3.7 (b), each V cycle is preceded by a smaller V cycle designed to provide the best initial guess possible. The extra work done in these preliminary V cycles is not only inexpensive, but generally pays for itself.

3.5.4 Algebraic Multigrid Method

The multigrid methods discussed above are also referred to as geometric multigrid methods, because the processes of making the grid coarser or coarsening processes (picking the coarse grid and defining interpolation) are based on the geometrical structures and a hierarchy of coarser grids are constructed explicitly. However, the implementation of geometric multigrid techniques can be cumbersome for practical engineering problems, such as FEM modeling with complex geometries, because the coefficients in the governing partial

differential equations may be varying strongly or have large discontinuities and the computational grids are therefore unstructured. Algebraic multigrid methods (AMG) on the other hand automatically construct a hierarchy of coarser grids without user intervention. The only information needed for coarsening is the operator matrix on the finest level. Since no geometric information is needed, AMG can thus be used as black box equation solver.

The coarsening process is performed automatically in a way that ensures the range of interpolation approximates those errors not efficiently reduced by relaxation [76]. The number of coarser levels to be used is not known a priori.

The procedures of AMG can be split into two parts: setup phase and solution phase. The setup phase consists of choosing the coarser grids and defining the grid transfer operators (restriction and interpolation operators) and coarse grid operator. The solution phase uses the components defined in order to perform standard multigrid cycling until a desired level of tolerance is reached. The solution phase is actually the same as the standard multigrid methods discussed above. So in the remaining of this section, only the setup phase will be discussed.

3.5.4.1 Setup Phase

The setup phase is illustrated in Figure 3.8, in which m is the index of grid level, labeling from the finest grid to the coarsest grid. In the m^{th} grid level, the setup phase chooses the next coarser grid Ω^{m+1} and defines the interpolation operator I_{m+1}^m . Then the restriction operator I_m^{m+1} is defined as the transpose of the interpolation operator and the next coarser grid operator A^{m+1} is obtained using the Galerkin formula. If Ω^{m+1} is not small enough, the setup

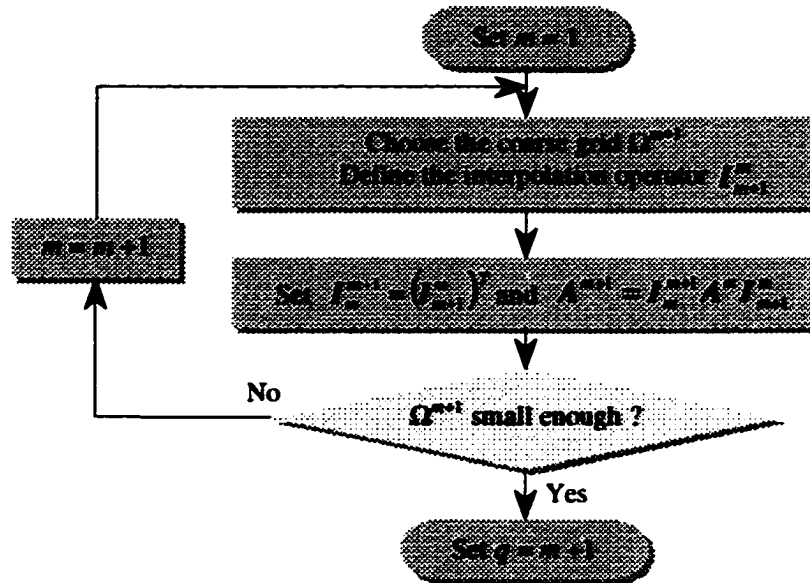


Figure 3.8 Setup phase

phase successively define the coarser grids and the corresponding operators. Otherwise, set $q = m+1$, in which q is the number of grid levels.

Now what have not been discussed are the coarsening scheme and defining the operators.

3.5.4.2 Coarsening Scheme

Notation

The coarsening scheme of AMG is rather complicated. Before discussing the coarsening scheme, let us define the notations that will be used later.

- (1) **C-variables and F-variables:** The variables in the fine grid Ω^h are partitioned into C-variables (denoted as C) and F-variables (denoted as F). C-variables are actually the variables in the next coarser grid Ω^H and F-variables are those excluded in Ω^H . That is

$$\Omega^h = C \cup F, \quad C \cap F = \emptyset, \quad \Omega^H = C \quad (3.99)$$

(2) Neighborhood of Point i :

$$N_i = \{j \mid a_{ij} \neq 0, i \neq j\} \quad (3.100)$$

where i and j represent the row and column indices of the grid operator A^h and a_{ij} is the $(i,j)^{\text{th}}$ element of A^h .

(3) Local set of coarse nodes: defined as the intersection of neighborhood and C-variables.

$$C_i = \{j \mid N_i \cap C\} \quad (3.101)$$

(4) Local set of fine nodes: defined as the intersection of neighborhood and F-variables.

$$F_i = \{j \mid N_i \cap F\} \quad (3.102)$$

(5) Strong connection: The distance $d(i, j)$ between Points i and j is defined as

$$d(i, j) = \frac{|a_{ij}|}{\max_{i \neq i} |a_{ii}|} \quad (3.103)$$

Point i is strongly connected to j , or strongly depends on j , if $d(i, j) \geq \theta$ for $0 < \theta \leq 1$ (θ is usually taken to be 0.25 in practice).

(6) Set of all strong connections of Point i :

$$S_i = \{j \in N_i : d(i, j) \geq \theta\} \quad (3.104)$$

(7) Set of points strongly connected to i :

$$S_i^T = \{j \in N_i : i \in S_j\} \quad (3.105)$$

(8) For a set P , $|P|$ denotes the number of elements in P .

Figure 3.9 illustrates the concepts of S_i and S_i^T . Assume that all the points, with their distances to a reference point greater than the threshold θ , fall in a circle with the the

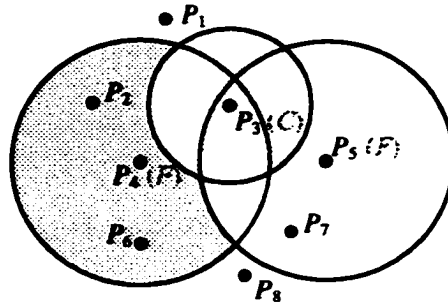


Figure 3.9 Illustration of coarsening scheme

reference point being the center. From the above notations, we have: $\{P_2, P_3, P_6\} \subseteq S_4$, $\{P_3, P_7\} \subseteq S_5$ and $\{P_4, P_5\} \subseteq S_3^T$.

Coarsening Scheme

Having established the above notation, we can now define the coarsening scheme as:

- (1) Set $C = \phi$, $F = \phi$, $U = \Omega^h$, and $\lambda_i = |S_i^T|$ for all i ;
- (2) Pick an $i \in U$ with maximal λ_i . Set $C = C \cup \{i\}$ and $U = U - \{i\}$;
- (3) For all $j \in S_i^T \cap U$, perform Steps 4 and 5;
 - (4) Set $F = F \cup \{j\}$ and $U = U - \{j\}$;
 - (5) For all $l \in S_j \cap U$, set $\lambda_l = \lambda_l - 1$;
- (6) For all $j \in S_i \cap U$, set $\lambda_j = \lambda_j - 1$;
- (7) If $U = \phi$, stop;

Otherwise, go to Step 2.

The coarsening scheme begins by setting C-variables and F-variables to be empty. An intermediate set U , which equals the fine grid variables initially, is used to record the

variables that have not been classified into C or F . λ_i is the number of points strongly connected to Point i .

Point $i \in U$ with maximal λ_i is classified into C with the purpose of efficiency. (Suppose P_3 in Figure 3.9 has maximal λ .) Point i (P_3) is then removed from U . The points in U that are strongly connected to i (P_4 and P_5) are considered as F-variables and removed from U , because they can be interpolated with information of i . Since they have been classified, for each of the strong connections of these F-variables (also in U), the λ value reduces one. Since Point i has been classified, for each of the strong connections of i , the λ value reduces one. The procedure continues until all the fine grid variables have been classified into C-variables or F-variables.

3.5.4.3 Interpolation Operator

For common relaxation schemes, a smooth error e is algebraically characterized by the fact that the residual $r = Ae$ is small in some sense compared to the error itself [77]. That is,

$$r_i = a_{ii}e_i + \sum_{j \in N_i} a_{ij}e_j = 0 \quad (3.106)$$

The fine grid correction is computed via the interpolation operator by

$$(e^h)_k = (I_H^h e^H)_k = \sum_{j \in C} w_{ij} e_j, \quad \forall i \in \Omega^h \quad (3.107)$$

with the interpolation weights

$$w_{ij} = \begin{cases} 1 & i = j \in C \\ -\frac{a_{ij} + c_{ij}}{a_{ii} + c_{ii}} & i \in F, j \in C \\ 0 & \text{else} \end{cases} \quad (3.108)$$

and

$$c_{ij} = \sum_{p \in F_i} \frac{a_p a_{pj}}{\sum_{l \in C_i} a_{pl} + a_{pi}} \quad (3.109)$$

Having the interpolation operator, the restriction operator is obtained by transposing the interpolation operator. The coarse grid operator is obtained using the Galerkin formula.

CHAPTER 4 POD MODELS AND TAGUCHI METHODS

4.1 Introduction

Reliability of nondestructive testing techniques is of considerable concern to the NDE community. In general signals generated by identical flaws are usually different under practical testing conditions. A variety of factors influence the measurements and hence the decision if a test specimen is to be accepted or rejected. Repeated inspections of a specific flaw can produce different magnitudes of response because of minute variations in setup and calibration. Different operators may make different decisions when testing the same specimen. Even the same operator may make different decisions when testing the same specimen twice.

The reliability of an NDE technique is characterized by the concept of probability of detection (POD). Hence there is a need for developing POD models for a nondestructive inspection. POD models constitute a powerful tool for quantifying the reliability and assessing the applicability of a selected NDE technique. The POD model accounts for the variabilities that affect the output signal and generates a distribution of the signal around its mean value, thus predicting the variations. Such a prediction helps in identifying optimal test parameters for achieving the highest probability of detection for a given flaw.

The Taguchi method is a statistical analysis technique that is used in quality improvement and design of experiments. The reliability of an NDE technique can be improved by the Taguchi method, which optimize the design parameters and make the design insensitive to the influence of uncontrollable factors. The Taguchi method is also a very useful tool for

partial factorial experiment or simulation design, which reduces the number of experiments needed for optimization considerably.

4.2 POD Models

4.2.1 Introduction

The main objective in nondestructive evaluation is to make an accept/reject decision based on the absence or presence of a flaw respectively in the test specimen, as illustrated in Figure 4.1. However there are a number of other secondary factors involved in the accept/reject decision process such as the cost incurred due to the false acceptance and false alarm that affect the decision process. This section describes a model based POD evaluation method, which is then used to optimize experiment setup.

4.2.2 Sources of Variability

The first step in computing probability of detection is to find out the sources of variabilities. Typical sources of variabilites of an NDE system include:

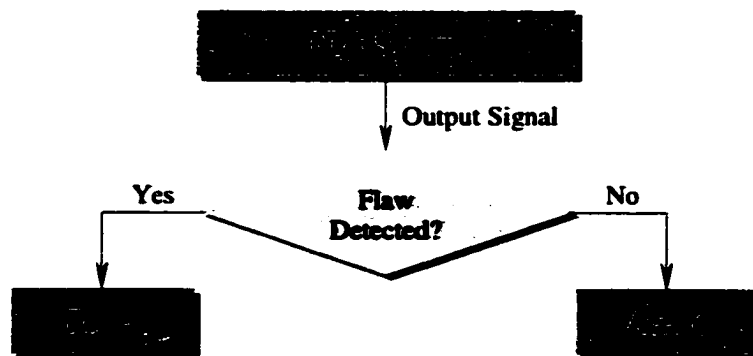


Figure 4.1 Decision process of NDE system

- **Human factors**
- **Variations in specimen geometry, such as surface roughness and defect shape and dimensions**
- **Variations in excitation sources, such as magnetization level and current value**
- **Variations in material property, such as permeability, conductivity, stress, residual magnetism, magnetic history, etc**
- **Variations in experiment setup, such as lift-off, gain, frequency, and scan related factors**
- **Instrumentation noise**

Human factor is the mental and physical make of the individual, the individual's training and experience, and the conditions under which the individual must operate that influence the ability of the NDE system to achieve its intended purpose [91]. The effect of human factors is discussed in [91-94] and is beyond the scope of this report.

Instrumentation noise always exists and is usually characterized as additive Gaussian noise.

4.2.3 POD Concepts

The probability of detection of a particular flaw of given size using a given measurement system can be determined by generating conditional probability density function (pdf) of the measurement signal for the flaw. Figure 4.2 shows the typical distributions of the measurement outputs in the absence of a flaw, $p(y|x_0)$, and in the presence of a flaw, $p(y|x_1)$, where y is the measurement output and x_0 and x_1 stand for the no-flaw and flaw situations respectively.

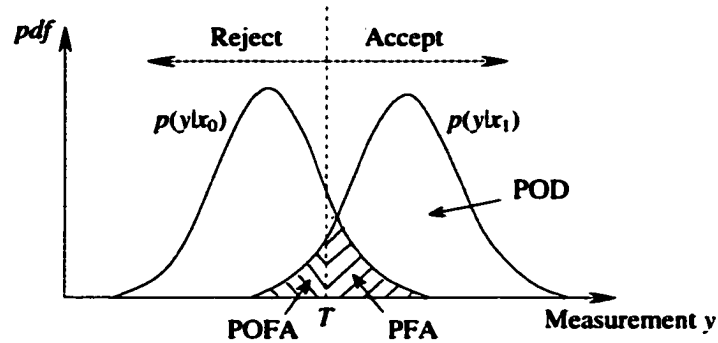


Figure 4.2 Typical distributions of flaw/no flaw signals

The interpretation of NDT data involves the decision if the observed response is a flaw signal or no-flaw signal (noise). The simplest approach to making the decision is to choose a threshold (T) such that all signals above the threshold will be classified as flaw signals and signals below the threshold will be interpreted as noise. Hence the probability of detection is determined by

$$\text{POD} = \int_T p(y|x_1) dy \quad (4.1)$$

If the pdf's of flaw signal and noise overlap, as shown in Figure 4.2, the data interpretation based on threshold detection will inevitably involve two types of errors that are of significance. The two types of errors are:

- (1) False alarm: The component without flaw is rejected due to incorrect interpretation of noise fluctuations as a flaw indication. A high false alarm rate is usually undesirable as this would result in the unnecessary replacement of components that are actually in good or even excellent condition. The probability of such an incorrect indication is called the probability of false alarm (PFA) and is calculated as

$$\text{PFA} = \int_T p(y|x_0) dy \quad (4.2)$$

(2) **False acceptance:** The component with flaw is accepted due to incorrect interpretation of flaw signal as noise fluctuations. False acceptance is undesirable as this would result in very serious consequence due to a miss in the detection of the flaw. The probability of such an incorrect interpretation is called the probability of false acceptance (POFA) and is calculated as

$$\text{POFA} = \int_{-\infty}^T p(y | x_1) dy \quad (4.3)$$

and related to POD by

$$\text{POFA} = 1 - \text{POD} \quad (4.4)$$

It is obvious by observing Figure 4.2 that when the PFA decreases, the threshold moves to the right, and hence the POD decreases. Similarly, the POD increases with increase in the PFA. The relative operating characteristic (ROC) shows the relationship between POD and PFA. Hence there is a trade-off between a high POD and a low PFA. Figure 4.3 shows a typical ROC curve.

4.2.4 Selection of Thresholds

Once the conditional pdf's are obtained, the threshold T is then selected using an appropriate criterion. The selection of the threshold is very important in signal classification

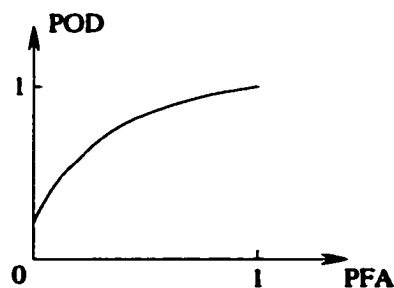


Figure 4.3 A typical ROC curve

because the probability of detection is dependent on the value of the threshold chosen. As the threshold decreases the POD increases along with an increase in PFA. Various criteria for selecting the threshold based on the application problem include:

1. Set PFA to a constant

In many practical applications it is desired to keep the probability of false alarm as low as possible. The PFA is independent of the pdf of the flaw signal and dependent only on the pdf of the background noise. The threshold is selected such that the PFA is a constant.

2. Set POD of the critical flaw size to a constant

This scheme is useful when the inspection system is expected to detect only flaws that are bigger than a critical size. The threshold is chosen such that the critical flaw is detected with a specified POD. The threshold is used to compute the POD and PFA of other flaws of different dimensions.

3. Minimization of the total signal classification error

The error in signal interpretation includes false alarm and false acceptance of the test specimen. In this scheme, the threshold is selected to minimize the weighted sum of the overall error in signal classification [97, 98], which is given by

$$E(T) = P \int_{-\infty}^T p(y | x_1) dy + (1 - P) \int_T^{\infty} p(y | x_0) dy \quad (4.5)$$

where P is the prior probability of a flaw being present in the test specimen. The threshold T is obtained by solving

$$\frac{\partial E(T)}{\partial T} = 0 \quad (4.6)$$

4.2.5 POD Models

Several probabilistic models are available for estimating the probability of detection of a flaw. Some of the popular approaches are summarized below.

1. Experimental Model

In this approach the flaw signals and their fluctuations are determined by a large number of sample measurements. The experimental data is used to estimate the POD of the flaw. Unfortunately the determination of the POD requires a rather extensive set of measurements to obtain statistically sound estimates. In general, this approach for generating POD curves is time consuming and expensive. It involves the machining of defects in a large number of specimens and requires a large number of operators.

2. Numerical Model

The limitations of the experimental model are overcome by numerically modeling the NDE phenomena. The flaw signal and the effect of measurement variabilities are predicted via simulation on a digital computer. Reliable methods are required to predict flaw signals and background noise as a function of flaw size and shape, measurement setup, and other inspection parameters. Although this approach is much more efficient and cost effective than the experimental model, it is computationally intensive.

3. Functional Model

This approach is an improvement over the numerical model and is employed in this report. Since the probabilistic approach requires at least thousands of measurement data for accurately estimating the probability density functions, simulation of the numerical model becomes time consuming and cumbersome. The functional model uses a mathematical function that fits a curve that accurately prescribes the signal variations with respect to experimental parameters. Data points for estimating the pdf's are generated using this functional model. In this way the number of simulations required is reduced by several orders without sacrificing accuracy.

4.2.6 POD Evaluation Based on Functional Model

The procedure for estimating the probability density functions using the functional model based POD evaluation method is illustrated in Figure 4.4. A finite element model predicts the signals numerically for a given test geometry (with and without flaw) and some values of variability parameters, such as liftoff. Only limited finite element simulations are required. The signal magnitudes are then used to generate two mathematical functions (one for each of the cases with and without flaw), using simple curve fitting procedures. These functions

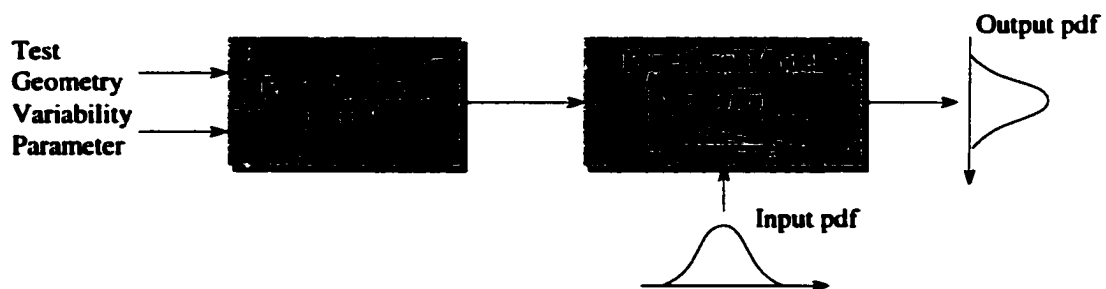


Figure 4.4 Procedure for generating conditional probability density functions

establish the relationship between signal magnitude and the perturbed parameter. A large number of values of the perturbed parameter, with the given distribution (input pdf), are mapped using the mathematical function to generate the conditional probability density functions of the signal magnitudes (output pdf's), $p(y|x_0)$ in the absence of flaw and $p(y|x_1)$ in the presence of a flaw, corresponding to the pdf of the perturbed parameter.

The simplest way to generate the mathematical function is using polynomial curve fitting, which fits the given data in a least-square sense. The order of the polynomial is chosen such that the norm of the residuals is small. When the data are not smooth enough, polynomial curve fitting requires a large order of polynomial to approximate the relationship. In this case an alternative method is to use interpolation to obtain the signal magnitude for an arbitrary value of variability parameter.

Once the two conditional pdf's are generated, the probability of detection can be evaluated using (4.1) with appropriately selected threshold.

The above discussion describes the procedure of evaluating POD due to a single variability parameter. In many applications, we need to optimize experiment setup with respect to multiple variabilities and simultaneously. This problem is solved by modeling the variabilities as a multivariate Gaussian distribution [99], expressed as

$$p(\mathbf{x}) = \frac{1}{(2\pi)^{N/2} |\Sigma|^{1/2}} \exp\left\{-\frac{1}{2}(\mathbf{x} - \boldsymbol{\mu})^T \Sigma^{-1}(\mathbf{x} - \boldsymbol{\mu})\right\} \quad (4.7)$$

where \mathbf{x} denotes the perturbed factors and

$$\boldsymbol{\mu} = E(\mathbf{x}) \quad (4.8)$$

$$\Sigma = E[(\mathbf{x} - \boldsymbol{\mu})(\mathbf{x} - \boldsymbol{\mu})^T] \quad (4.9)$$

are the expectation vector and covariance matrix of \mathbf{x} respectively. This method requires a large number of simulations, which is computationally intensive. An alternative scheme is to use the Taguchi method, which will be discussed in the next section. The Taguchi method requires only limited number of simulations using the fractional factorial design, where no independency assumption is needed.

4.2.7 Confidence Bounds of POD Estimates

The calculation of POD described above involves the integration of the conditional pdf of signal magnitude with flaw from the threshold to infinity. When using a digital computer, this is implemented by computing the ratio of the number of signal values that are greater than the threshold (T) over the total number of signal values. That is,

$$\hat{P}_d = \frac{N_d}{N} \quad (4.10)$$

where \hat{P}_d is the estimate of the true POD that is denoted as P_d , N_d the number of signal values that are greater than the threshold, and N the total number of signal values. Intuitively the larger the value of N , the better the accuracy of POD estimation. The confidence interval for the estimated POD can be derived from the Chebyshev's inequality, which states that for any $\varepsilon > 0$, a probabilistic bound on the accuracy of the estimate is given by

$$P\left\{|\hat{P}_d - P_d| > \varepsilon\right\} \leq \frac{E\left[\left(\hat{P}_d - P_d\right)^2\right]}{\varepsilon^2} \quad (4.11)$$

Let x_1, x_2, \dots, x_N denote the N sample in the distribution, then from (4.10) \hat{P}_d is given by

$$\hat{P}_d = \frac{\sum_{k=1}^N I_k}{N} \quad (4.12)$$

with

$$I_k = \begin{cases} 1 & \text{if } x_k > T \\ 0 & \text{otherwise} \end{cases} \quad (4.13)$$

The expectation and variance of I_k are given by

$$E(I_k) = 1 \cdot P\{I_k = 1\} + 0 \cdot P\{I_k = 0\} = P_d \quad (4.14)$$

$$\text{Var}(I_k) = E(I_k^2) - E^2(I_k) = P_d - P_d^2 \quad (4.15)$$

Using (4.12), (4.14), and (4.15), we have

$$\begin{aligned} E\left[(\hat{P}_d - P_d)^2\right] &= \text{Var}(\hat{P}_d) = \frac{\sum_{k=1}^N \text{Var}(I_k)}{N^2} \\ &= \frac{N \cdot (P_d - P_d^2)}{N^2} = \frac{P_d(1 - P_d)}{N} \end{aligned} \quad (4.16)$$

(4.16) reaches its maximum with $P_d = \frac{1}{2}$, i.e.,

$$E\left[(\hat{P}_d - P_d)^2\right] \leq \frac{1}{4N} \quad (4.17)$$

Substitute (4.17) into (4.11), we have

$$P\left\{|\hat{P}_d - P_d| > \varepsilon\right\} \leq \frac{1}{4N\varepsilon^2} \quad (4.18)$$

(4.18) tells us that with the confidence level $1 - P\left\{|\hat{P}_d - P_d| > \varepsilon\right\}$ and the number of samples

N , the error in the estimated POD is in the interval $(-\varepsilon, \varepsilon)$, where ε is computed from (4.18).

4.2.8 Discussions

The definitions of POD (P_d) and PFA (P_f) in (4.1) and (4.2) can be rewritten as

$$P_d = \int_{-\infty}^{\infty} I_T(y)p(y|x_1) dy \quad (4.19)$$

and

$$P_f = \int_{-\infty}^{\infty} I_T(y)p(y|x_0) dy \quad (4.20)$$

respectively with

$$I_T(y) = \begin{cases} 1, & y \geq T \\ 0, & y < T \end{cases} \quad (4.21)$$

They are estimated by the Monte Carlo simulations:

$$\hat{P}_d = \frac{1}{N} \sum_{i=1}^N I_T(y_{1,i}) \quad (4.22)$$

$$\hat{P}_f = \frac{1}{N} \sum_{i=1}^N I_T(y_{0,i}) \quad (4.23)$$

where $y_{1,i}$ ($i = 1, 2, \dots, N$) are independent and identically distributed (i.i.d.) random variables in the presence of a flaw and $y_{0,i}$ ($i = 1, 2, \dots, N$) are i.i.d. random variables in the absence of a flaw with N denotes the number of samples in each case. It is readily shown that

$$E\{\hat{P}_d\} = P_d \quad (4.24)$$

$$\text{Var}\{\hat{P}_d\} = \frac{P_d(1-P_d)}{N} \quad (4.25)$$

$$E\{\hat{P}_f\} = P_f \quad (4.26)$$

$$\text{Var}\{\hat{P}_f\} = \frac{P_f(1-P_f)}{N} \quad (4.27)$$

That is, (4.22) and (4.23) are unbiased estimates and their variances are given in (4.25) and (4.27) respectively. The variances are said to be large and can be substantially reduced using importance sampling technique that makes use of the information of the integrands in (4.1) and (4.2) [116].

Importance sampling got its name because we sample more intensively where $p(y|x_1)$ and $p(y|x_0)$ make the greatest contribution to the integrals (4.1) and (4.2). (4.19) and (4.22) can be rewritten as

$$P_d = \int_{\Omega} I_T(y) w_1(y) p^*(y|x_1) dy \quad (4.28)$$

$$P_f = \int_{\Omega} I_T(y) w_0(y) p^*(y|x_0) dy \quad (4.29)$$

where

$$w_1(y) = \frac{p(y|x_1)}{p^*(y|x_1)} \quad (4.30)$$

$$w_0(y) = \frac{p(y|x_0)}{p^*(y|x_0)} \quad (4.31)$$

are called weighting functions. The estimates of POD and PFA are then given as

$$\hat{P}_d^* = \frac{1}{N^*} \sum_{i=1}^{N^*} I_T(y_{1,i}) w_1(y_{1,i}) \quad (4.32)$$

$$\hat{P}_f^* = \frac{1}{N^*} \sum_{i=1}^{N^*} I_T(y_{0,i}) w_0(y_{0,i}) \quad (4.33)$$

By appropriately choosing $p^*(y|x_1)$ and $p^*(y|x_0)$, one can significantly reduce the variances of the estimates (4.32) and (4.33). The cost of importance sampling is that it is not easy to construct nonuniform random variables that have densities similar to $p(y|x_1)$ and

$p(y|x_0)$ respectively [116]. This problem has been solved in many applications in signal detection that estimate small probability of false alarm [117-122]. However, they are efficient only when the PFA is very small (generally smaller than $1.e-4$), which is not the case in current NDE techniques.

Observing (4.25) and (4.27), it is easy to find that increasing the number of samples is a simpler way to reduce variances of estimates. This is feasible because we can obtain a large number of data necessary for estimating the POD and PFA easily and quickly using the functional model presented in Section 4.2.6.

4.3 Taguchi Methods

4.3.1 Introduction

The Taguchi method is a statistical analysis technique that is used in quality improvement and design of experiments. In this technique, Taguchi simplifies the conventional statistical tools by identifying a set of stringent guidelines for experiment layout and the analysis of results. Factors that influence produce/process quality are categorized into controllable factors or uncontrollable factors. Controllable factors are the design parameters that can be easily controlled under practical conditions. Uncontrollable factors, also referred to as noise factors, are difficult to control in practical operations; but they are under control in laboratory conditions. Taguchi's approach ensures quality by optimizing the design of the product/process and making the design insensitive to the influence of uncontrollable factors (robustness).

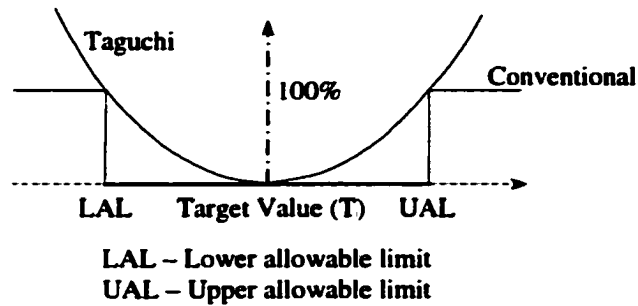


Figure 4.5 Taguchi and conventional loss function

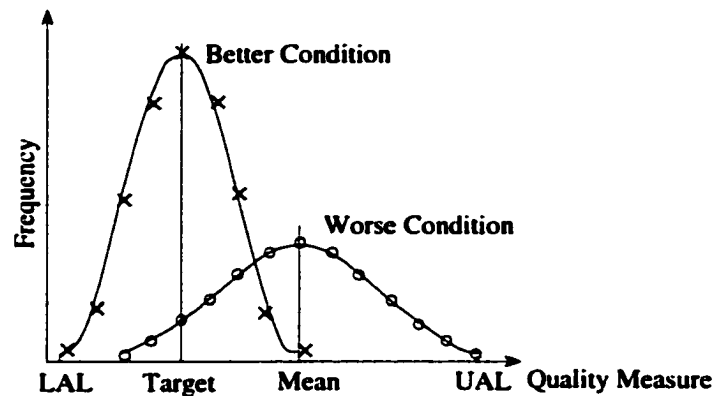


Figure 4.6 Representation of the Taguchi approach

The basic idea underlying Taguchi's quality control philosophy is the minimization of variation around the target value. A product is functionally acceptable if the measure of the specified parameter is within the range between the lower allowable limit (LAL) and upper allowable limit (UAL), as shown in Figure 4.5. In contrast to the conventional loss function, the performance begins to deteriorate gradually as the design parameter deviates from its optimum value. If Y represents the quality characteristics and Y_0 represents the target value of Y , then the loss, in the Taguchi method, for single sample is expressed as

$$L(Y) = k(Y - Y_0)^2 \quad (4.34)$$

and for multiple samples,

$$L(Y) = k \cdot \frac{1}{n} \sum_{i=1}^n (Y_i - Y_0)^2 = k(MSD) \quad (4.35)$$

where $MSD = \sum_{i=1}^n (Y_i - Y_0)^2 / n$ is called the Mean Square Deviation, n is the number of samples, k is a constant. So a product with quality characteristic distribution of the curve labeled with “better condition” in Figure 4.6 is said to have better quality than a product with quality characteristic distribution of the curve labeled with “worse condition”.

A typical application of the method will include the following five major steps:

- (1) A brainstorming session: Determine the quality characteristic and factors (controllable and uncontrollable) and levels that need to be considered by prior experience.
- (2) Design of experiment
- (3) Conducting the experiments
- (4) Analyzing the results
- (5) Running confirmation tests

4.3.2 Experiment Design

4.3.2.1 Fractional Factorial Design

The technique of defining and investigating all possible conditions in an experiment involving multiple factors is known as the design of experiments, also referred to as factorial design. A full factorial design may result in a large number of experiments. To reduce the number of experiments to a practical level, the Taguchi method selects only a small set from

Table 4.1 Comparison of Factorial Design and Taguchi Design

Factors	Levels	Total Number of Experiments	
		Full Factorial Design	Taguchi Design
2	2	4 (2^2)	4
3	2	8 (2^3)	4
4	2	16 (2^4)	8
7	2	128 (2^7)	8
15	2	32,768 (2^{15})	16
4	3	81 (3^4)	9

all the possibilities. The method of selecting a limited number of experiments, which produces the most information, is known as the partial factorial experiment design. Table 4.1 compares the number of experiments of factorial design and those used in the Taguchi design. It shows that when the number of factors or levels is large, the number of experiments designed using Taguchi method is far smaller than that using full factorial design.

The Taguchi design is a standardized design methodology that can easily be applied by investigators. Furthermore, designs for the same experiment by two different investigators will yield similar data and will lead to similar conclusions.

4.3.2.2 Orthogonal Array

The design of experiments in the Taguchi method employs specially constructed tables known as orthogonal arrays (OA). The use of these tables makes the design of experiments

Table 4.2 Orthogonal Array $L_4(2^3)$

Trial	Column	$L_4(2^3)$		
		1	2	3
1		1	1	1
2		1	2	2
3		2	1	2
4		2	2	1

easy and consistent. Table 4.2 shows a standard OA $L_4(2^3)$. This OA is designed for the experiments with three factors and two levels of each factor. The trial numbers using this OA is four. In Table 4.2, each column contains two level 1 and two level 2 conditions for the factor assigned to the column. Two 2-level factors can be combined in four possible ways, (1,1), (1,2), (2,1), and (2,2). When any two columns of an array form these combinations the same number of times, the columns are said to be balanced or orthogonal. For example, Column 1 and Column 2 in Table 4.2 have all the above combinations once. This holds for the other column pairs.

In some applications, two levels may not be enough to represent some factors. For example, if the influence of a factor on the result is suspected to vary nonlinearly, two levels are not enough because they will give a linear output. Fortunately there are some standard OA's that treat mixed level factors. Users can also modify the standard arrays to fit the circumstances.

When the effect of changes in the level of Factor *A* determines the influence of Factor *B* and vice versa, the two factors are said to interact (written as $A \times B$). Interaction $A \times B$ is treated as a column in the orthogonal array. The interacting pair of columns along with the column where interaction is shown constitute an interacting triple.

4.3.2.3 Inner Array and Outer Array

An OA experiment design leads to reduction of variations due to controllable factors. Uncontrollable factors (noise factors) can be included in a second OA, which is used in conjunction with the array of controllable factors. Because OA's are used to define the unique experimental conditions as well as the noise factors, Taguchi calls the array for

Table 4.3 Example of inner and outer orthogonal arrays

Inner Array				Outer Array			
				Noise Factors		Col	
Controllable Factors				Results			
Trial \ Column	1	2	3	1	2	3	4
1	1	1	1	1	1	1	1
2	1	2	2	1	1	2	2
3	2	1	2	2	1	2	2
4	2	2	1	2	2	1	1

controllable factors, the Inner Array and the one for uncontrollable factors, Outer Array. Table 4.3 shows the inner and outer orthogonal arrays. To obtain complete data, each trial run of L_4 (inner array) must be repeated for each of the four noise combinations (outer array).

By expanding the design of the experiment to include noise factors in a controlled manner, optimum conditions insensitive to the influence of the noise factors can be found. These are Taguchi's robust conditions that control production close to the target value despite noise in the production process.

4.3.3 Analyses

Conducting the experiments/simulations as designed above, the results are analyzed to achieve the following three objectives:

- (1) To establish the best or the optimum design for the inspection tool, i.e., find the trial condition under which POD reaches maximum;

- (2) To estimate the contribution of individual factors;
- (3) To estimate the response under the optimum conditions.

The results of the Taguchi experiments were analyzed using the standard steps. First, the factorial effects (main effects) were evaluated and the influences of the factors were determined in qualitative terms. The optimum design parameters and the performance under this condition were also determined from the factorial effects. In the next phase, analysis of variance (ANOVA) was performed to identify the relative influence of the factors. When the experiments include multiple runs and the results are measured in quantitative terms, one of the two analysis procedures, standard analysis and *S/N* analysis, can be chosen to analyze the results. Taguchi recommends signal to noise ratio (*S/N*) analysis.

4.3.3.1 *S/N* Analysis

The signal to noise ratio measures the sensitivity of the quality characteristic investigated in a controlled manner, with respect to uncontrolled (noise factors). The *S/N* ratio is defined as

$$S/N = -10 \log_{10}(MSD) \quad (4.36)$$

where *MSD* is mean squared deviation from the target value of the quality characteristic. Taguchi's loss function in (4.35) is expressed in terms of *MSD*, and hence the *S/N* ratios. Consistent with its application in engineering and science, the value of *S/N* is desired to be large; hence the value of *MSD* should be small. Thus *MSD* is defined differently for each of the three quality characteristics considered: smaller, nominal or larger. For smaller is better:

$$MSD = (y_1^2 + y_2^2 + y_3^2 + \dots) / n \quad (4.37)$$

For nominal is the best:

$$MSD = ((y_1 - m)^2 + (y_2 - m)^2 + (y_3 - m)^2 + \dots) / n \quad (4.38)$$

where m is the nominal (target) value. For bigger is better:

$$MSD = (1/y_1^2 + 1/y_2^2 + 1/y_3^2 + \dots) / n \quad (4.39)$$

In (4.37) through (4.39), y_i is the result of the i^{th} repetition, and n is the number of repetitions.

The S/N ratio calculation is based on data from all observations of a trial condition. The set of S/N ratios can then be considered as trial results without repetitions.

4.3.3.2 Main Effects

In Taguchi analysis, the optimum condition is identified by studying the main effects of each of the factors. The main effects indicate the general trend of the influence of the factors.

Suppose we have conducted the experiments as designed in Table 4.4 and obtained the experimental results. To compute the main effect of each factor at each level, we add results (average values of each trial conditions) for trials including the factor at this level, and then divide by the number of such trials. For example, to compute the main effect of factor A at level 1, A_1 , we look in the column for A in Table 4.4 and find that level 1 occurs in experiment numbers 1 and 2. Thus the main effect of A_1 is

Table 4.4 Example of test data

Trials	A	B	C	Results (S/N)
1	1	1	1	30.0
2	1	2	2	25.0
3	2	1	2	34.0
4	2	2	1	27.0

$$\bar{A}_1 = \frac{1}{L \cdot M} \left(\sum_{j=1}^M Y_{1j} + \sum_{j=1}^M Y_{2j} \right) \quad (4.40)$$

where Y_{ij} denotes the result in the i^{th} row and j^{th} column, M is the number of repetition, L is the number of trials including the factor at this level. In our applications using S/N analysis, $M = 1$ and $Y_i = Y_{i1} = (S/N)_i$. So with Table 4.4, (4.40) reduces to

$$\bar{A}_1 = \frac{1}{2} ((S/N)_1 + (S/N)_2) = \frac{1}{2} (30.0 + 25.0) = 27.5 \quad (4.41)$$

The average effects of other factors are computed in a similar manner and summarized in Table 4.5.

Theoretically, the factorial effect is the difference between the two average effects of the factor at the two levels. The difference indicates the relative influence of the effect. The larger the difference, the stronger is the influence. The average effects can also be plotted for a visual inspection as appears in Fig 4.7. From both Table 4.5 and Figure 4.7 for this example, we can conclude that if the quality characteristic is expected to be as large as

Table 4.5 Main Effects

Columns	Factors	Level 1 (d_1)	Level 2 (d_2)	$d_2 - d_1$
1	Factor A	27.5	30.5	3.0
2	Factor B	32.0	26.0	-4.0
3	Factor C	28.5	29.5	1.0

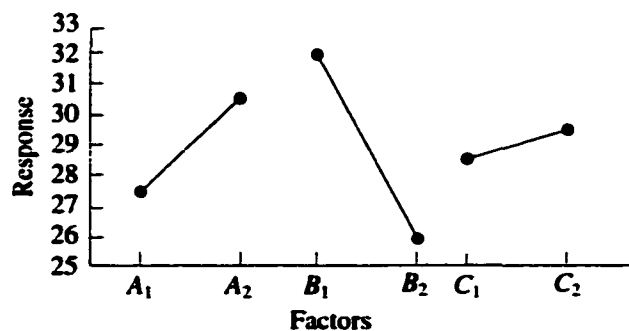


Figure 4.7 Main effects

possible, the optimum condition is $A_2B_1C_2$, and Factor B has more influence on the results than any other factors.

4.3.3.3 Analysis of Variance

The analysis of variance (ANOVA) is the statistical treatment most commonly applied to the results of experiments to determine the percent contribution of each factor. Study of the ANOVA table for a given analysis helps determine which of the factors need control and which do not. The procedure of ANOVA is described in [124-127] and summarized in the following. The following analyses are based on the S/N ratios.

Sum of Squares

The total sum of squares can be expressed as

$$S_T = \sum_{i=1}^N Y_i^2 - \frac{T^2}{N} \quad (4.42)$$

where Y_i is the S/N ratio of the i^{th} trial; N is the number of trials; $T = \sum_{i=1}^N Y_i$ is the summation of all results. The T^2/N term in (4.42) is called the correction factor, C.F.

The sum of squares for a factor (e.g. Factor A) can be calculated from

$$S_A = \sum_{k=1}^L \frac{1}{n_k} (\bar{A}_k \cdot n_k)^2 - \frac{T^2}{N} \quad (4.43)$$

where L is the number of levels; n_k is the number of trials for factor A at level k ; $(\bar{A}_k \cdot n_k)$ is the summation of (S/N)s when the level of factor A is k .

Subtracting all the factor sums of squares from the total sum of squares, the residual is referred to as error sum of squares, expressed as

$$S_c = S_T - S_A - S_B \quad (4.44)$$

Degrees of Freedom

Degrees of freedom (DOF) is an important and useful concept that is defined as the measure of the amount of information that can be uniquely determined from a given set of data. DOF of a factor equals one less than the number of levels. For a factor A with two levels, A_1 can be compared with only A_2 , not with itself. Thus a two level factor has 1 DOF. The concept of DOF can be extended to an experiment with N trials and M repetitions of each trial resulting in $N \times M$ trial runs. The total DOF is then

$$f_T = N \times M - 1 \quad (4.45)$$

Since S/N analysis is employed, the number of repetitions is 1. So the total DOF is $N - 1$.

DOF of the error term is given by

$$f_c = f_T - f_A - f_B \quad (4.46)$$

Variance

Variance measures the distribution of data about the target value. Since the data is representative of only a part of all possible data, DOF rather than the number of observations is used in the calculation.

$$\text{Variance} = \frac{\text{Sum of Squares}}{\text{Degrees of Freedom}} \text{ or } V = \frac{S}{f} \quad (4.47)$$

The variance of factors and error term can be expressed respectively as

$$V_A = \frac{S_A}{f_A} \quad (4.48)$$

and

$$V_e = \frac{S_e}{f_e} \quad (4.49)$$

Variance Ratio

The variance ratio, commonly called the F statistic, is the ratio of variance due to the effect of a factor to the variance due to the error term. This ratio is used to measure the significance of the factor under investigation with respect to the variance of all factors included in the error term. The F value obtained in the analysis is compared with a value from standard F - tables for a given statistical level of significance. When the computed F value is less than the value determined from the F - tables at the selected level of significance, the factor does not contribute to the sum of squares within the confidence level. The tables of various significance levels and different degrees of freedom are available in most statistical handbooks.

The F values are calculated by:

$$F_A = \frac{V_A}{V_e} \quad (4.50)$$

and

$$F_e = \frac{V_e}{V_e} = 1 \quad (4.51)$$

Pure Sum of Squares

The pure sum of squares is defined as the sum minus the degrees of freedom times the error variance. It is used to calculate percent contribution and is determined by

$$S'_A = S_A - f_A \cdot V_e \quad (4.52)$$

$$S'_e = S_e + (f_A + f_B) \cdot V_e \quad (4.53)$$

Percent Contribution

The percent contribution for any factor is obtained by dividing the pure sum of squares for that factor by S_T and multiplying the result by 100.

$$P_A = S'_A \times 100 / S_T \quad (4.54)$$

$$P_e = S'_e \times 100 / S_T \quad (4.55)$$

Pooling

The above quantities are listed in a table, referred to as ANOVA table, to compare contributions of the factors. When the contribution of a factor is small, the sum of squares for that factor is combined with the error S_e . This process of disregarding the contribution of a selected factor and subsequently adjusting the contributions of other factors is known as pooling. Pooling is recommended when a factor is determined to be insignificant by performing a test of significance against the error term at a desired confidence level. Thus, the statistical significance of important factors is increased. For instance, suppose the contribution of Factor A is small; then the variance for this factor is pooled with the error term. The new error variance is computed as

$$V_c = \frac{S_B + S_c}{f_B + f_c} \quad (4.56)$$

With a pooled V_c , all S' values must be modified to reflect pooling.

4.3.4 Response-Model Approach

The robust design approach described in sections 4.3.1 through 4.3.3 is referred to as loss-model approach because it models the loss or other optimization criterion (such as Taguchi's signal-to-noise ration analysis) as a function of the control factors. Associated with the loss-model approach is the product array, which consists of the inner (control) array and outer (noise) array. The disadvantages of the loss-model approach and product-array designs are discussed in [166] and summarized below:

- (1) A large number of runs may be required. Although the Taguchi methods utilize the fractional factorial designs, the number of experiments/simulations may still be prohibitive because the noise array is repeated for every trial in the control array;
- (2) Many degrees of freedom are dedicated to the estimation of interactions between control factors and noise factors. There is no flexibility in using some of these degrees of freedom to estimate other effects;
- (3) Even if the system response has linear relationship with the control and noise factors, the loss (or signal-to-noise ratio) is less likely to be linear with the factors, because the transformation of the response to loss is often nonlinear and many-to-one.

To remedy the disadvantages of the loss-model approach, Welch et al [167] proposed an alternative approach, namely, response-model approach, which model the response directly and use the response model to find control-factor values to reach robustness. In this

approach, the control factors and the noise factors are combined in a single design matrix, named combined array or single array. Using the combined array, experiment design can choose the interactions to be estimated. Use of the combined-array design can lead to significant run-size savings in the experiments/simulations. Detail procedure of the loss-model approach will be discussed in Section 6.7.4.

The discussions in this section do not mean that the loss-model approach and the product-array design are useless. They have their distinctions over the combined-array design [128, 166]:

- (1) The analysis of the data for the product array is more intuitive because all noise combinations are comparable;
- (2) The product-array design does not require a prioritized list of the important control-and-noise-factor interactions, as required in the combined-array design;
- (3) The loss-model approach provides some built-in insurance against modeling difficulties, such as missing data, because the replication using the outer array may indirectly capture the effects of important but unanticipated noise factors.

In Chapter 6, we make use of both approaches in the robust design of the magneto-optic imaging system.

CHAPTER 5 APPLICATION TO NATURAL GAS TRANSMISSION PIPELINE INSPECTION

5.1 Introduction

The natural gas pipeline system in the United States contains more than 1.2 million miles of piping [148]. Thirty percent of the energy produced in the United States is carried through this system. Figure 5.1 is a conceptual diagram of the pipeline system. The system is divided into three classifications: gathering lines carry gas from the wellhead to facilities where it may be processed and compressed; transmission lines carry gas at high pressures to local distribution systems, large individual users, or gas storage fields; distribution mains and lines receive and process gas from the transmission lines and distribute it to the end users.

Transmission pipelines transport huge volumes of high-pressure gas over long distances, through both isolated and populated areas, over varying terrain, and under a wide range of operating and service conditions. The majority of the 280,000 miles of transmission pipelines have been constructed in the past five decades. Over half of the transmission lines have been

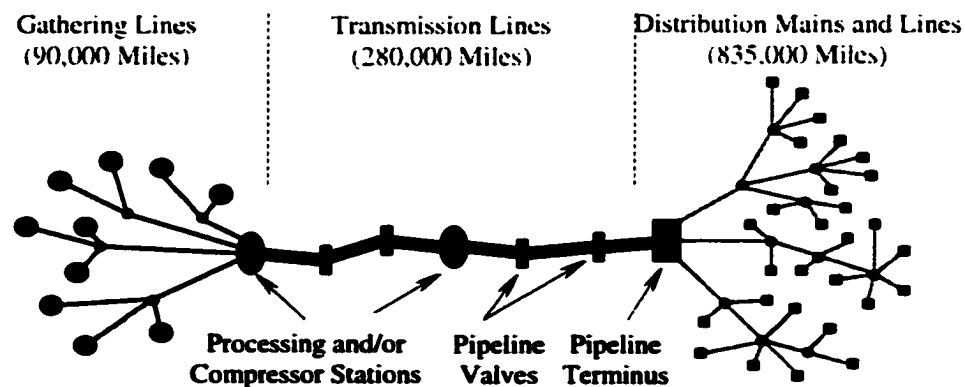


Figure 5.1 Conceptual diagram of a natural gas pipeline system

in the ground for forty or more years. Therefore, nondestructive inspection for evaluating the safety and integrity of the transmission pipelines are very important.

Various inspection methods and instruments have been developed over the past decades to assist in assuring the safety and integrity of the pipeline system. In-line inspection (ILI) of gas pipelines is accomplished by an instrumented, self-contained vehicle commonly referred to by the pipeline industry as a “pig” [149]. Magnetic flux leakage method has been the dominant technology for metal loss detection. Figures 5.2 and 5.3 show an example of an MFL pig. To inspect the pipe using the MFL method, the pipe wall is magnetized to near saturation by permanent magnets or electromagnets located on the vehicle. With the pipe

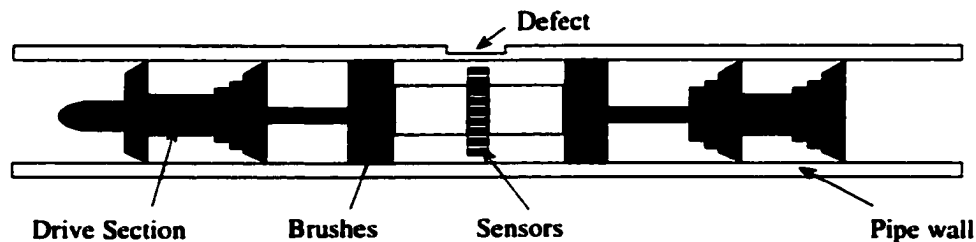


Figure 5.2 Cutaway view of a MFL “pig”

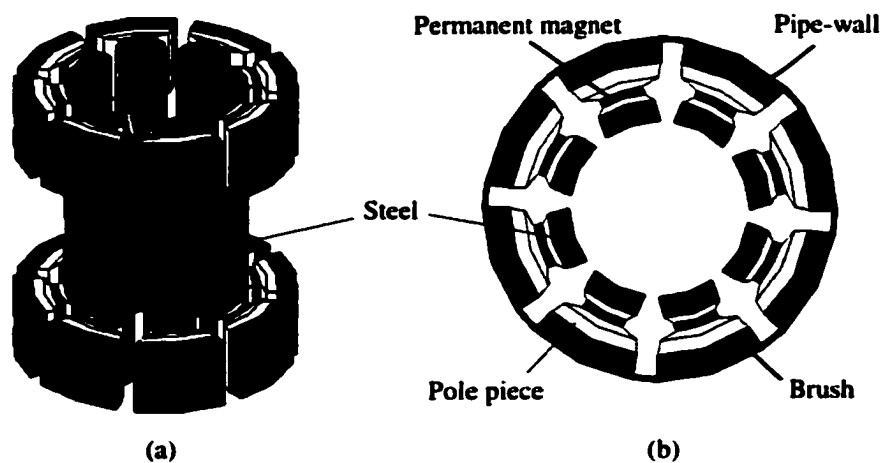


Figure 5.3 Structure of MFL pig
(a) 3-D view (b) Top view with pipe-wall

saturated, any reduction in wall thickness due to metal loss corrosion or gouges will force some of the magnetic flux to leak out of the pipe, as shown in Figure 5.4. The magnetic fields generated by MFL pigs are oriented along a path that is parallel to the axis of the pipe. This direction of field is effective for detecting and locating anomalies that are oriented along the circumferential direction. The leakage is detected by the sensors mounted between the magnets. Principles of the MFL method were discussed in Section 2.3.1. The sensor network is designed to cover the entire 360-degree circumference of the pipe and located in close proximity to the wall of the pipe.

The MFL pig discussed so far is sensitive to the presence of circumferential cracks. However, inspection tool is insensitive to stress corrosion cracking (SCC) which are oriented largely in the axial direction. A possible solution to this problem is to utilize the fields

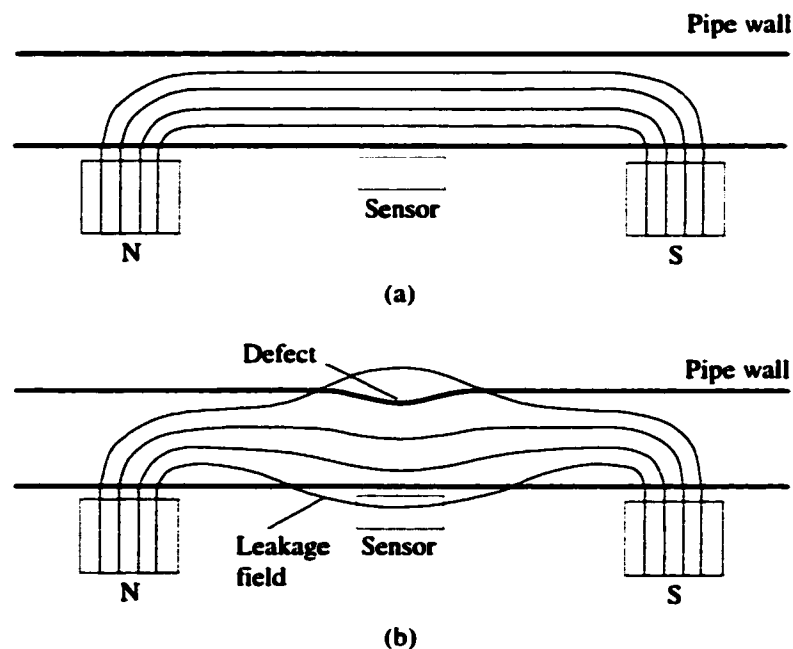


Figure 5.4 MFL defect detection
(a) No defect present (b) Defect present

associated with the circumferential currents generated in the pipe-wall by the movement of the magnetizer relative to the pipe-wall [150].

Variabilities that influence the probability of detection include the material properties of the pipe and the magnetizing unit, radial liftoff of the sensors, sensor spacing in the circumferential direction, etc.

A 3-D finite element model with magnetic scalar potential formulation is employed to predict signals under various testing conditions. Probability of detection with respect to each of the perturbed parameters is studied to optimize that parameter and determine the detection reliability. The Taguchi method is used to determine the optimum combination of the test parameters as well as reduce the total number of simulations.

5.2 Finite Element Modeling

5.2.1 Formulations

The governing equation and the corresponding boundary conditions for modeling the MFL phenomenon in natural gas transmission pipeline inspection are given as

$$\nabla \cdot \mu \nabla \psi = 0 \quad (5.1)$$

$$\psi = 0 \quad \text{on } S_1 \quad (5.2)$$

$$\frac{\partial \psi}{\partial n} = 0 \quad \text{on } S_2 \quad (5.3)$$

Since the right hand side of (5.1) vanishes, the energy functional is simply expressed as

$$F(\psi) = \frac{1}{2} \langle L\psi, \psi \rangle = \sum_{e=1}^M F^e(\psi^e) \quad (5.4)$$

with

$$F^e(\psi^e) = \frac{1}{2} \iiint_{V_e} \psi^e \nabla \cdot \mu^e \nabla \psi^e dV \quad (5.5)$$

Using the first scalar Green's theorem, which states that for scalars a , b , and u we have the following equation,

$$\iiint_V [a \nabla \cdot (u \nabla b) + u (\nabla a) \cdot (\nabla b)] dV = \iint_S au \frac{\partial b}{\partial n} dS \quad (5.6)$$

(5.5) becomes

$$F^e(\psi^e) = \frac{1}{2} \iint_{S_e} \psi^e \mu^e \frac{\partial \psi^e}{\partial n} dS - \frac{1}{2} \iiint_{V_e} \mu^e \nabla \psi^e \cdot \nabla \psi^e dV \quad (5.7)$$

Notices that

$$\sum_{e=1}^M \iint_{S_e} \psi^e \mu^e \frac{\partial \psi^e}{\partial n} dS = \iint_{S_1+S_2} \psi \mu \frac{\partial \psi}{\partial n} dS = 0 \quad (5.8)$$

the first term in the right hand side of (5.7) does not have influence on the total energy functional and hence can be neglected. So (5.7) reduces to

$$F^e(\psi^e) = -\frac{1}{2} \iiint_{V_e} \mu^e \nabla \psi^e \cdot \nabla \psi^e dV \quad (5.9)$$

Substitute the expansion (of hexahedral element)

$$\psi^e = \sum_{j=1}^8 N_j^e(x, y, z) \psi_j^e \quad (5.10)$$

into (5.9), we have

$$F^e(\psi^e) = -\frac{1}{2} \iiint_{V_e} \mu^e \left[\left(\sum_{j=1}^8 \frac{\partial N_j^e}{\partial x} \psi_j^e \right)^2 + \left(\sum_{j=1}^8 \frac{\partial N_j^e}{\partial y} \psi_j^e \right)^2 + \left(\sum_{j=1}^8 \frac{\partial N_j^e}{\partial z} \psi_j^e \right)^2 \right] dV \quad (5.11)$$

The functional is minimized by enforcing each of the partial derivatives of F^e with respect to ψ_i^e ($i = 1, 2, \dots, 8$) to be zero, i.e.,

$$\frac{\partial F^e(\psi^e)}{\partial \psi_i^e} = -\sum_{j=1}^8 \psi_j^e \iiint_{V_e} \mu^e \left(\frac{\partial N_i^e}{\partial x} \frac{\partial N_j^e}{\partial x} + \frac{\partial N_i^e}{\partial y} \frac{\partial N_j^e}{\partial y} + \frac{\partial N_i^e}{\partial z} \frac{\partial N_j^e}{\partial z} \right) dV = 0 \quad (5.12)$$

(5.12) can be written in a compact matrix form as

$$[S^e] \{\psi^e\} = \{b^e\} \quad (5.13)$$

with the entries

$$S_{ij}^e = \iiint_{V_e} \mu^e \left(\frac{\partial N_i^e}{\partial x} \frac{\partial N_j^e}{\partial x} + \frac{\partial N_i^e}{\partial y} \frac{\partial N_j^e}{\partial y} + \frac{\partial N_i^e}{\partial z} \frac{\partial N_j^e}{\partial z} \right) dV \quad (5.14)$$

$$b^e = 0 \quad (5.15)$$

The hexahedral element in the xyz coordinate system can be transformed into cubic element in the $\xi\eta\zeta$ coordinate system, in which the interpolation functions have much simpler forms and (5.14) is much easier to be evaluated.

In the presence of permanent magnets (PMs), the governing equation is modified to [151]

$$\nabla \cdot \mu \nabla \psi = \nabla \cdot \mathbf{B}_r \quad (5.16)$$

The energy functional becomes

$$F(\psi) = \frac{1}{2} \langle L\psi, \psi \rangle - \langle \psi, f \rangle \quad (5.17)$$

with

$$f = \nabla \cdot \mathbf{B}_r \quad (5.18)$$

Substitute the operator and (5.18) into (5.17), we have

$$F(\psi) = \frac{1}{2} \iiint_{V} \psi \nabla \cdot \mu \nabla \psi dV - \iiint_{V} \psi \nabla \cdot \mathbf{B}_r dV \quad (5.19)$$

The first term in the right hand side of (5.19) is the same as in the case without permanent magnets. The second term, denoted as

$$F_2(\psi) = -\iiint_V \psi \nabla \cdot \mathbf{B}, dV \quad (5.20)$$

is due to permanent magnets. As we will see in the following, (5.20) is treated as Neumann boundary condition. (5.20) can be simplified to [151]

$$F_2(\psi) = -\oiint_Y \psi \mathbf{B}_r \cdot d\mathbf{S} \quad (5.21)$$

In the MFL pig, \mathbf{B}_r is uniform in the PMs and only along the radial direction, i.e.,

$$F_2(\psi) = -\oiint_Y \psi \mathbf{B}_r \cdot d\mathbf{S} = -B_r \iint_Y \psi dS \quad (5.22)$$

in which Y denotes the pole faces that are perpendicular to the radial direction. The functional can also be expressed as

$$F_2(\psi) = \sum_{s=1}^{M_Y} F_2^s(\psi^s) \quad (5.23)$$

with

$$F_2^s(\psi^s) = -B_r \iint_{Y_s} \psi^s dS \quad (5.24)$$

In the above, M_Y is the number of elements in Y . Substitute the expansion of the rectangular element in the pole surfaces

$$\psi^s = \sum_{j=1}^4 N_j^s \psi_j^s \quad (5.25)$$

into (5.24), we have

$$F_2^s(\psi^s) = -\sum_{j=1}^4 B_r \iint_{Y_s} N_j^s \psi_j^s dS \quad (5.26)$$

The functional is minimized by enforcing each of the partial derivatives of F_2^s with respect to ψ_i^s ($i = 1, 2, \dots, 4$) to be zero, i.e.,

$$\frac{\partial F_2^s(\psi^s)}{\partial \psi_i^s} = -B_r \iint_r N_i^s dS = -\frac{1}{4} B_r S_s, \quad (5.27)$$

By equating the partial derivatives to zero, we have the elemental matrix equation as

$$[K^s] \{\psi^s\} = \{b^s\} \quad (5.28)$$

with the entries

$$b^s = -\frac{1}{4} B_r S_s, \quad (5.29)$$

$$K^s = 0 \quad (5.30)$$

$\{\psi^s\}$ and $\{b^s\}$ are then assembled to the global stiffness matrix and global load vector.

5.2.2 Nonlinear Calculation

An iterative scheme is employed to model the nonlinear magnetization property of the ferromagnetic pipe wall:

Step 1. Assume initial values of permeabilities in steel;

Step 2. Solve the linear problem for magnetic scalar potential ψ ;

Step 3. Calculate field intensity H in each element in steel from ψ ;

Step 4. Calculate flux density B in each element in steel from H by interpolating the $B - H$ curve;

Step 5. Update permeability in each element in steel;

Step 6. If the change of permeabilities with respect to permeabilities in the previous iteration is not small enough, go to Step 2; otherwise, the process is said to be converged.

The $B - H$ curve obtained experimentally is very noisy. A smoothing method, named Kalman smoothing, is used to make the curve smooth. The curve is then extended to sufficiently high H such that the dynamic permeability dB/dH is identically μ_0 , the permeability in free space. Figure 5.5 shows a typical processed initial magnetization curve.

Permeabilities in the pipe wall are updated in the following way:

$$\mu_{new}(j) = \mu_{old}(j) + (\mu_i(j) - \mu_{old}(j)) \cdot vfac \quad (5.31)$$

where $j = 1, 2, 3, \dots, M_p$ is the element index in the ferromagnetic specimen with M_p the number of elements in the pipe wall; μ_{old} is the permeability obtained in the previous iteration; μ_i is the permeability obtained by interpolation in the current iteration; μ_{new} is the new permeability; $vfac$ is the factor controlling the rate of convergence. If $vfac$ is chosen too large, convergence may not be smooth. If $vfac$ is chosen to be too small, convergence may be

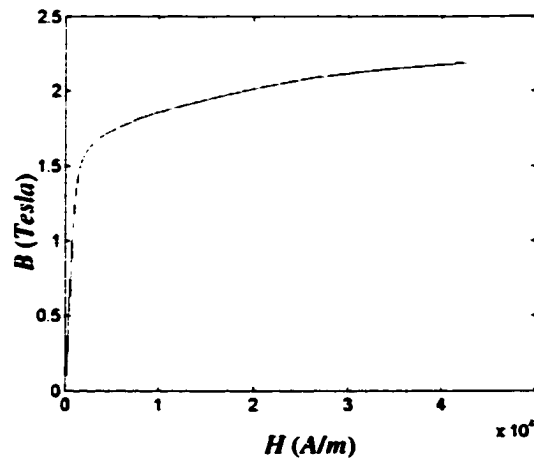


Figure 5.5 A typical initial magnetization curve of pipe wall

slow. In practice, we choose $vfac$ to be large, say 1, in the first few iterations, and then make it smaller thereafter.

5.2.3 Procedure of Modeling

The process of pipeline inspection involves pulling the MFL pig through the pipeline. In the finite element model, this process is implemented by moving the defect, which is much easier, in each step instead of moving the pig.

The procedure of finite element modeling is illustrated in Figure 5.6, in which the variable $step$ indicates the current step of moving the defect and $Nstep$ is the total number of steps. In each defect position, the nonlinear calculation as described above is performed. $iter$ indicates the current iteration number. The iterative process stops if the maximum relative change of permeabilities in steel is smaller than the desired accuracy est or the process has reached the maximum allowed iteration number $Niters$.

Figure 5.7 shows the axial component of a typical collected signal.

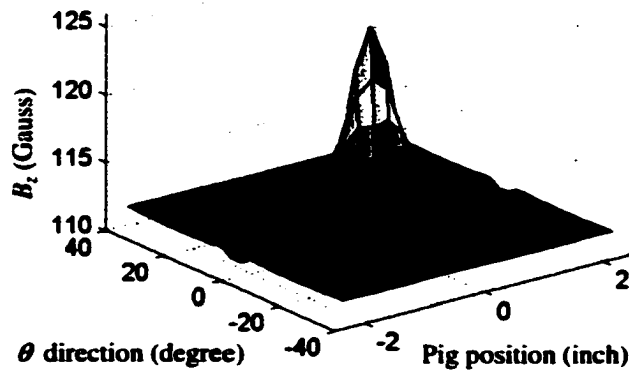


Figure 5.7 Axial component of a typical signal

5.3 Application of POD Model

Three factors: radial liftoff, magnetization level, and sensor spacing are recognized as the major variabilities that have much influence on the probability of detection in pipeline inspection. In this section, POD studies with respect to these factors will be discussed.

5.3.1 POD with respect to radial liftoff

Radial liftoff, also referred to as liftoff for simplicity, is defined as the distance from a sensor to the inner surface of the pipe wall. Two defects (referred to as Flaws A and B) are used for the POD study with respect to liftoff. Flaw A is a 0.5"×0.5" rectangular defect of 15% depth and 45° surface angle. Flaw B is a 1"×1" rectangular defect of 35% depth and 45° surface angle. The pipe wall thickness for both Flaws A and B is 0.344". The magnetization level is $B_r = 1.6 T$.

The signal magnitudes with Flaw A, Flaw B, and without any flaw at different liftoffs are plotted in Figure 5.8. A 3rd order polynomial curve is employed to create the functional model. The polynomial coefficients for the 3rd order polynomials

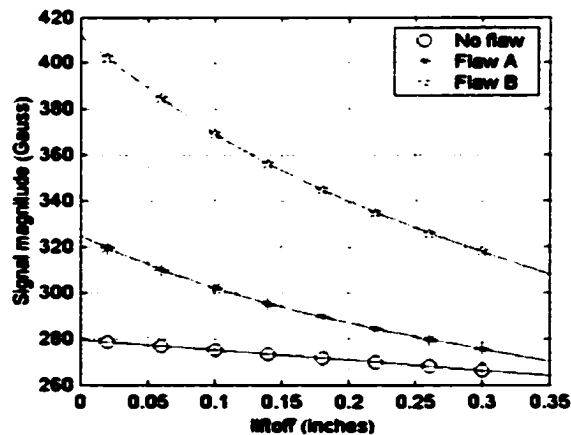


Figure 5.8 Signal magnitudes for different liftoffs, with $B_r=1.6 T$

Table 5.1 Polynomial coefficients of the functional model for liftoff

Flaw	Functional Model ($y = ax^3 + bx^2 + cx + d$)			
	a	b	c	d
No Flaw	-2.20959	-5.52049	-40.92598	279.29731
Flaw A	-594.02619	555.04701	-278.44182	324.92721
Flaw B	-893.38699	917.09956	-509.29118	411.98840

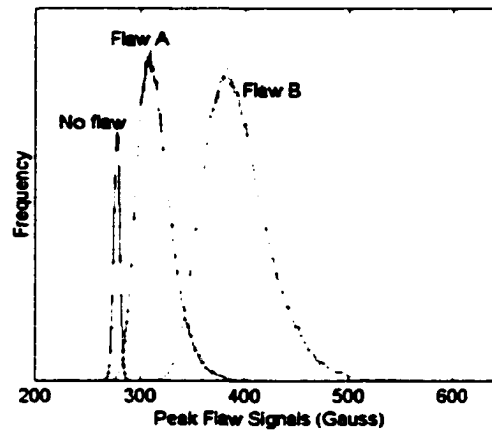


Figure 5.9 pdf of signal magnitudes with mean liftoff 0.05"

$$y = ax^3 + bx^2 + cx + d \quad (5.32)$$

for Flaw A, Flaw B, and no flaw are listed in Table 5.1.

Assuming a Gaussian distribution (input pdf) of liftoff variation to have a selected mean and a variance 10% of the mean, the corresponding conditional pdf's of signal magnitudes for Flaw A, Flaw B, and no flaw are obtained using the above functional model. Since the functional models are nonlinear, the signal magnitude distributions, as shown in Figure 5.9, are not Gaussian. Figure 5.9 shows the pdfs when the mean liftoff equals 0.05". In this case, if the threshold is set to 280 Gauss, the POD for Flaws A and B are found as 0.998 and 1.000, respectively. The corresponding PFA for both Flaws A and B is found as 0.170. If, however,

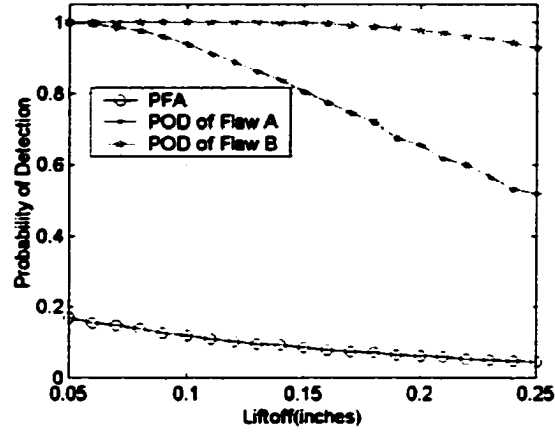


Figure 5.10 POD and PDF curves for different liftoffs, with $T = 280$ Gauss

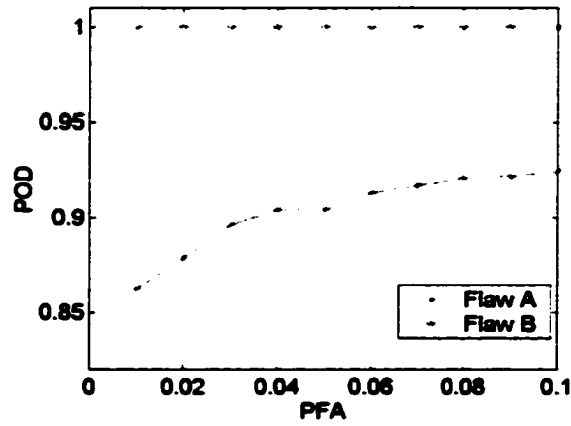


Figure 5.11 POD curves for different liftoffs, with $PFA = 5\%$

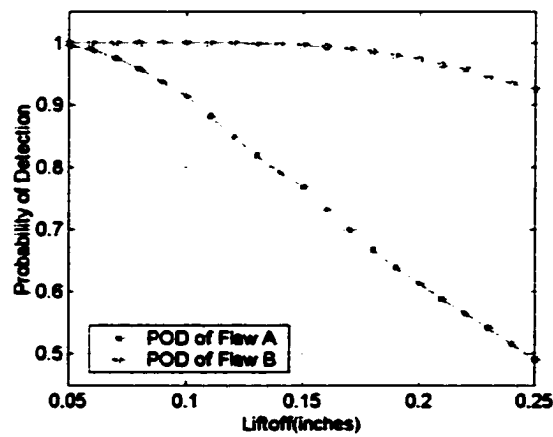


Figure 5.12 ROC curve, with liftoff = 0.1"

the PFA is set to 5%, the threshold is found to be 282 Gauss, and the POD for Flaws A and B are 0.995 and 1.000, respectively. Figure 5.10 shows the POD and PFA curves with respect to different liftoffs for the two flaws when the threshold is fixed at 280 Gauss. Figure 5.11 shows the POD curves when the threshold is obtained by fixing PFA to 5%. As expected, the POD decreases monotonically when liftoff increases.

Figure 5.12 is the relative operating characteristic, which shows the relationship between POD and PFA, when the liftoff is 0.1". For Flaw A, with increasing PFA, the threshold decreases, thus increasing the POD. The POD for Flaw B is always one when liftoff is 0.1".

5.3.2 POD with respect to magnetization level

Magnetization level, denoted by B_r , is a design parameter characterizing the strength of the permanent magnets. Two defects are used for POD study with respect to magnetization level. Flaw A is a 1"×1" rectangular defect of 35% depth and 45° surface angle, and Flaw B is a 2"×2" rectangular defect of 35% depth and 45° surface angle. The wall thickness for both flaws is 0.344". The liftoff is chosen as 0.02".

The signal magnitudes with Flaw A, Flaw B, and without any flaw at different magnetization levels are plotted in Figure 5.13. The signal magnitude in the absence of any flaw is just the background level. Although the curves in Figure 5.13 appears to be linear, they are in fact, nonlinear, as can be seen by observing the difference between the magnitudes (peak values) and the background levels, as shown in Figure 5.14. The nonlinearity occurs due to saturation when the magnetization level is high.

A 4th order polynomial curve is employed to create the functional model. The polynomial coefficients for the 4th order polynomials

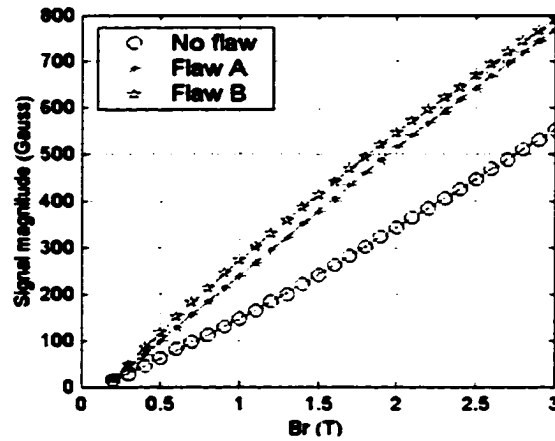


Figure 5.13 Signal magnitudes for different magnetization levels, with 0.02'' liftoff

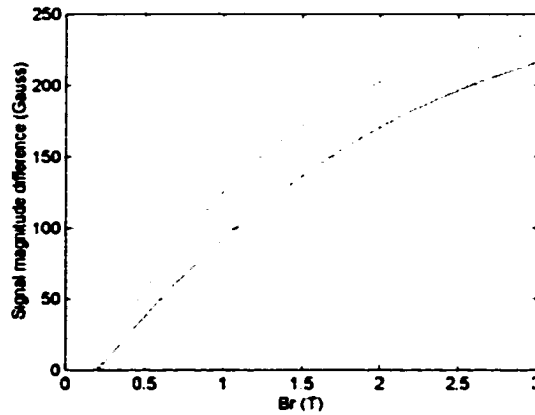


Figure 5.14 Magnitude difference between signals with flaw and without flaw

$$y = ax^4 + bx^3 + cx^2 + dx + e \quad (5.33)$$

for Flaw A, Flaw B, and no flaw are listed in Table 5.2.

Assuming a Gaussian distribution of input magnetization levels with the variance of 2% of the mean, the corresponding pdf's of signal magnitudes for Flaw A, Flaw B, and no flaw are obtained using the above functional model. Figure 5.15 shows the pdf's with the mean magnetization level set to 1.5T. In this case, if the threshold is set to 300 Gauss, the POD for Flaw A and Flaw B are found to be 0.951 and 0.991, respectively. The PFA for both Flaw A

Table 5.2 Polynomial coefficients of the functional model for magnetization level

Flaw	Functional Model ($y = ax^4 + bx^3 + cx^2 + dx + e$)				
	a	b	c	d	e
No Flaw	-0.02532	0.12476	-0.05477	1.62583	-0.19442
Flaw A	0.00891	-0.07433	0.12715	2.74721	-0.40946
Flaw B	-0.00232	0.06272	-0.45792	3.69646	-0.56746

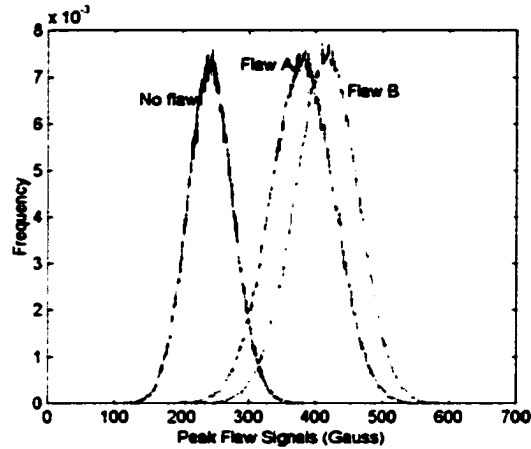


Figure 5.15 pdf of signal magnitudes with mean magnetization level 1.5T

and Flaw B is 0.046. If, however, the PFA is set to 5%, the threshold is found as 299 Gauss, and the POD for Flaw A and Flaw B are 0.952 and 0.991, respectively.

In [96, 104] the POD is reported to increase with increasing magnetization level and then decrease when the magnetization level is greater than a particular value. The conclusion of this study is that the POD reaches its maximum before getting saturated. However, this is not true, because in [96, 104], the background is subtracted from the measurement values, and the difference is used instead of the measurement values as signal magnitudes. Our research, as presented in the following, shows that the higher the magnetization level, the more possible a defect can be detected.

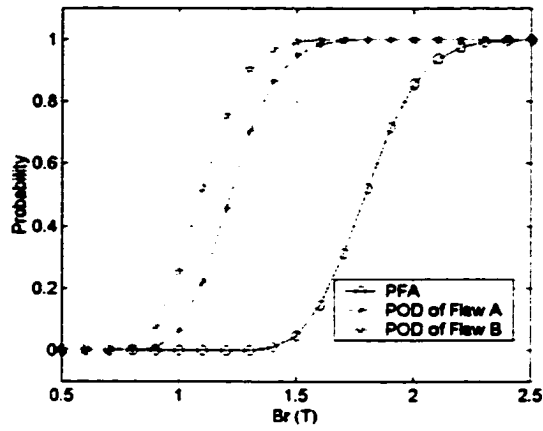


Figure 5.16 POD and PDF curves for different magnetization levels, with $T = 300$ Gauss

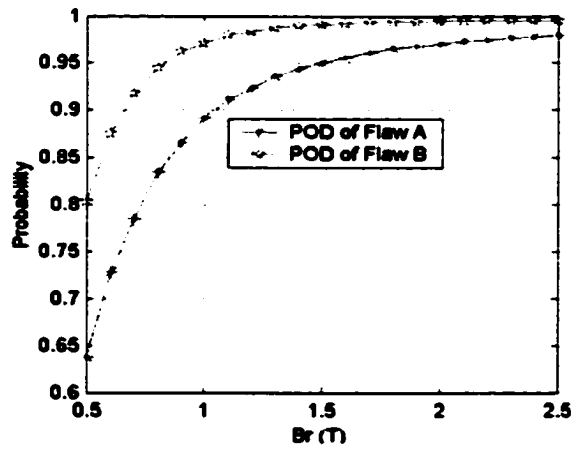


Figure 5.17 POD curves for different magnetization levels, with $PFA = 5\%$

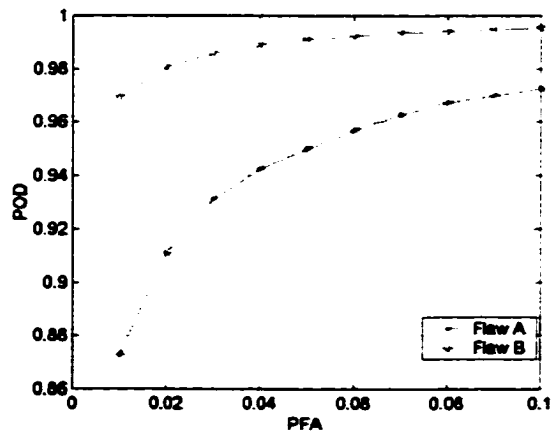


Figure 5.18 ROC curve, with $Br=1.5T$

Figure 5.16 shows the POD and PFA curves with respect to different magnetization levels for the two flaws when the threshold is fixed at 300 Gauss. Figure 5.17 shows the POD curves obtained when the PFA is fixed at 5%. As observed from the figures, POD increases monotonically with magnetization level. Figure 5.18 shows the ROC curves when the magnetization level is 1.57.

5.3.3 POD with respect to sensor spacing

For each run of the pig through the pipe, the position of the sensor array with respect to the defect may be different due to randomness in the pig orientation. Thus the measured signals are different for each run. This problem is related to sensor spacing. Sensor spacing, denoted as S_i , is the distance between adjacent sensors in the circumferential direction, as shown in Figure 5.19. If there is no perturbation in the sensor positions, there is a sensor exactly under the center of the defect. We set this position to be the origin where the circumferential distance between defect and sensor is 0. We can then define the perturbation d as the distance the sensor shifts from the origin.

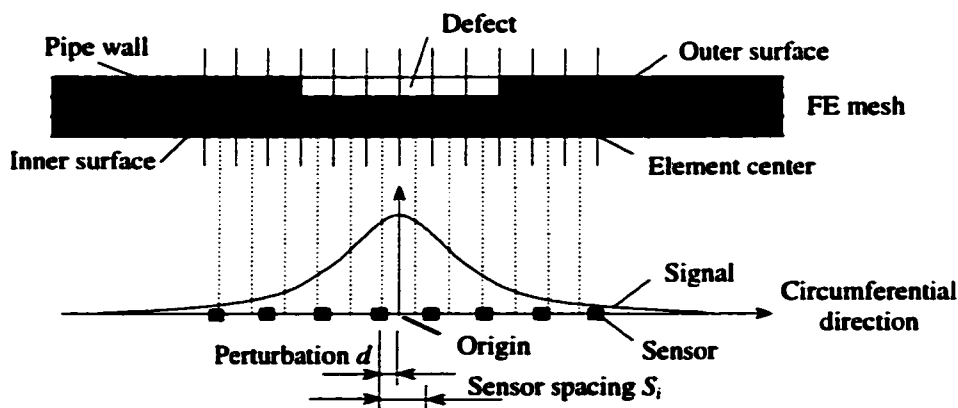


Figure 5.19 Illustration of sensor spacing and perturbation

An infinite number of sensors along the circumferential direction will yield a continuous signal. In practice, however, the number of sensors is finite and the measured signal is a sampled version of the continuous signal in the circumferential direction. In the case of the FEM signal shown in Figure 5.7, the sensor spacing S_0 is exactly equal to the element size in the circumferential direction. The maximum perturbation d is therefore $\pm S_0/2$.

Peak values of signals with arbitrary sensor spacing S_i and perturbation d can be obtained from the FEM signal using 2-D spline interpolation. In order to obtain a smooth distribution, a large number of signals from different perturbations need to be generated. For each value of perturbation, a 2-D interpolation needs to be performed, which is computationally expensive. Since we are interested in the peak value of the signal, we can consider only 1-D signals (and correspondingly, 1-D interpolation) along the circumferential direction at the center of the flaw in order to reduce the computational effort. An example is shown in Figure 5.20. The peak values at different perturbations can be found by interpolating the 1-D signal. So, the functional model in Figure 4.4 is actually a 1-D interpolation process.

A 0.5"×0.5" rectangular defect, of 15% depth and 45° surface angle, is used in POD

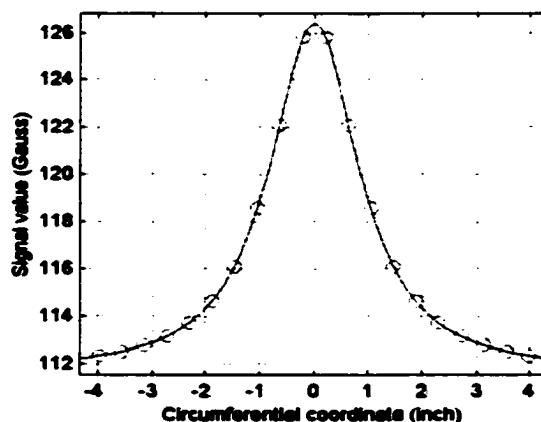


Figure 5.20 1-D Signal interpolation in the circumferential direction

study with respect to sensor spacing. The thickness of the pipe wall is 0.344". The radial liftoff is set to 0.02" according to the finite element mesh, and the magnetization level is set to $B_r = 0.8T$. We choose a small defect relative to sensor spacing with small magnetization level because a large defect with large magnetization levels will always result in a POD equal to one due to the strong signal.

Since the signal is periodic with respect to perturbation, we assume that the perturbation is distributed uniformly in the range of $[-S_i/2, S_i/2)$. Thus the mean and variance of the perturbations are 0 and $S_i^2/12$ respectively. The corresponding distribution of signal magnitudes is obtained by interpolating the FEM signal, as described above. When there is no flaw in the pipe, the signal magnitude is just the background level, which is a constant, regardless of the perturbation. In practice, however, the measured signal without a flaw is corrupted by random measurement noise, here assumed to be Gaussian. This noise is also imposed on the signal with a defect, because the measurement noise is independent of the presence of a defect. Figure 5.21 shows the pdf's of peak values with and without a defect. In

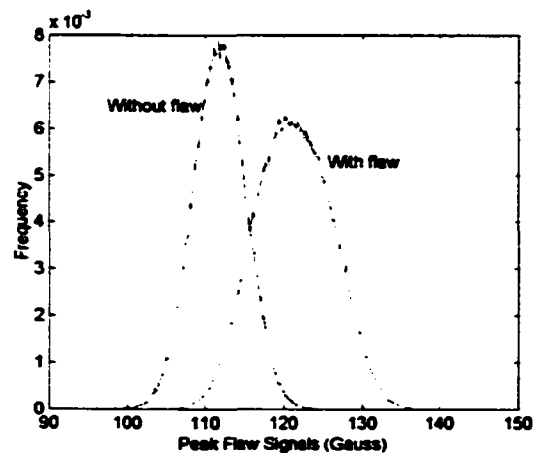


Figure 5.21 pdf of signal magnitudes with mean sensor spacing 3"

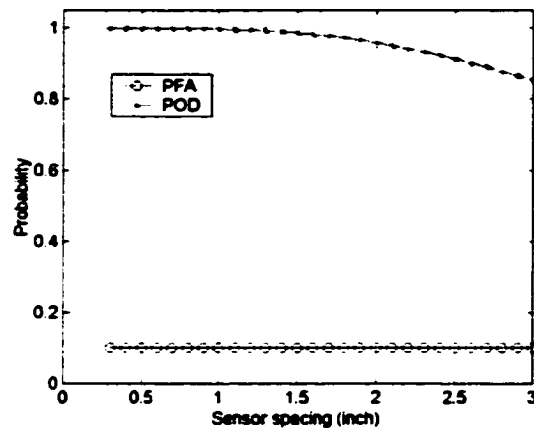


Figure 5.22 POD and PDF curves for different sensor spacing, with $T = 116$ Gauss

Figure 5.21, the variance of the noise is set to 10% of the background level. The POD and PFA with respect to sensor spacing can be calculated using (4.1) and (4.2). If the threshold is set to 116 Gauss to minimize the classification error, the POD is 0.852, and the PFA is 0.102. If the PFA is set to 5%, the threshold is found to be 117.2 Gauss, and the POD is 0.778.

Figure 5.22 shows the POD and PFA curves with respect to different sensor spacing when the threshold is fixed at 116 Gauss. The PFA is constant since the background level and noise are independent of sensor spacing. POD decreases monotonically when sensor spacing increases. Figure 5.23 shows the POD curve obtained when PFA is fixed at 5%. Again, POD decreases monotonically with increasing sensor spacing. Figure 5.24 shows the ROC curve when the sensor spacing is 3".

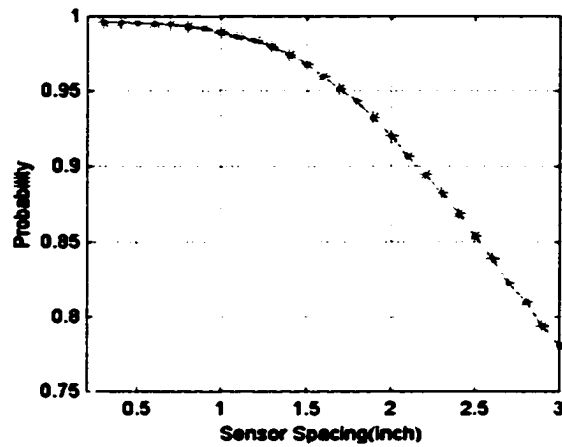


Figure 5.23 POD for different sensor spacing, with $PFA = 5\%$

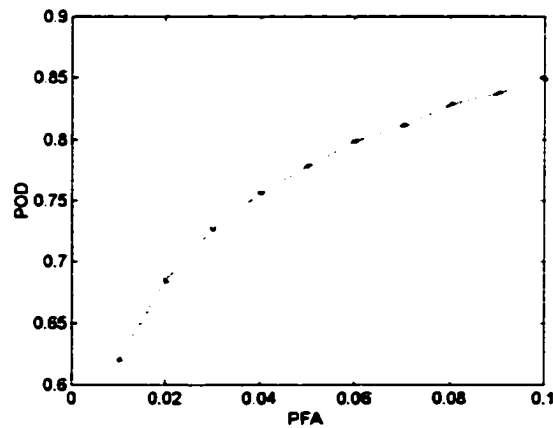


Figure 5.24 ROC curve, with 3" sensor spacing

5.4 Application of Taguchi Methods

5.4.1 Design and Conduct Experiments

Four factors with two levels each were first identified in this study. Based on prior experience, magnetization level, sensor spacing, radial liftoff, and perturbation (circumferential shift) between sensor and defect, as defined in the previous section, have

Table 5.3 Factors and levels

Factors		Levels	
		Level 1	Level 2
Controllable	Magnetization level (A)	0.8T	1.2T
	Sensor spacing (B)	1"	2"
Uncontrollable	Radial liftoff	0.05"	0.1"
	Perturbation	0	25% of sensor spacing

Table 5.4 Experiment design and results

Inner Array		Outer Array				Results (PODs)					
		Noise Factors	Col 1	2	3						
Column	Trial	1	2	3	1	2	3	4	Mean	Std. Dev.	S/N
	1	1	1	0	0.8640	0.8372	0.7736	0.7202	0.7988	0.0646	12.5729
	2	1	2	0	0.8640	0.7330	0.7202	0.5879	0.7263	0.1128	10.7324
	3	2	1	0	0.9923	0.9867	0.9504	0.9328	0.9655	0.0286	27.4408
	4	2	2	0	0.9923	0.9504	0.9504	0.8598	0.9382	0.0559	22.1044

obvious influences on the measured signal. The factors can be classified into controllable or uncontrollable (noise) factors, depending on whether or not its level can be easily controlled under practical conditions. Magnetization level and sensor spacing are controllable factors, while radial liftoff and perturbation are considered as uncontrollable factors. Although radial liftoff and circumferential shift are hard to control in practical operations, they are under control in lab conditions and varied systematically to represent their variation in a practical situation. Table 5.3 lists the factors and levels.

Table 5.4 shows the inner and outer orthogonal arrays used in the Taguchi study. Note that the last columns of both the inner array and the outer arrays in Table 5.4 are not used, because we have only two controllable and two uncontrollable factors. With the factors and

levels chosen as shown in Table 5.3, the number of experiments is the same as that of full factorial design. However, the method will be more efficient if more factors and/or more levels are considered in future research.

A $0.5'' \times 0.5''$ rectangular defect, of 15% depth and 45° surface angle, is used as the critical defect in this Taguchi study.

To obtain complete data, each trial run of the inner array must be repeated for each of the four noise combinations (in outer array). That is, the experiments consist of the computation of POD for each combination of magnetization level, sensor spacing, radial liftoff and circumferential shift.

FEM simulations are performed to predict signals. With each simulation of the FEM at a particular magnetization level, we obtain a signal in the 3-D space (radial, circumferential, and axial). Note that, experimentally, we can only obtain a 2-D signal at a particular radial liftoff, while signals at different radial liftoffs are available at the same time via simulation. Since we are interested in the peak value of the signal, we can consider only the signal at the center (in the axial direction) of the flaw. The 2-D (perpendicular to the axial direction with axial coordinate at the center of the flaw) signals with $B_r = 0.8\text{T}$ and 1.2T are shown in Figures 5.25 (a) and (b).

For each run of the inspection tool, we can find signal magnitudes at arbitrary radial liftoff and circumferential shift using 2-D interpolation. Note that there is measurement noise present in the signal, which is independent of any of the four factors being considered. This common measurement noise should be taken into account when calculating the 16 PODs. Typically, we assume the noise to be Gaussian with zero mean and variance 25 Gauss.

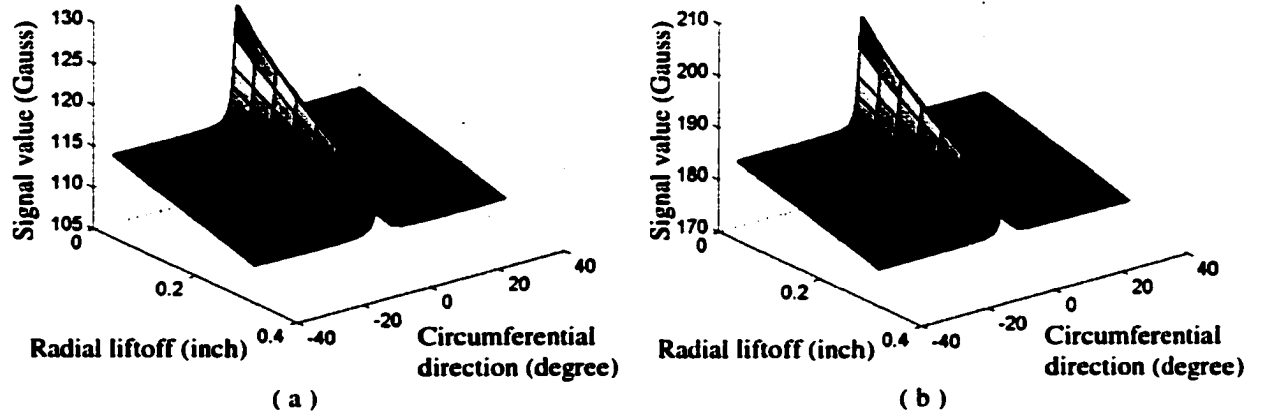


Figure 5.25 2-D signals in the surface perpendicular to the axial direction at the center of the flaw
 (a) $B_r = 0.8T$ (b) $B_r = 1.2T$

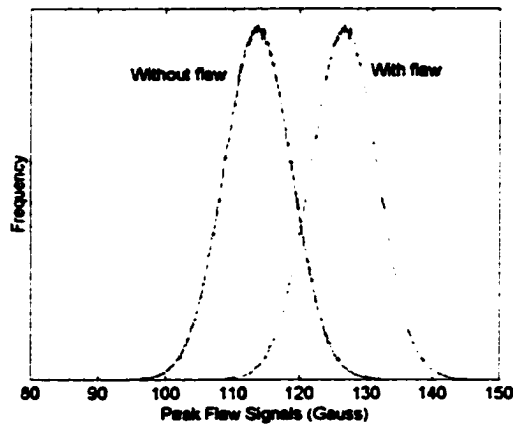


Figure 5.26 pdf of signal magnitudes with and without flaw
 when $B_r = 0.8T$, sensor spacing is $1''$, radial liftoff equals $0.05''$,
 and zero circumferential shift

Conducting each of the 16 simulations in Table 5.4, pdf's of measurement outputs with and without flaw were found. Figure 5.26 presents the pdf's of measurement outputs when $B_r = 0.8T$, sensor spacing = 1", radial liftoff = 0.05" and circumferential shift = 0. The POD and PFA can then be calculated using (4.1) and (4.2). The threshold was selected so that the PFA is 5%. All 16 PODs with the computed signal to noise ratios are shown in Table 5.4.

5.4.2 Analyses

5.4.2.1 Optimal Parameters

The signal to noise ratios, along with the means and standard deviations for each of the design settings are calculated and given along with the PODs in Table 5.4. We find in the table that the 3rd design setting, magnetization level at Level 2 (1.2 Tesla) and sensor spacing at Level 1 (1 inch), is optimal and most robust with respect to noise variations because its mean POD is the largest and it has the smallest standard deviation. The signal to noise ratio also reaches its maximum at the 3rd trial, which indicates that this set of design parameters is the one that we are seeking for.

5.4.2.2 Main Effects

The main effects of magnetization level and sensor spacing are computed using (4.25) and (4.26) and listed in Table 5.5 and plotted in Figure 5.27.

From the last column of Table 5.5, we find that the magnetization level has more influence than the sensor spacing for the defect under consideration. Meanwhile, from Table 5.5 and Figure 5.27, we find that \bar{A}_2 is greater than \bar{A}_1 , \bar{B}_1 is greater than \bar{B}_2 . This leads to

Table 5.5 Main Effects for S/N analysis

Factors	Level 1 (d_1)	Level 2 (d_2)	d_2-d_1
Magnetization level (A)	11.653	24.773	13.120
Sensor spacing (B)	20.007	16.418	-3.589

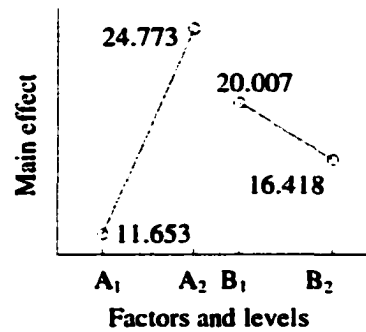


Figure 5.27 Main effects for S/N analysis

the same conclusion as in the above subsection that the optimum condition among the four possibilities is A_2B_1 . That is, among all the four trial conditions, the maximum POD is obtained at a magnetization level of 1.2T and sensor spacing of 1". In fact, the higher the magnetization level, the greater the POD, if other conditions are the same. Also POD increases monotonically when sensor spacing decreases while other conditions are kept constant.

5.4.2.3 Analysis of Variance

Following the standard steps of ANOVA described in Chapter 4 and using Formulations (4.27) through (4.40), the statistical quantities were calculated and summarized in Table 5.6.

The F values obtained in this study are $F_A = 56.34$, $F_B = 4.22$, $F_c = 1$. Assuming a confidence level of 90%, the F values determined from the F - table for both Factors A and B

Table 5.6 ANOVA table without pooling

Column	Factor	f	S	V	F	P (%)
1	Factor A	1	172.13	172.13	56.34	89.90
2	Factor B	1	12.88	12.88	4.22	5.22
	All other/error	1	1	3.06	3.06	
	Total	3	3	188.07		

f: degrees of freedom S: sum of squares V: variance
F: variance ratio P: Percent contribution

Table 5.7 ANOVA table with pooling

Column	Factor	f	S	V	F	P (%)
1	Factor A	1	172.13	172.13	21.61	87.29
2	Factor B	(1)	(0.102)	Pooled		
	All other/error	2	15.93	7.97		12.71
	Total	3	188.07			100.00

f: degrees of freedom S: sum of squares V: variance
F: variance ratio P: Percent contribution

are $F_{0.1}(1,1) = 39.864$, where the two parameters in the parentheses are DOF of Factor A and DOF of the error term, respectively. Since $F_A > F_{0.1}(1,1) > F_B$, Factor A (magnetization level) does contribute to the sum of squares at the confidence level of 90%, while Factor B (sensor spacing) does not contribute to the sum of squares within this confidence level. If the confidence level is chosen to be 95%, the F values determined from the F - table for the two factors are $F_{0.05}(1,1) = 161.45$. Since both F_A and F_B are smaller than this value, both factors do not contribute to the sum of squares within the 95% confidence level.

In Table 5.6, we find that the percent contribution of Factor B (sensor spacing) is only 5.22%. Thus Factor B can be pooled to increase the statistical significance of important factor. The ANOVA table (Table 5.7) lists the new analysis results with Factor B being pooled using (4.41). The percent contribution of Factor A is now 87.29%. The contribution of errors is 12.71%.

These results were obtained by considering a $0.5'' \times 0.5'' \times 15\%$ deep critical defect. This defect was chosen on the basis of the smallest element in the FE mesh. If the critical defect is smaller, the sensor spacing will have a greater effect on the POD.

CHAPTER 6 APPLICATION TO MAGNETO-OPTIC/EDDY CURRENT IMAGING

6.1 Introduction

The Magneto-optic Imaging (MOI) is a relatively new non-destructive evaluation technique for detecting subsurface cracks and corruptions in aircraft skin structures. The technique involves inducing eddy currents into the test specimen and detecting the magnetic flux associated with eddy current distribution in the specimen by exploiting the Faraday rotation effect. If the test specimen is homogeneous, the associated magnetic flux is tangential to the specimen surface. Anomalies in the specimen result in the generation of a normal component of the magnetic flux density. The magneto-optic sensor then produces an easy-to-interpret and real-time binary-valued image of the local magnetic fields associated with the anomalies. More details about the principles of MOI are provided in the next section.

A 3-D finite element model of MOI inspection using A - v formulation has been developed where A and v denote the magnetic vector potential and electric scalar potential respectively. The numerical model offers the capability to examine the effects of individual and multiple parameters that are expensive to obtain experimentally. Three typical types of flaws in aircraft skin structures have been modeled, namely, radial crack, circumferential crack and fastener-to-fastener crack. The formulations and predicted results are provided in Section 6.3. Numerical results in the case of radial cracks are used for parametric study, POD study and Taguchi study in this chapter.

To evaluate the performance of an MOI system under given measurement conditions, the concept of skewness is introduced to quantify the strength of the field/ flaw interaction embedded in the binary MO image. The definition of the coefficient of skewness of binary MO image is presented in Section 6.4.

The skewness of binary MO image is affected by a number of test parameters such as the value of the thresholding bias and the frequency of the excitation current. A parametric study is conducted to determine the effects of the variations of these parameters on the skewness of binary MO images, which is discussed in Section 6.5.

In Section 6.6, the model-based POD evaluation technique is modified for MOI applications in which inspectors make accept/reject decisions by simply observing MO images. The new approach utilizes the concept of degree of certainty to reflect the human decisions. Parametric studies are performed to determine the effects of the variations in threshold and frequency individually on the probability of detecting a critical crack.

Finally, Section 6.7 utilizes these results in the Taguchi analysis for seeking the optimum set of test parameters in the MOI inspection. Ideally, one would like to have maximum value of skewness. In the meanwhile, the performance of MOI is expected to be most robust to the variations of the parameters. Sometimes the resultant sets of parameters are contradictory. The Taguchi method provides a tradeoff by the means of signal to noise ratio analysis. The number of trials necessary for the optimization is significantly reduced with Taguchi's methodology of experimental design.

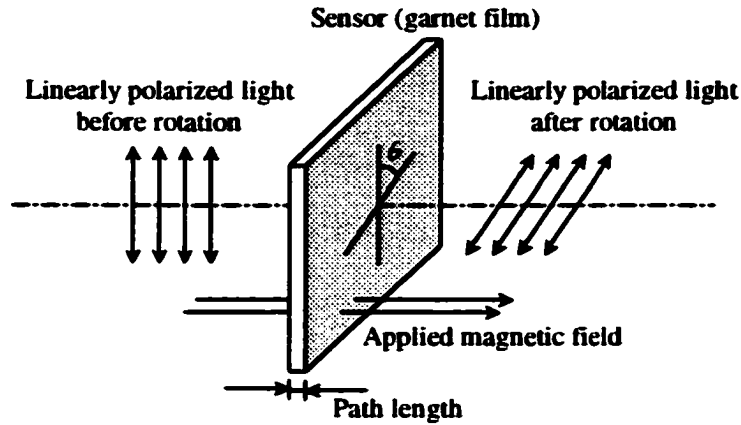


Figure 6.1 Faraday rotation effect

6.2 Principles of MOI

The operational principles of magneto-optic imaging is partially based on the Faraday rotation effect, which states that the plane of polarization of a linearly polarized light transmitting through a certain material in the direction of an applied magnetic field is rotated, with the amount of rotation proportional to the path length and the strength of the magnetic field, as illustrated in Figure 6.1. The magneto-optic sensor used in the MO instrument consists of a garnet film that has a magnetic anisotropy property with an “easy” axis of magnetization normal to the sensor surface and a “hard” axis of the magnetization in the plane of the sensor. Here “easy” and “hard” axes mean that the sensor is very sensitive and insensitive, respectively, to magnetic fields along these directions [158].

Figure 6.2 shows a schematic of the MOI inspection system. An induction foil carrying alternating current is used to induce eddy current into the test specimen. The magnetic field generated by the eddy current is tangential to the specimen surface if the specimen is homogeneous. In this case, the linearly polarized light is not rotated. If, however, there are anomalies in the specimen, such as holes, fasteners and cracks, the induced current is

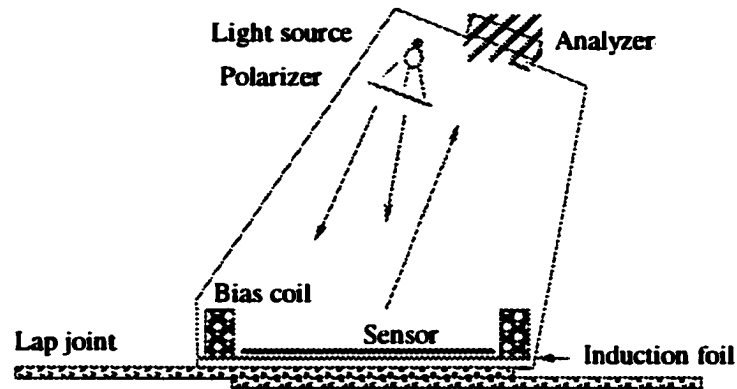


Figure 6.2 Schematic of MOI instrument

distorted. The resultant magnetic field has a component normal to the specimen surface or sensor surface. The polarization plane of the polarized light is therefore rotated by the sensor and a footprint or image of the normal magnetic flux densities is then generated, as a dark (lack of light signal) patch.

The process of generating binary MO image in the presence of anomalies in the specimen is illustrated in Figures 6.3 (a) through (e). A hole or a rivet is assumed to be present in the test specimen. Since the induced eddy currents cannot go through the hole or the air gap surrounding the rivet, they are redistributed around the hole, as shown in Figures 6.3 (a) and (c). Figures 6.3 (a) shows the induced eddy currents and leakage fields during the first half cycle of the excitation current. In some region, the normal components of leakage fields are strong enough (greater than the threshold value) to flip the domain in the garnet sensor film and generate a binary image, as shown in Figure 6.3 (b). During the second half cycle of the excitation current, the directions of the induced eddy currents and leakage fields are opposite to those generated during the first cycle and another binary image is obtained, as shown in Figures 6.3 (c) and (d). The time interval between the two adjacent half cycles is so small

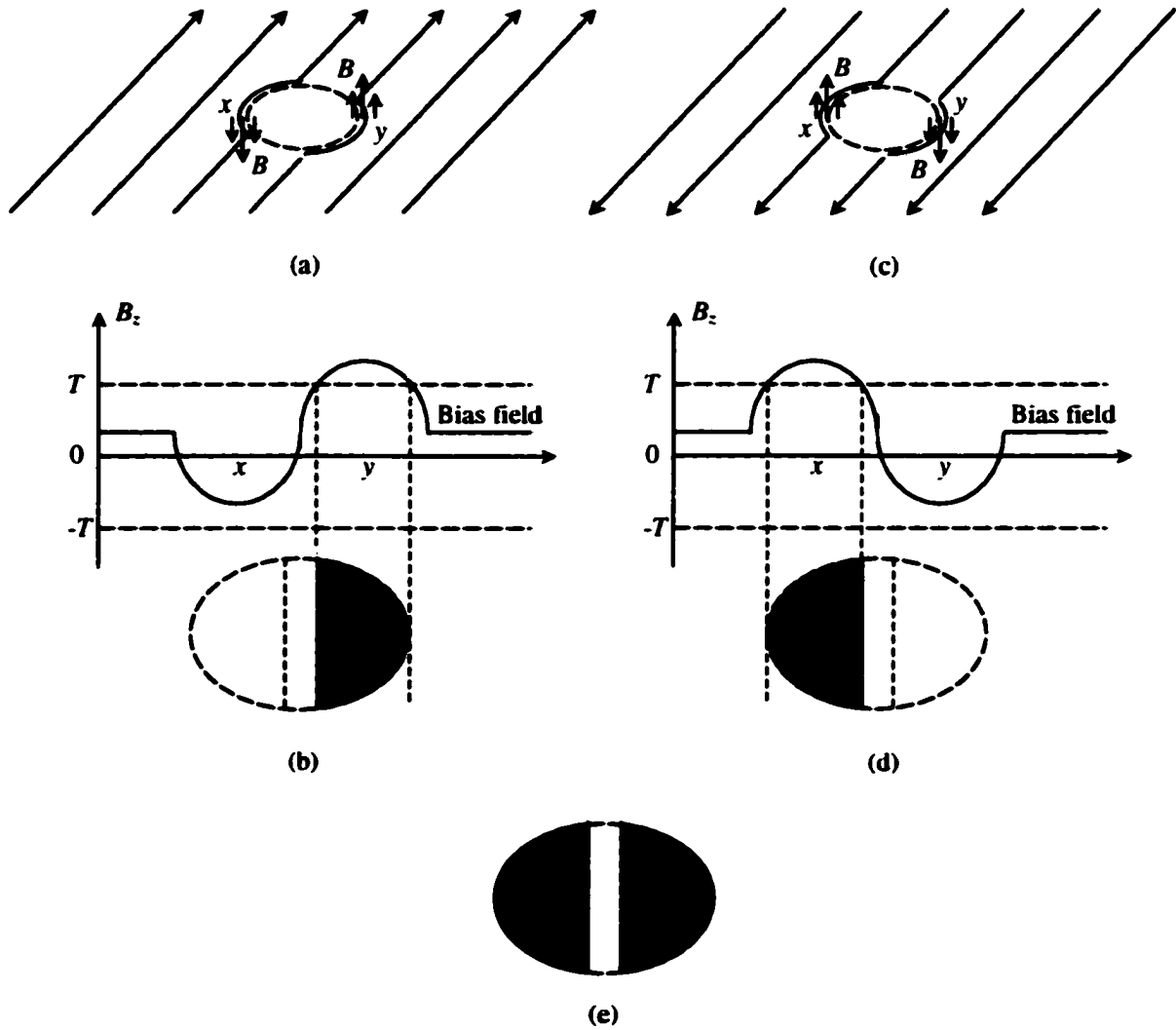


Figure 6.3 Induced currents, normal magnetic fields, and corresponding images
 (a) Induced currents and leakage fields in the first half cycle
 (b) Normal field densities and corresponding image in the first half cycle
 (c) Induced currents and leakage fields in the second half cycle
 (d) Normal field densities and corresponding image in the second half cycle
 (e) Image generated by the whole cycle

that both the above half images are visible to the inspector at the same time and appears like Figure 6.3 (e).

Generally the leakage field associated with a flaw is much smaller than the threshold value necessary to flip the domain in the garnet sensor film. A bias coil is utilized to generate a bias field that is just a little smaller than the threshold. Since the total magnetic field applied to the sensor is the sum of the leakage and bias fields, the use of bias coil allows the sensor to detect very small leakage fields.

In the actual procedure of MOI inspection, the sensor is first cleared of all previous images and appear uniformly bright by the delta-function type erase current pulse in the bias coil. Then a steady state current in the bias coil and the excitation sheet current in the foil are established at the same time. To detect cracks in different directions, multi-direction (rotating) excitation current is adopted. The image appear in the garnet film due to anomalies in the test specimen is observed by the inspector or recorded by a CCD TV camera for further analysis. If the magnetic fields are removed by turning off the sheet-current excitation, the films will retain most of the established magnetization (memory), the image produced remains until the start of the next erase pulse. Images are erased and refreshed about 26 times a second [159].

The advantages of MOI are presented in [158] and [160] and summarized below:

- (1) MOI inspection is faster than conventional NDE techniques in that it produces large area and real-time images of inspected parts;
- (2) MOI instrument is suitable for detecting both surface breaking and subsurface cracks:
At higher frequency, it can detect small, tight surface cracking; at lower frequency, it can detect subsurface cracking and corrosion in aluminum;

- (3) Interpreting binary MO images is much easier than interpreting complex impedance trajectory obtained by conventional eddy current methods, which reduces the training requirements;
- (4) It eliminates the need for paint and decal removal;
- (5) It can be used on conducting and ferromagnetic specimens as well as composites by “tagging” the specimens with ferromagnetic particles;
- (6) It dramatically reduces the possibility of false calls;
- (7) The MO images are easy to document with videotapes or cameras.

6.3 Finite Element Modeling

6.3.1 Formulations

Numerical modeling of NDE phenomenon is extremely useful in understanding the underlying field/flaw interaction and offers the capability to examine effects of individual test parameters that are expensive to obtain experimentally.

A 3-D finite element model of MOI phenomenon has been developed, in which the A - v formulation is utilized. The governing equations for time-varying harmonic fields can be derived as [161]

$$\nabla \times \frac{1}{\mu} \nabla \times A + j\omega\sigma A + \sigma \nabla v = 0 \quad \text{in } \Omega_1 \quad (6.1)$$

$$\nabla \cdot (j\omega\sigma A + \sigma \nabla v) = 0 \quad \text{in } \Omega_1 \quad (6.2)$$

$$\nabla \times \frac{1}{\mu} \nabla \times A = J, \quad \text{in } \Omega_2 \quad (6.3)$$

In (6.1) – (6.3), Ω_1 and Ω_2 are a partition of the solution domain with Ω_1 and Ω_2 denoting the eddy current region and surrounding free space respectively. A is the magnetic vector potential used in both Ω_1 and Ω_2 ; v is the electric scalar potential used in Ω_1 only; μ and σ are the permeability and conductivity of the media respectively.

Expanding the potentials in terms of shape functions and applying the Galerkin technique in (6.1) – (6.3), the modeling problem reduces to solving the following system of algebraic equations

$$GU = Q \quad (6.4)$$

where G is a symmetric and complex matrix, U is the unknowns consisting of the electric scalar potential and the three components of the magnetic vector potential at each node, Q is the load vector incorporating the current source.

Physical and measurable quantities, such as magnetic flux density B , Electric field intensity E and conduction current density J , are calculated using the following formulae

$$B = \nabla \times A \quad (6.5)$$

$$E = -\frac{\partial A}{\partial t} - \nabla v \quad (6.6)$$

$$J = \sigma E \quad (6.7)$$

B is calculated and thresholded to generate a binary MO image. J is calculated for the purpose of examining the current distribution in the test specimen.

The model has been validated by comparing the predicted image with the experimental image [162].

6.3.2 Simulation Results

The predicted binary MO images in the presence of radial crack, fastener-to-fastener crack, or circumferential crack are shown in this section along with the geometries and meshes.

6.3.2.1 Radial Crack

The geometry and mesh under consideration in this subsection is shown in Figure 6.4. The test sample is 90mm long, 90mm wide and 3mm thick. A rivet is embedded in the aluminum plates. The diameters at the top and bottom of the rivet are 6mm and 4mm respectively. The induction foil, whose size is $30 \times 30 \times 0.05 \text{mm}^3$, is located 0.35mm above the top surface of the specimen. The foil carries 1.5kHz or 3kHz linear (one directional) alternating current with the root mean square value of current density to be 10^8A/m^2 . The magnetic field is measured at 0.1mm above the foil. A buried crack in the lowest layer of the aluminum plates is considered as the critical flaw to be detected. The crack has a height of

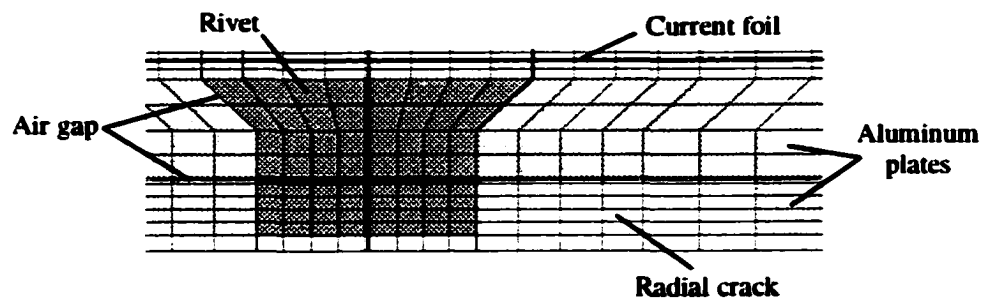


Figure 6.4 Geometry and mesh with radial crack

Table 6.1 Material properties

Material	Relative permeability	Conductivity (S/m)
Aluminum plates	1	1.9×10^7
Rivet	1	1.9×10^7
Induction foil	1	0

1mm, width of 0.1mm and length of 5mm. The material properties of the aluminum plates, rivet and induction foil are listed in Table 6.1

In practice, rotating excitation currents are used to detect flaws in all directions. For simplicity, in the FE simulations in this dissertation, we use linear currents in a direction perpendicular to the orientation of the crack.

The normal components of the predicted magnetic flux densities are shown in Figure 6.5. The binary MO images are obtained by thresholding the flux densities. Figures 6.6 (a) presents the predicted binary MO images obtained at a frequency of 3kHz, with the threshold selected to be 25% of peak value and Figure 6.6 (b) shows the corresponding image at frequency 1.5kHz, threshold 10% of peak value. Figure 6.6 (b) is not as clean as (a) due to the strong edge effect due to the finite size of the induction foil. Both the binary images skew in the direction of the radial crack. We will show later that the degree of the skewness reflects the strength of field/crack interaction. The parametric studies on the skewness of MO image will be discussed later.

6.3.2.2 Fastener-to-Fastener Crack

As shown in Figure 6.7, two rivets are embedded in a three-layer planar aluminum structure. The distance between the centers of the two rivets is 0.7 inch. A buried crack extends from one rivet to the other. The width and height of the crack, the sizes of the rivets, the locations of the foil and sensor, and the material properties are the same as those in Figure 6.4. All air gaps are 0.1mm wide.

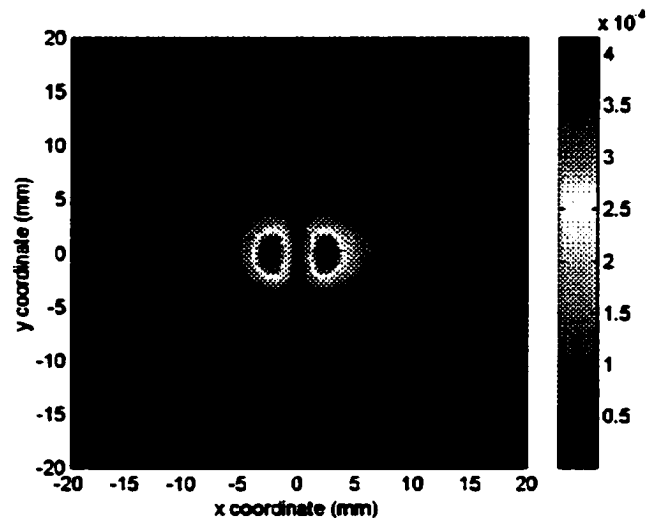


Figure 6.5 Predicted B_z with radial crack, crack length 5mm, frequency 3000Hz

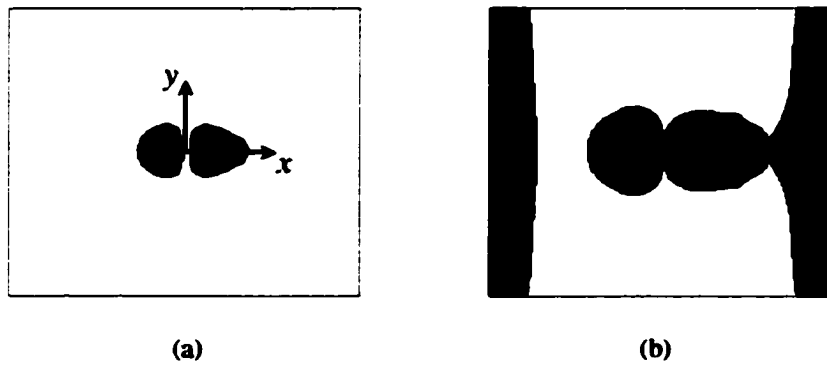


Figure 6.6 Predicted binary MO images with radial crack, crack length 5mm
 (a) Frequency 3000Hz, threshold 25% of peak value
 (b) Frequency 1500Hz, threshold 10% of peak value

Figure 6.8 shows the normal components of the predicted magnetic flux densities when the excitation current of frequency 3kHz is applied perpendicular to the crack. Figure 6.9 presents the corresponding binary MO image with a threshold selected to be 35% of peak value.

Figure 6.10 shows the normal components of the predicted magnetic flux densities when the 3kHz excitation current is parallel to the crack. Figure 6.11 presents the corresponding binary MO image with a threshold at 50% of peak value.

Obviously using an excitation current perpendicular to the crack makes it easy to detect it. On the contrary, the crack is not detectable when the excitation current is parallel to the crack. This again suggests using rotating excitation current to detect cracks in all directions.

6.3.2.3 Circumferential Crack

Figures 6.12 (a) and (b) are the side view and top view, respectively, of the geometry and mesh with circumferential crack. The sizes of the rivet, the locations of the foil and sensor, and the material properties are still the same as those in Figure 6.4. However, only one layer of aluminum plate with a thickness of 1mm is considered. The circumferential crack penetrating 100% of the plate thickness is 0.1mm wide and its circumferential extent is varied from 0 to 180 degrees in this subsection.

Figure 6.13 shows the normal components of the predicted magnetic flux densities assuming the excitation current in the y direction, operating frequency of 3kHz and 90° circumferential crack.

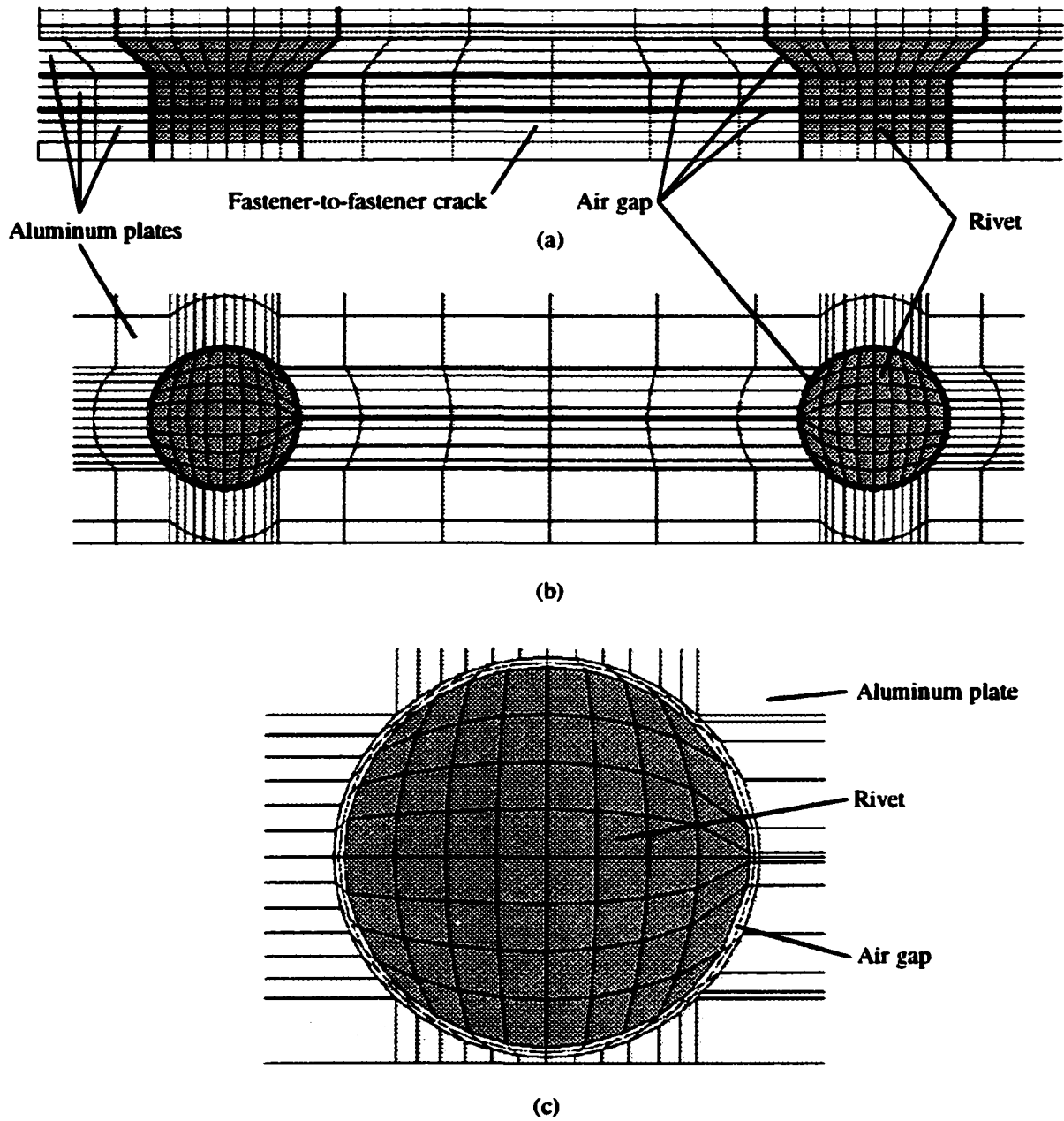


Figure 6.7 Geometry and mesh with fastener-to-fastener crack
(a) x-z plane (b) x-y plane (c) mesh around rivet

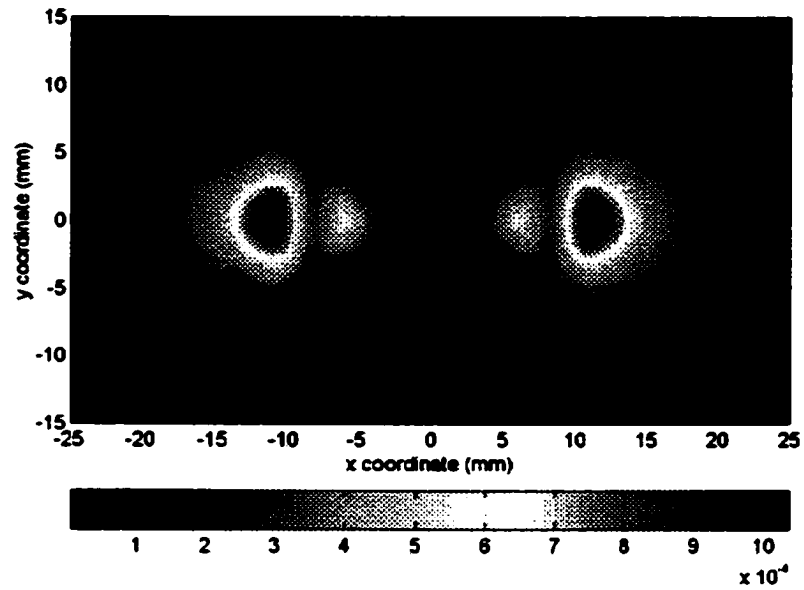


Figure 6.8 Predicted B_z with fastener-to-fastener crack.
current in y direction, frequency 3000Hz

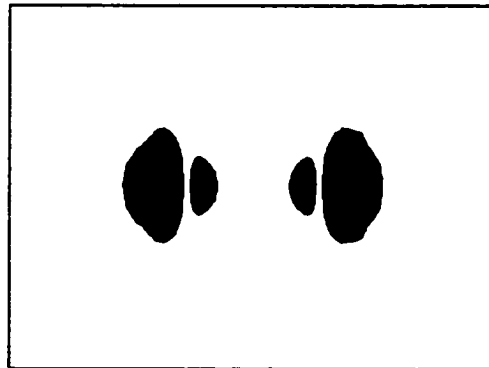


Figure 6.9 Predicted binary MO image,
current in y direction, frequency 3000Hz, threshold 35% of peak value

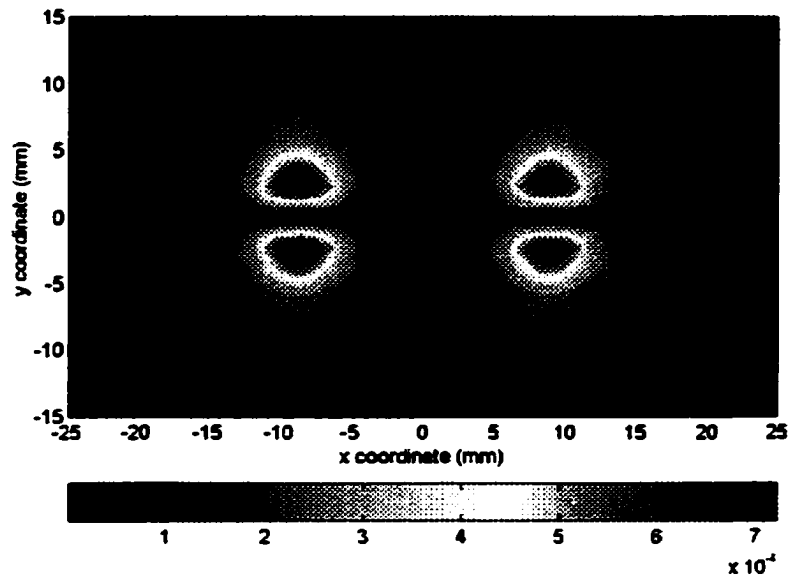


Figure 6.10 Predicted B_z with fastener-to-fastener crack.
current in x direction, frequency 3000Hz

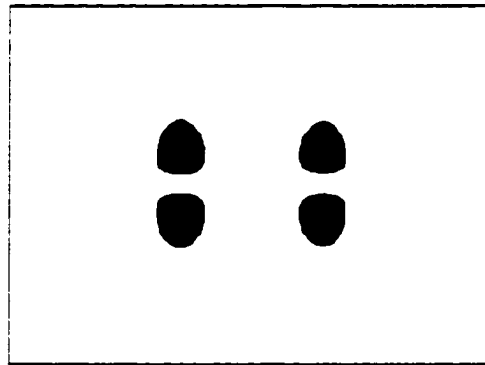


Figure 6.11 Predicted binary MO image.
current in x direction, frequency 3000Hz, threshold 50% of peak value

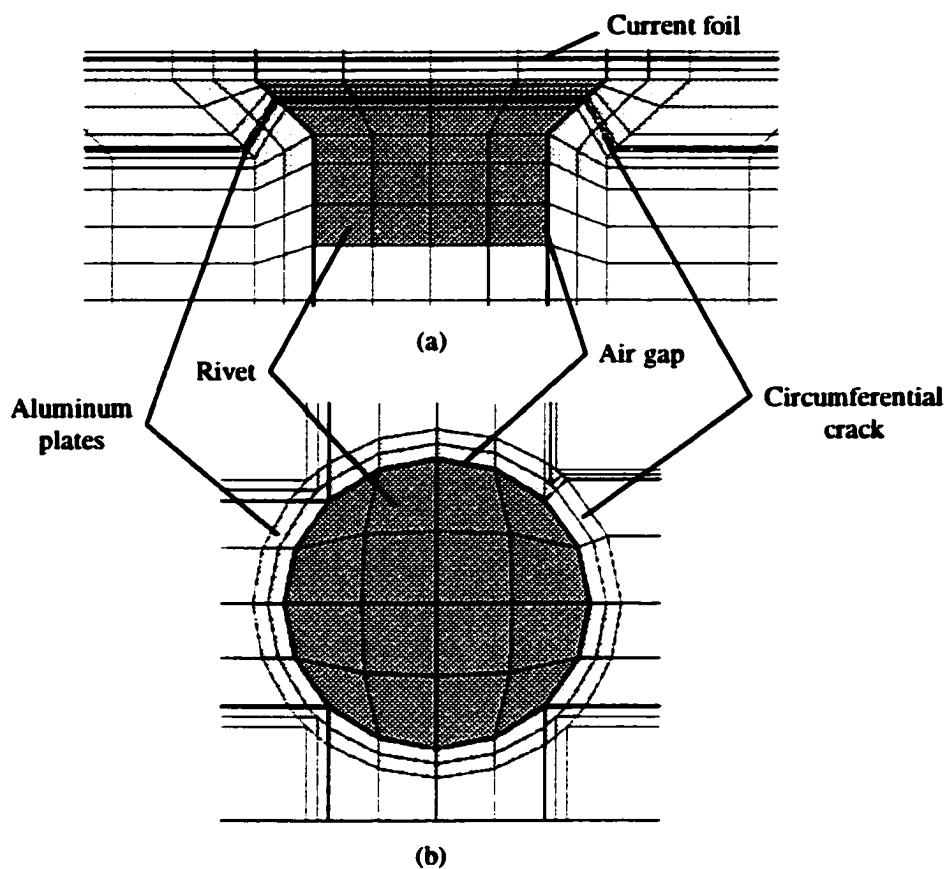


Figure 6.12 Geometry and mesh with circumferential crack
(a) x - z plane (b) x - y plane

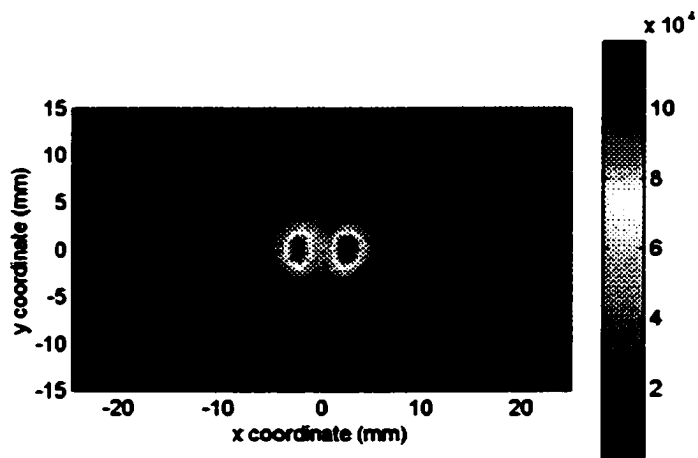
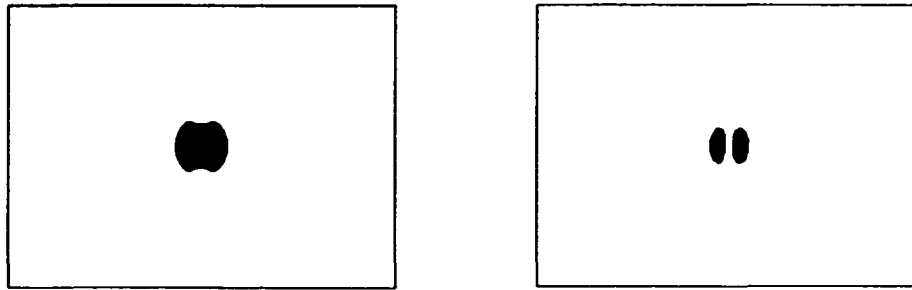


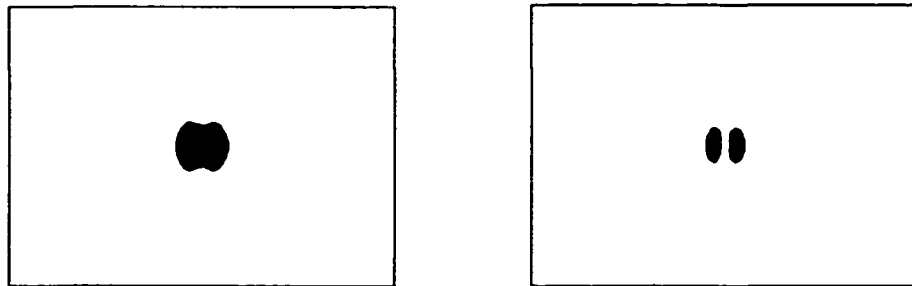
Figure 6.13 Predicted B_z with 90° circumferential crack, frequency 3000Hz



(a)

(b)

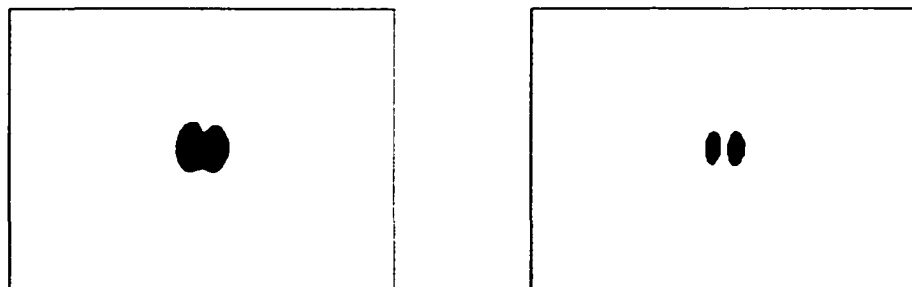
Figure 6.14 Predicted binary MO images without crack
(a) threshold 25% of peak value (b) threshold 50% of peak value



(a)

(b)

Figure 6.15 Predicted binary MO images with 45° circumferential crack
(a) threshold 25% of peak value (b) threshold 50% of peak value



(a)

(b)

Figure 6.16 Predicted binary MO images with 90° circumferential crack
(a) threshold 25% of peak value (b) threshold 50% of peak value

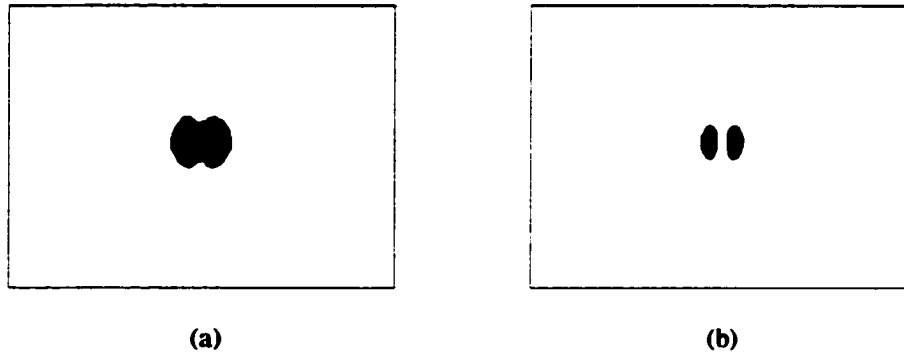


Figure 6.17 Predicted binary MO images with 180° circumferential crack
 (a) threshold 25% of peak value (b) threshold 50% of peak value

Predicted binary MO images with 0, 45, 90 and 180 degree circumferential cracks are shown in Figures 6.14 through 6.17. Figure 6.15 (a) is similar to is similar to Figure 6.14 (b) which implies that 45° circumferential crack is very difficult to detect. Images in Figures 6.16 (a) and (b) skew in both the x and y directions. Hence it can be concluded that the 90° circumferential crack is detectable. Figure 6.17 (a) looks similar to Figure 6.14 (a) and Figure 6.17 (b) looks similar to Figure 6.14 (b). However, they have small shifts in the y direction due to the crack. From this observation we can expect that if the position of the rivet center is known, 180° circumferential crack can be detected.

6.4 Coefficient of Skewness for MOI Applications

The standard statistical definition of the Coefficient of Skewness is

$$CS = \frac{\sum_{i=1}^N (x_i - \mu)^3}{\sigma^3} \quad (6.8)$$

where x_i ($i = 1, 2, \dots, N$) are the N data points (x coordinate of black pixel in Figure 6.6 (a)), μ the expectation and σ the standard deviation. However using the above definition, the

skewness of the MO images associated with the same crack may have different signs with different thresholds, because the expectation of the x coordinates of the black pixels is not at the origin and varies with variation in threshold. So the third moment (6.8) of data is not suitable for the definition of the skewness of an MO image.

Intuitively the skewness of an MO image should be measured with respect to the origin (rivet center). An alternative definition of the skewness of an MO image can be obtained as the negative ratio of the sum of the x coordinates of black pixels with positive x coordinates to the sum of the x coordinates of black pixels with negative x coordinates, i.e.,

$$CSO = \frac{S_1}{S_2} \quad (6.9)$$

where

$$S_1 = \sum_{i=1}^N \text{sgn}(x_i) \cdot x_i \quad (6.10)$$

$$S_2 = -\sum_{i=1}^N \text{sgn}(-x_i) \cdot x_i \quad (6.11)$$

$$\text{sgn}(x) = \begin{cases} 1, & x > 0 \\ 0, & \text{else} \end{cases} \quad (6.12)$$

With this definition, CSO is greater than 1 when the image skews in $+x$ direction and smaller than 1 when the image skews in $-x$ direction. CSO equals 1 when the image does not skew (i.e., no crack).

The above definition of skewness is further modified as

$$CS = \text{sign}(CSO - 1) \cdot (1 - \min(CSO, 1/CSO)) \quad (6.13)$$

where

$$\text{sign}(x) = \begin{cases} 1, & x > 0 \\ 0, & x = 0 \\ -1, & x < 0 \end{cases} \quad (6.14)$$

This modification ensures that $-1 < CS < 1$. CS is positive when the image skews in $+x$ direction, negative when the image skews in $-x$ direction, zero when the image does not skew.

It can be easily shown that the definition (6.13) is equivalent to the following formula

$$CS = \text{sign}(S_1 - S_2) \frac{\max(S_1, S_2) - \min(S_1, S_2)}{\max(S_1, S_2)} \quad (6.15)$$

with S_1 and S_2 given in (6.10) and (6.11) respectively.

If the signal image is corrupted due to the strong edge effect of the finite size of induction foil, the skewness is not meaningful. So in the following parametric studies, we consider the skewness of MO images that are not corrupted by edge effects.

6.5 Parametric Studies on the Performance of MOI

Parametric studies are performed to observe the effects of crack size, tear strap and excitation frequency on the skewness of binary MO image. The geometry under consideration in the rest of this chapter is that of the radial crack as shown in Figure 6.4.

6.5.1 Effect of Crack Size on Skewness

Figure 6.18 shows the effect of crack size on skewness of binary MO image at an excitation frequency of 3kHz. The skewness value is plotted as a function of the threshold. Obviously, the larger the crack, the greater is the skewness resulting in easier detection. Another phenomenon observed from Figure 6.18 is that the optimum threshold, at which the

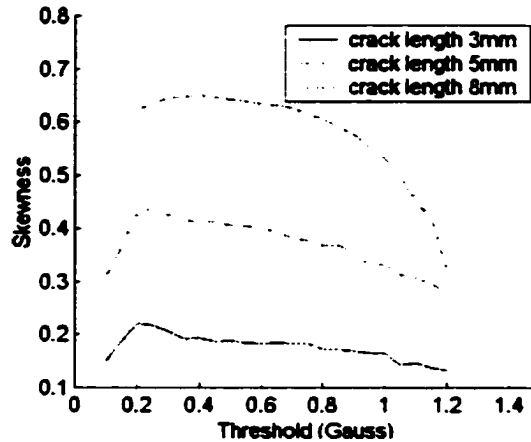


Figure 6.18 Effect of crack size and threshold on skewness, frequency 3000Hz

skewness reaches its maximum, increases with increase in crack size. The optimum thresholds for crack length 3mm, 5mm and 8mm when the excitation frequency is 3kHz are 0.2 Gauss, 0.25 Gauss and 0.4 Gauss respectively. These conclusions are also true for other excitation frequencies.

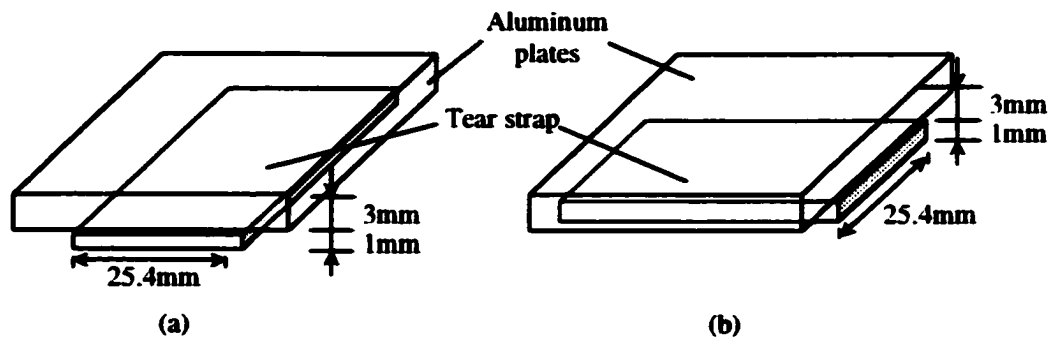


Figure 6.19 Tear straps under aluminum plates
 (a) Tear strap in y direction (perpendicular to the crack orientation)
 (b) Tear strap in x direction (parallel to the crack orientation)

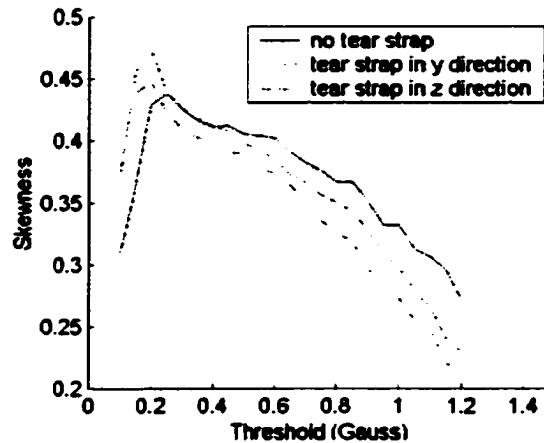


Figure 6.20 Effect of tear strap and threshold on skewness, crack length 5mm, frequency 3000Hz

6.5.2 Effect of Tear Strap on Skewness

A tear strap is added below the fastener and aluminum plate, as shown in Figures 6.19 (a) and (b). Figure 6.20 shows the effect of tear strap on the skewness of binary MO image due to the crack of length 5mm and the excitation frequency 3kHz. It is easy to see that skewness of MO image with tear strap located along the y direction (perpendicular to the crack orientation) is greater than with tear strap located along the x direction (parallel to the crack orientation). Another fact implied by Figure 6.20 is that the optimum threshold in the presence of tear strap is smaller than that in the absence of tear strap and the optimum threshold in the presence of tear strap is independent of the orientation of the tear strap. These conclusions hold for other excitation frequencies.

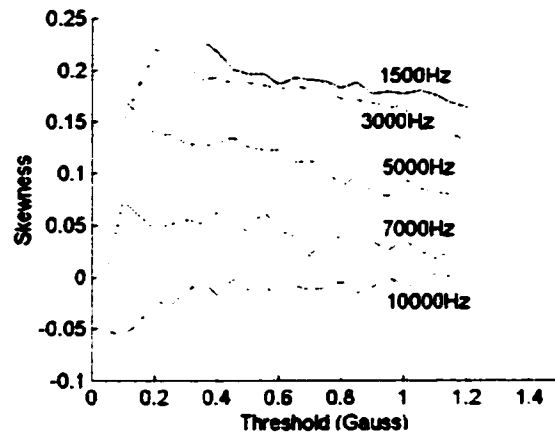
6.5.3 Effect of Frequency on Skewness

Figures 6.21 (a) ~ (c) show the effect of frequency on skewness of thresholded MO images when the crack lengths are 3, 5 and 8 mm respectively. From these results we can make the following observations:

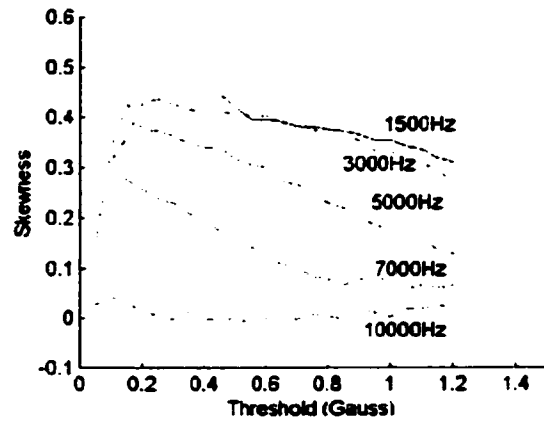
- (1) Skewness of a binary MO image decreases with increase in frequency.
- (2) Generally (disregarding edge effect), the skewness of a binary MO image increases with increasing threshold value until it reaches an optimum, when defect contribution is maximum. Further increase in the threshold value results in a reduction in the skewness value indicating that the defect contribution is now lower. This trend is, however reversed when the excitation frequency is higher than 7kHz for a crack of length 3mm (see Figure 6.21 (a)). Similar effect is observed to take place at a frequency of 10kHz for a crack of length 5 mm (see Figure 6.21 (b)).

(3) We can define Critical Frequency as the frequency at which the skewness versus threshold behavior goes through a transition as described above. We can then find that the critical frequency is higher for larger crack size: the critical frequency is between 5kHz and 7kHz for 3mm-long crack (see Figure 6.21 (a)), between 7kHz and 10kHz for 5mm-long crack (see Figure 6.21 (b)), and higher than 10kHz for 8mm-long crack (see Figure 6.21 (c)).

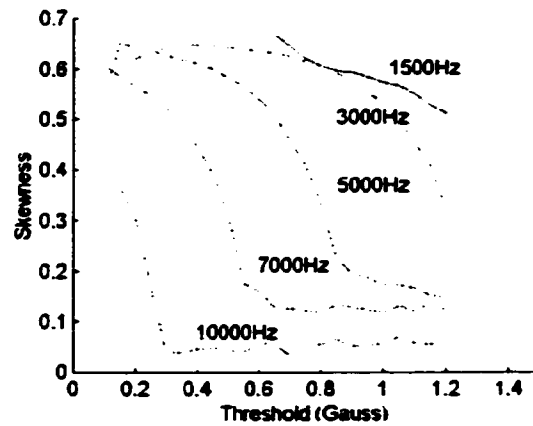
(4) The optimum threshold of the magnetic flux density generating the MO image decreases with increase in frequency. For example, when the crack length is 5mm, the optimum thresholds for images obtained at excitation frequencies 3kHz, 5kHz and 7kHz are 0.25 Gauss, 0.15 Gauss and 0.1 Gauss respectively.



(a)



(b)



(c)

Figure 6.21 Effect of frequency and threshold on skewness
 (a) crack length 3mm (b) crack length 5mm (c) crack length 8mm

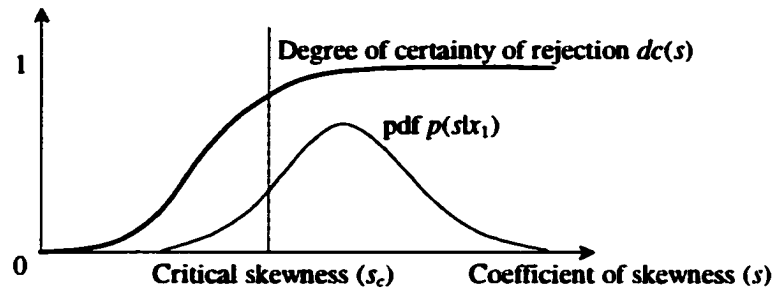


Figure 6.22 pdf of crack signal and degree of certainty of rejection

6.6 Application of POD Model

A typical distribution of the coefficients of skewness (CS) of binary MO images is shown in Figure 6.22. The traditional formula for calculating POD for a critical flaw is given in Chapter 4 and rewritten below for convenience:

$$POD = \int_{s_c}^{\infty} p(s | x_1) ds \quad (6.16)$$

where $p(s | x_1)$ denotes the conditional pdf of coefficient of skewness (s) in the presence of a crack; s_c is the selected threshold. To avoid confusion with thresholds, s_c is called critical skewness rather than threshold. Changing the mean value of input (perturbation) pdf and calculating the corresponding POD using (6.16), a curve that indicates the relationship between POD and level of the uncertainty can be obtained.

Equation (6.16) is, however, not suitable for MOI applications, because it is not reasonable to totally accept or reject a specimen whose associated coefficient of skewness is only slightly greater or smaller than the critical skewness, which may be caused by when the inspector becomes fatigue. The modification of the model for MOI applications is presented in the follow subsection.

6.6.1 POD Calculation for MOI Applications

Unlike automated inspection techniques, MOI is based on operator interpretation of images. The inspector makes an accept/reject decision by observing the binary MO image. The possibility of correct judgment is highly dependent on the experience (e.g. training) and physical status (e.g. fatigue) of the inspector, as well as the working environment. So it is very difficult to develop a theoretical model for estimating the POD associated with an image-based technique.

Observing Figures 6.23 (a) ~ (c), it is easy to find that the specimen associated with (a) whose CS is 0.321 has a crack. The specimen associated with (b) whose CS is 0.201 also has a crack. However, the confidence level of the claim (b) is not as high as that of claim (a). The confidence level, or degree of certainty, of rejection becomes smaller when the image has a lower coefficient of skewness, such as in (c). It is unlikely to accept a specimen, whose CS is greater than that of (a). It is also difficult to reject a specimen, whose CS is smaller than that of (c). If we use 0.321 as the critical skewness, the fact that CS of (c) is about half of that of

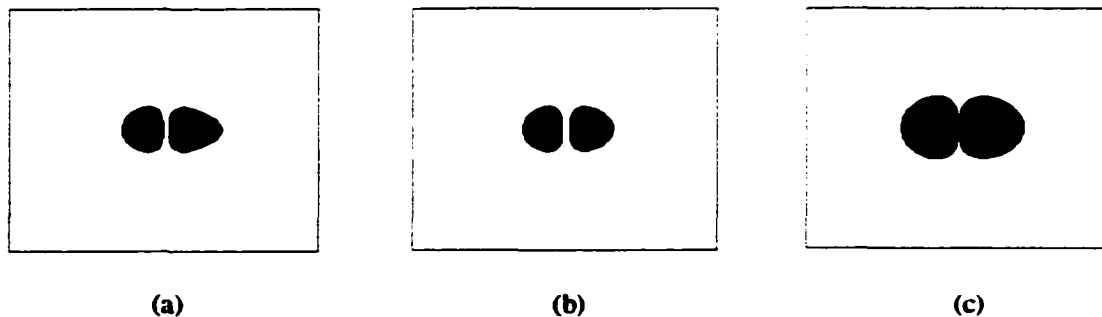


Figure 6.23 Predicted binary MO images with radial crack
 (a) crack length 5mm, threshold 25% of peak value, coefficient of skewness is 0.321
 (b) crack length 3mm, threshold 10% of peak value, coefficient of skewness is 0.201
 (c) crack length 3mm, threshold 25% of peak value, coefficient of skewness is 0.154

(a) suggests that the model describing the relationship between the degree of certainty of acceptance vs. CS must have the following properties: it decreases monotonically; it is close to 1 when CS is less than half of the critical skewness and close to 0 when CS is greater than the critical skewness.

The best model satisfying the above requirements is the Butterworth low-pass filter response. A simpler alternative model is the pdf of Gaussian distribution normalized by its maximum value. Its standard deviation is half of the critical skewness. So the degree of certainty of rejection is modeled as

$$dc(s) = 1 - \sqrt{2\pi} \phi\left(\frac{s}{\sqrt{s_c/2}}\right) \quad (6.17)$$

where $\phi(\cdot)$ is the pdf of the standard Gaussian distribution and s_c is called the critical skewness. The model is shown in Figure 6.22.

Having the degree of certainty of rejection, the formula for calculating POD (6.16) can be modified by weighting the pdf with degree of certainty of rejection and integrating over the whole range of coefficients of skewness, i.e.,

$$POD = \int_0^{+\infty} dc(s)p(s|x_1)ds \quad (6.18)$$

In the following POD studies in this section, the critical crack in Figure 6.4 has height 1mm, width 0.1mm and length 5mm.

6.6.2 POD with respect to Threshold

In calculating the POD at a particular threshold, the variations of threshold is assumed to be Gaussian with its mean being the given threshold and variance 5% of the mean. The pdf of

the thresholds is easily estimated as described earlier. The pdf of the corresponding coefficients of skewness are computed by mapping the thresholds to the parametric relation curve of CS vs. threshold. The mapping process is simply an interpolation in this instance. An example of the relation curve used in this report with excitation frequency 3kHz is shown in Figure 6.24 (a). Having the pdf of the coefficients of skewness, the POD is then calculated using (6.18) with the critical skewness 0.321. Repeating the above procedure for different mean values of threshold, the POD curve with respect to threshold is obtained and shown in Figure 6.24 (b).

Observing Figures 6.24 (a) and (b) carefully, it is not difficult to find that, the optimum threshold for POD is not identical to that for skewness. The coefficient of skewness reaches its maximum at threshold 0.24 Gauss, while the maximum POD appears at threshold 0.35 Gauss. This is due to the fact that little variation of threshold to the left dramatically reduces the skewness if the mean threshold is the location of maximum CS.

Another example of POD study with respect to threshold is conducted by increasing the excitation frequency to 6kHz. The relation between skewness and threshold and the curve of POD vs. threshold are shown in Figures 6.25 (a) and (b) respectively. In this case, the optimum thresholds for skewness and POD are 0.11 Gauss and 0.15 Gauss respectively.

6.6.3 POD with respect to Current Frequency

Figure 6.26 (a) shows the CS data used in this case study. Two examples are conducted with the threshold being set to 0.5 Gauss and 0.09 Gauss individually. The procedure of obtaining POD curves with respect to frequency is similar to that used for obtaining POD curves with respect to threshold as described in the above subsection.

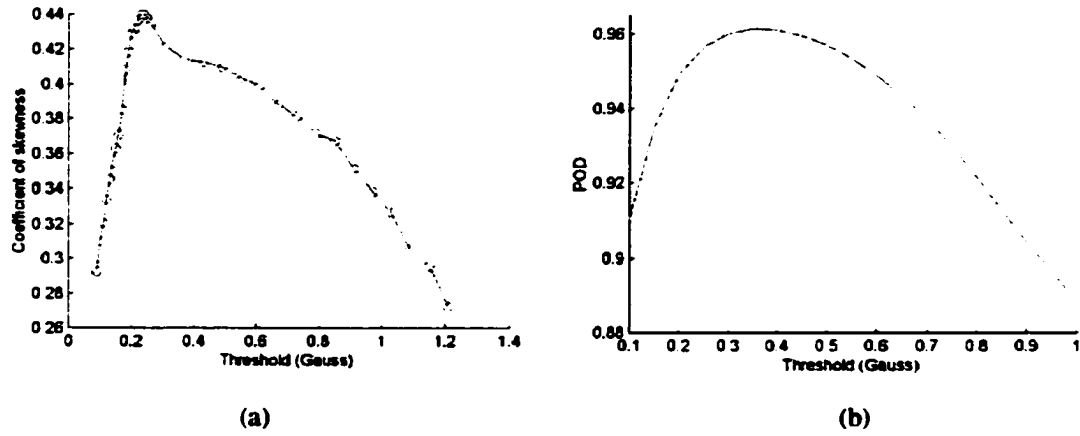


Figure 6.24 Skewness and POD vs. threshold, frequency 3000Hz
 (a) Coefficient of skewness vs. threshold (b) POD vs. threshold

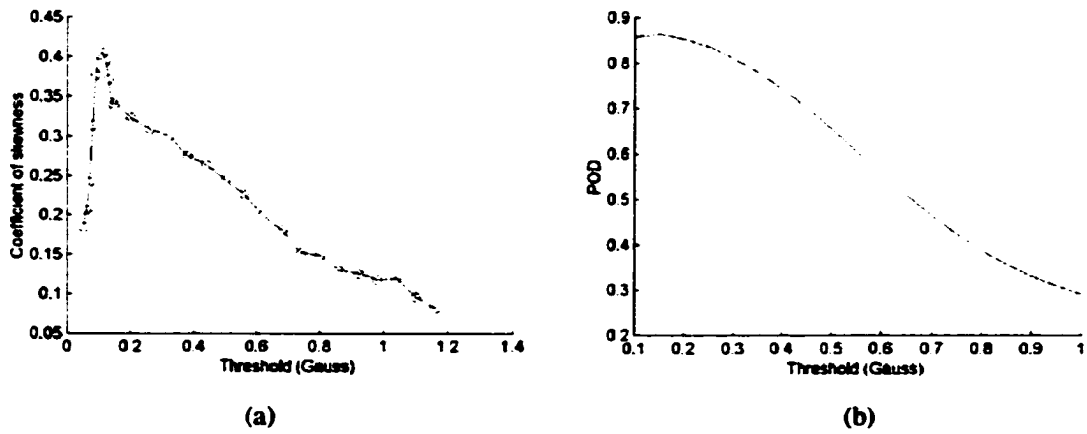
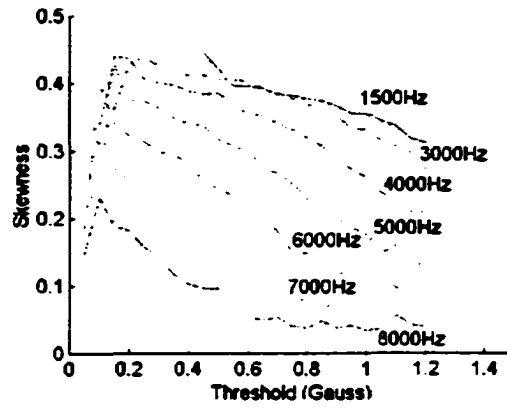


Figure 6.25 Skewness and POD vs. threshold, frequency 6000Hz
 (a) Coefficient of skewness vs. threshold (b) POD vs. threshold

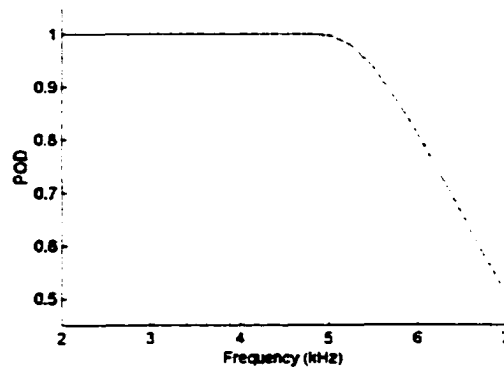
The POD curve versus frequency with 0.5 Gauss threshold is shown in Figure 6.26 (b). The POD is 1 if the frequency is lower than 5kHz. If the frequency is higher than 5kHz, increasing the frequency results in decreasing the POD. This is not necessarily true for all thresholds, especially when the threshold is smaller than 0.2 Gauss, where the CS curves overlap as seen in Figure 6.26 (a). The POD curve when setting threshold to 0.09Gauss is shown in Figure 6.26 (c).

6.7 Application of Taguchi Methods

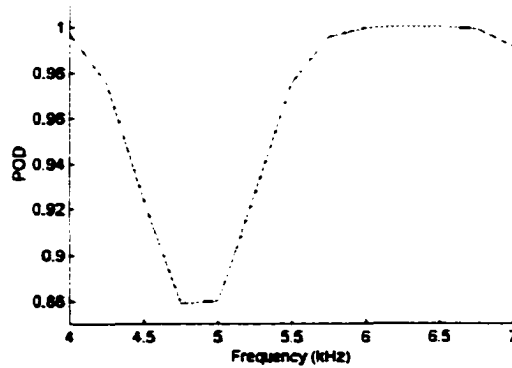
Many test parameters affect the skewness of binary MO image and hence the probability of detection. Parametric studies on the performance of MOI system and POD studies have been presented in the above sections. The parametric studies seek the optimum value of a particular test parameter while keeping other parameters fixed. The Taguchi method, on the other hand, changes parameter values simultaneously to look for the optimum set of test parameters. Ideally, one would like to have maximum skewness. In the meanwhile, the performance of MOI is expected to be most robust to the variations of the parameters. Sometimes the resultant sets of parameters are contradictory. In this section, the Taguchi method is applied to find a tradeoff by means of signal to noise ratio analysis. The number of trials necessary for the optimization is significantly reduced with Taguchi's methodology of experimental design.



(a)



(b)



(c)

Figure 6.26 Coefficients of skewness for multiple frequencies and POD vs. frequency
(a) Coefficients of skewness vs. threshold with multiple frequencies
(b) POD vs. frequency, with threshold 0.5 Gauss
(c) POD vs. frequency, with threshold 0.09 Gauss

6.7.1 Experiment Design and Simulation

The performance characteristic in this study is chosen to be the coefficient of skewness (CS) of the binary MO image. The larger the coefficient of skewness associated with a critical flaw the better the performance of the MOI system.

Four test parameters are believed to apparently affect the skewness of MO image. They are, namely, excitation current value, excitation current frequency, threshold and liftoff. Since increasing current value is equivalent to reducing liftoff, we do not consider the effect of liftoff in this dissertation. These parameters are controllable factors and incorporated in the inner array. Their variations are noise factors and incorporated in the outer array. The Taguchi method is utilized to choose the optimum set of parameters that yield an MO image with maximum coefficient of skewness and are less sensitive to their variations. The factors and the levels of each factor considered in this dissertation are listed in Table 6.2.

The standard OA $L_9(3^4)$, as shown in Table 6.3, is used for the experiment layouts of both the inner and outer arrays. Factors A, B and C are assigned to the first three columns in the inner array. Their variations, i.e., Factors D, E and F, are assigned to the first three columns in the outer array. The last columns of both the inner and outer arrays are left empty.

For each combination of the simulation conditions in both the inner and outer arrays, the 3-D finite element model using $A-v$ formulation is performed. For each row of the inner array, all trials in the outer array are performed. The resultant coefficients of skewness are then used in calculating statistical quantities, such as mean response, standard deviation and signal to noise ratio, as shown in Table 6.4. The total number of trials using the Taguchi method is 81 (9^2). This demonstrates the efficiency of the Taguchi's experimental design

Table 6.2 Factors and levels

Factors		Levels			
		Level 1	Level 2	Level 3	Unit
Controllable	Current value (A)	120	240	360	Amp
	Excitation frequency (B)	3000	4000	5000	Hz
	Threshold (C)	0.2	0.4	0.6	Gauss
Uncontrollable	Variation of A (D)	-24	0	+24	Amp
	Variation of B (E)	-40	0	+40	Hz
	Variation of C (F)	-0.04	0	+0.04	Gauss

Table 6.3 Orthogonal array $L_9(3^4)$

Trial \ Column	$L_9(3^4)$			
	1	2	3	4
1	1	1	1	1
2	1	2	2	2
3	1	3	3	3
4	2	1	2	3
5	2	2	3	1
6	2	3	1	2
7	3	1	3	2
8	3	2	1	3
9	3	3	2	1

Table 6.4. Summary of simulation results

Trial	μ	σ	$(S/N)_1$	$(S/N)_2$
1	0.4168	0.0088	33.4877	4.6829
2	0.3088	0.0405	17.6460	3.1948
3	0.1417	0.0336	12.5056	1.3213
4	0.4164	0.0031	42.5668	4.6771
5	0.3589	0.0148	27.6783	3.8597
6	0.3852	0.0204	25.5288	4.2212
7	0.4153	0.0026	44.1593	4.6611
8	0.3923	0.0542	17.1984	4.2955
9	0.3692	0.0061	35.6870	4.0017

μ : Mean Response

σ : Standard Deviation

$$(S/N)_1 = 10 \log_{10} (\mu^2 / \sigma^2)$$

$$(S/N)_2 = -10 \log_{10} (MSD)$$

when compared with the full factorial design where the total number of trials required is 729 (27^2).

6.7.2 Analysis of Main Effects

There are two definitions of signal to noise ratio (S/N) that are commonly used. One is

$$(S/N)_1 = 10 \log_{10} \left(\frac{\mu^2}{\sigma^2} \right) \quad (6.19)$$

and the other one is

$$(S/N)_2 = -10 \log_{10} (MSD) \quad (6.20)$$

with

$$\begin{aligned} MSD &= \frac{1}{n} \sum_{i=1}^n (y_i - t)^2 \\ &= (\mu - t)^2 + \sigma^2 \end{aligned} \quad (6.21)$$

where MSD stands for the mean square deviation from the target value. In equations (6.19) – (6.21), μ is the mean response, σ is the standard deviation, y_i is the i th result in the outer array, n is the number of simulation conditions in the outer array, and t is the target value (1 for the absolute value of the coefficient of skewness).

To make the performance of MOI system robust to the variations of parameters, Definition (6.19) is preferred. Among the nine combinations of test parameters, the 7th set has the highest robustness. Definition (6.20) measures the deviation of quality characteristic from the target, which is consistent with Taguchi's quadratic loss function and is utilized in further analysis in this dissertation.

The main effects indicate the general trend of the influence of these factors. They are calculated by averaging the S/N ratios for each control factor at the same level. Main effects calculated from Table 6.4 are listed in Table 6.5 and plotted in Figure 6.27.

Generally the optimal set of parameters may not appear in those trial conditions in the orthogonal array, because Taguchi's experimental design is a partial factorial design. Optimal condition is found as the combination of the best level of each factor. Observing Figure 6.27, the optimal condition is Levels 3, 1 and 1 for Factors A, B and C respectively, which is not included in Table 6.4. A confirmation run is performed with the condition $A_3B_1C_1$ and the resultant signal to noise ratio is 3.7115, much less than many of the S/N ratios in Table 6.4. The controversy occurs because we have neglected all the interactions between test parameters.

Two factors are said to interact when the effect of changes in one of them determines the influence of the other one and vice versa [124]. Analyses find that the interaction between current value and threshold, denoted as $A \times C$, cannot be neglected, as represented graphically in Figure 6.28. The combination A_3C_1 should be replaced by the other combination that yields the maximum S/N ratio. Since A_1C_1 , A_2C_2 and A_3C_3 have almost the same S/N ratios, the optimal set of test parameters are $A_1B_1C_1$, $A_2B_1C_2$ and $A_3B_1C_3$, i.e., frequency at Level 1 (3kHz), current value and threshold at the same level (linearly proportional). Further studies reveal the fact that using threshold proportional to the current value will yield almost identical binary MO images. Since the optimal combination appears in Table 6.4, no additional runs are required.

Table 6.5 Main effects

Factors	Level 1	Level 2	Level 3
Factor A	3.066	4.253	4.319
Factor B	4.674	3.783	3.181
Factor C	4.400	3.958	3.281

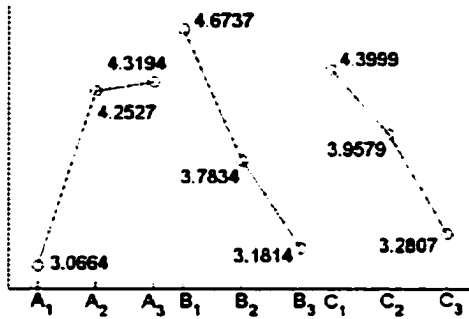


Figure 6.27 Main effects

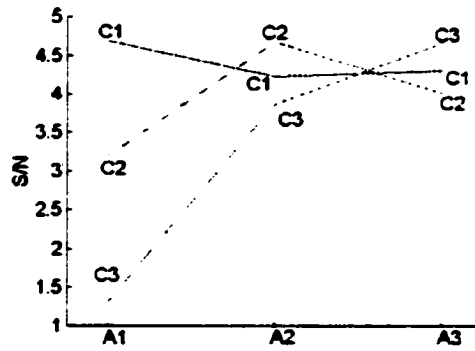


Figure 6.28 Interaction AxC

6.7.3 Analysis of Variance

Interaction A×C is assigned to the last column of the inner array. Analysis of variance is performed to estimate the percent contribution of each factor, which is helpful in determining which of the factors need to be controlled and which do not.

In the left part of Table 6.6, the degree of freedom of the error term (f_e) is negative, which is not meaningful. In order to calculate other statistical measurements involving the division by f_e , the factor that has small variance (Interaction A×C in this case) is pooled to obtain new, positive estimate of S_e (sum of squares of the error term) and f_e . The percent contributions for the factors are listed in the last column of Table 6.6. Among the three test parameters considered, frequency has most influence on the performance on the MOI system in detecting the buried crack as shown in Figure 6.4. Other factors or errors, such as interactions between parameters, have a combined contribution of 41%.

6.7.4 Response-Model Approach

Disadvantages of the above loss-model approach have been presented in Section 4.3.4. To overcome the shortcomings, the response-model approach and the corresponding

Table 6.6 ANOVA table

Factor	Before pooling			After pooling				
	f	S	V	f	S	V	F	P (%)
A	2	2.982	1.491	2	2.982	1.491	3.171	22.166
B	2	3.382	1.691	2	3.382	1.691	3.597	26.510
C	2	1.906	0.953	2	1.906	0.953	2.028	10.490
A×C	4	0.940	0.235	(4)	Pooled	Pooled		
error	-2	0.000		2	0.940	0.470		40.834
Total	8	9.211		8	9.211			100.00

f: degrees of freedom S: sum of squares V: variance
F: variance ratio P: Percent contribution

combined-array design have been proposed, which are also discussed in the same section. In this section, we do not attempt to totally discard the loss-model approach. Instead, the response-model approach is utilized as a complement to the loss-model approach, with its own benefits discussed in Section 4.3.4.

In this scenario, a $L_{18}(2^1 \times 3^7)$ orthogonal array is chosen in designing the experiment with combined array, as shown in Table 6.7. The L_{18} OA has 8 columns: the first column is reserved for a 2-level factor; the others are for 3-level factors. Since we have totally 6 factors (see Table 6.2), the last column as well as the first column is not used. Hence the control factors A, B and C and the noise factors D, E and F are assigned to Columns 2, 3, 4, 5, 6 and 7 respectively. Using the combined array, only 18 runs are necessary in building the response

Table 6.7 Orthogonal array $L_{18}(2^1 \times 3^7)$

Column Trial	$L_{18}(2^1 \times 3^7)$								Skewness
	1	2	3	4	5	6	7	8	
1	1	1	1	1	1	1	1	1	0.4136
2	1	1	2	2	2	2	2	2	0.3190
3	1	1	3	3	3	3	3	3	0.1557
4	1	2	1	1	2	2	3	3	0.4410
5	1	2	2	2	3	3	1	1	0.3977
6	1	2	3	3	1	1	2	2	0.2783
7	1	3	1	2	1	3	2	3	0.4248
8	1	3	2	3	2	1	3	1	0.3924
9	1	3	3	1	3	2	1	2	0.3427
10	2	1	1	3	3	2	2	1	0.3318
11	2	1	2	1	1	3	3	2	0.3542
12	2	1	3	2	2	1	1	3	0.2713
13	2	2	1	2	3	1	3	2	0.4136
14	2	2	2	3	1	2	1	3	0.3573
15	2	2	3	1	2	3	2	1	0.3730
16	2	3	1	3	2	3	1	2	0.4114
17	2	3	2	1	3	1	2	3	0.3443
18	2	3	3	2	1	2	3	1	0.3605

model. Compared with the 81 runs with the product array. This shows the immediate advantage of the combined array approach in designing the experiment.

Before modeling the response, an experiment matrix X is built: every line in X describes an experiment while every column is related to effect or interaction. The entries of the experiment matrix are defined as the centered reduced values of factors for each trial, i.e.,

$$\bar{x} = \frac{2}{x_{\max} - x_{\min}} \left(x - \frac{x_{\max} + x_{\min}}{2} \right) \quad (6.22)$$

where x_{\max} and x_{\min} are the maximum and minimum values of a factor and \bar{x} is the centered reduced value. Equation (6.22) makes each entry of the experiment matrix to be in the interval $[-1, 1]$. Since the values chosen for each factor are equally spaced (Table 6.2), the \bar{x} values in X are -1 , 0 or $+1$, which denotes low level, median level or high level respectively.

Since the quadratic effects and the interactions between noise factors are generally of less concern in quality improvements, these terms are discarded in the model. Thus we can estimate the most important effects of factors and interactions using a relatively small number of simulations. Furthermore, the interaction between the controllable factors A (current value) and B (frequency) is believed to be small (this can be simply verified by plotting Interaction A×B). Hence there are totally 17 effects of factors and interactions to be estimated, which leads to 18 unknown coefficients in the model. The model is expressed as

$$\begin{aligned} y = & a_0 + a_1 x_A + a_2 x_B + a_3 x_C + a_4 x_D + a_5 x_E + a_6 x_F + a_7 x_A x_C + a_8 x_B x_C + a_9 x_A x_D + a_{10} x_A x_E \\ & + a_{11} x_A x_F + a_{12} x_B x_D + a_{13} x_B x_E + a_{14} x_B x_F + a_{15} x_C x_D + a_{16} x_C x_E + a_{17} x_C x_F \end{aligned} \quad (6.23)$$

in which x_i ($i = A, B, C, D, E, F$) are the centered reduced values of Factor i ; $x_i x_j$ ($i, j = A, B, C, D, E, F$) are the values of the interactions between Factors i and j ; y is the response

(coefficient of skewness in this scenario). Utilizing the method of least squares and the data in Table 6.7 to fit the model, the coefficients in (6.23) are calculated by

$$\hat{a} = (X^T X)^{-1} X^T y \quad (6.24)$$

So the fitted model is

$$\begin{aligned} y = & 0.355 + 0.042x_A - 0.054x_B - 0.143x_C - 0.013x_D - 0.087x_E - 0.145x_F \\ & + 0.148x_Ax_C + 0.006x_Bx_C - 0.239x_Ax_D - 0.127x_Ax_E - 0.097x_Ax_F - 0.034x_Bx_D \\ & + 0.022x_Bx_E - 0.030x_Bx_F - 0.001x_Cx_D - 0.003x_Cx_E + 0.014x_Cx_F \end{aligned} \quad (6.25)$$

Obviously the interaction A×D greatly influences the response. Interaction A×D is shown in Figure 6.29. Note that Factor A is a control factor while Factor D is a noise factor. To make the inspection system more robust relative to noise factor, the 3rd level of Factor A is preferred. This important information is missed when using the loss-model approach and the product-array design.

Recall that we have found in Section 6.7.2 that Interaction A×C also has a significant influence on the system response, which is also seen from the corresponding coefficient in the fitted model (6.25). Section 6.7.2 suggests that to reach best performance, Factors A and

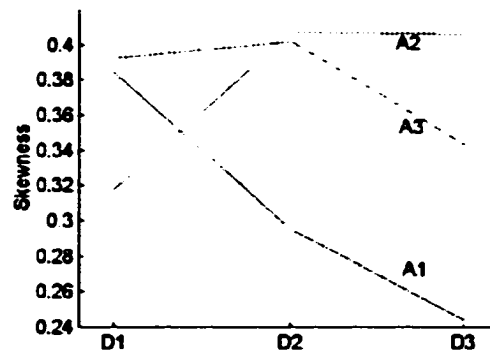


Figure 6.29 Interaction A×D

C should have the same levels. Combing this information with that obtained from Interaction **A**×**D**, we conclude that both Factors **A** and **C** should use the 3rd level for achieving robustness. So the optimal set of test parameters is $A_3B_1C_3$, i.e., current value at Level 3 (360Amp), frequency at Level 1 (3kHz), and threshold at Level 3 (0.6Gauss).

Equation (6.25) also implies that many control-factor-by-noise-factor interactions, such as the interaction between Factors **C** and **D**, are very small. The corresponding degree of freedom can be used in estimating other effects that are of interest.

CHAPTER 7 CONCLUSIONS AND FUTURE WORK

A Probability of detection (POD) model based on numerical modeling has been successfully employed to evaluate the performance of electromagnetic non-destructive inspection systems. The optimum value of a design parameter of the inspection tool can be obtained via the POD studies. The Taguchi method, on the other hand, optimizes the design parameters simultaneously. The use of Taguchi method is particularly useful for reducing the number of numerical simulations required for the optimization. The significance of the influence of each of the experimental factors on the inspection performance has also been determined by the Taguchi method.

7.1 Summary of Accomplishments

The tasks that have been accomplished to-date include:

- (1) Finite element modeling of MFL phenomenon of natural gas transmission pipeline inspection;
- (2) Development of model-based POD evaluation technique for automated NDE systems;
- (3) POD studies with respect to individual parameters such as radial liftoff, magnetization level, and circumferential shift in natural gas transmission pipeline inspection;
- (4) Application of Taguchi methods for optimizing the natural gas transmission pipeline inspection tool;

- (5) Finite element modeling of magneto-optic/eddy current imaging of multi-layer aviation geometries, such as second layer radial crack, third layer fastener-to-fastener crack, and circumferential crack;
- (6) Development of the concept of coefficient of skewness for binary MO image analysis;
- (7) Parametric studies on the skewness of binary MO images;
- (8) Development of POD model for image-based NDE systems;
- (9) POD studies with respect to threshold and frequency individually of MOI measurements;
- (10) Application of Taguchi methods for optimizing the operational parameters in MOI;
- (11) Development of Matlab code for the use of algebraic multigrid method in enhancing finite element models;
- (12) Other projects including experiments and/or finite element modeling with user-friendly software interface of differential coil eddy current tubing inspection, magnetic particle inspection, artificial heart valve inspection, etc.

7.2 Future Work

Plans for future work include:

- (1) Development of Fortran and C codes for the use of algebraic multigrid method in enhancing finite element models. Matlab code is effective in quickly implementing algorithms and ideas in hand. However it is difficult to compare the efficiencies of codes in Matlab. So it is necessary to develop Fortran and C codes for both the efficiency investigation and practical application.

(2) **Combination of Taguchi methods with response surface methodology in optimizing the test parameters of NDE systems. The optimal set of design parameters found by Taguchi methods is not truly optimal but near optimal, because the levels of factors under investigation are discrete. The truly optimal set of parameters may not appear on the levels chosen. The response surface methodology is a useful tool in searching the truly optimal parameters by the means of polynomial fitting.**

BIBLIOGRAPHY

- [1] J. H. Hwang and W. Lord, "Finite Element Modeling of Magnetic Field/Defect Interactions", *ASNT Journal of Testing and Evaluation*, Vol. 3, No. 1, pp 21-25, 1975
- [2] J. H. Hwang and W. Lord, "Magnetic Leakage Field Signatures of Material Discontinuities", *Proceedings of the 10th Symposium on NDE*, San Antonio, Texas, 1975
- [3] W. C. Yen, *Finite Element Characterization of Residual Leakage Fields*, MS Thesis, Colorado State University, 1978
- [4] R. B. Thompson and D. O. Thompson, "Ultrasonics in Nondestructive Evaluation", *Proceedings of the IEEE*, Vol. 73, No. 12, Dec 1985
- [5] D. E. Bray and R. K. Stanley, *Nondestructive Evaluation, a Tool for Design, Manufacturing, and Service*, McGraw-Hill, 1989
- [6] W. Lord and D.J. Oswald, "Leaking Field Methods of Defect Detection", *International Journal of Nondestructive Testing*, Vol. 4, 1972, pp. 249-274
- [7] S. Udpa, Y. Sun and N. Nakagawa, *Detecting SLS Failures in BSCC Heart Valves*, Technical Report, Iowa State University, 2000
- [8] J. Jin, *Electromagnetic analysis and design in magnetic resonance imaging*, CRC Press, 1999
- [9] D. Simunic et al, "Analysis of Eddy Currents Originating from Switched Magnetic gradient Fields in Magnetic Resonance Imaging", *Biomedizinische Technik*, 41 (1996), 79-83

- [10] W. Renhart et al, "Application of Eddy Current Formulation to Magnetic Resonance Imaging", *IEEE Transactions on Magnetics*, Vol. 28, No. 2, March 1992
- [11] X. Cai, *Iterative Blind Deconvolution and its Application in Characterization of Eddy Current NDE Signals*, MS Thesis, Iowa State University, 2001
- [12] Y. Sun, T. Ouang, and S. Udpa, "Remote Field Eddy Current Testing: One of the Potential Solutions for Detecting Deeply Embedded Discontinuities in Thick and Multilayer Metallic Structures", *Materials Evaluation*, May 2001
- [13] Y. Sun, T. Ouang, S. Udpa, and Z. Zeng, "Detecting Compressive Residual Stress in Carbon Steel Specimens of Flat Geometries Using the Remote-Field Eddy Current Technique", *Review of Progress in Quantitative Nondestructive Evaluation*. Maine, USA, July 2001
- [14] D. Lovejoy, *Magnetic Particle Inspection – A Practical Guide*, Chapman & Hall, 1993
- [15] L. Cartz, *Nondestructive Testing – Radiography, Ultrasonics, Liquid Penetrant, Magnetic Particle, Eddy Current*, ASM International, 1995
- [16] J. Blitz, *Electrical and Magnetic Methods of Nondestructive Testing*, Adam Hilger, 1991
- [17] Z. Zeng, L. Xuan, L. Udpa and S. S. Udpa, "Modeling of Current Excitation Waveforms for Magnetic Particle Inspection", *Review of Progress in Quantitative Nondestructive Evaluation*, Maine, USA, July 2001
- [18] K. Ishibashi, "Nonlinear Eddy Current Analysis by the Integral Equation Method", *IEEE Transactions on Magnetics*, Vol. 30, No. 5, September 1994

- [19] N. Esposito et al, "Modeling of Three-Dimensional Nonlinear Eddy Current Problems with Conductors in Motion by an Integral Formulation", *IEEE Transactions on Magnetics*, Vol. 32, No. 3, May 1996
- [20] J. R. Bowler, Y. Yoshida and N. Harfield, "Vector-Potential Boundary-Integral Evaluation of Eddy-Current Interaction with a Crack", *IEEE Transactions on Magnetics*, Vol. 33, No. 5, September 1997
- [21] Y. Yoshida and J. R. Bowler, "Vector Potential Integral Formulation for Eddy-Current Probe Response to Cracks", *IEEE Transactions on Magnetics*, Vol. 36, No. 2, March 2000
- [22] Z. You, Z. Jiang, Y. Sun and L. Udpa, "Application of the Substructure-Frontal Method for Repeated Solution of Large Sparse Matrix Equations to Field Problems", *IEEE Transactions on Magnetics*, Vol. 24, No. 1, January 1988
- [23] Y. Sun, G. Zhang and W. Chen, "A Data Base Method for 3D Open Boundary Field Computation", *IEEE Transactions on Magnetics*, Vol. 26, No. 2, March 1990
- [24] W. Chen, G. Zhang, Y. Sun, M. Chen and Y. Zhao, "The Application of the Data Base Method for 3-D Open Boundary Field Computation", *IEEE Transactions on Magnetics*, Vol. 28, No. 2, March 1992
- [25] H. Lin and Y. Sun, "Application of Zoom-In Technique in 3D Remote Field Eddy Current Effect Computation", *IEEE Transactions on Magnetics*, Vol. 26, No. 2, March 1990
- [26] A. Kalimov et al, "Eddy Current Calculation Using Finite Element Method with Boundary conditions of Integral Type" *IEEE Transactions on Magnetics*, Vol. 33, No. 2, March 1997

- [27] Y. E. Ouazzani et al, "Finite Element Modeling of Unbounded Problems: Use of a Geometrical Transformation and Comparison with the Boundary Integral Method", *IEEE Transactions on Magnetics*, Vol. 32, No. 3, May 1996
- [28] Z. Ren et al, "Comparison of Differential Boundary Integral Formulations When Coupled with Finite Elements in Three Dimensions", *IEE Proceedings*, Vol. 135, Pt. A, No. 8, November 1988
- [29] F. Bouillault, "T Ω Formulation by Hybrid F.E.M.-B.I.M. and its Gauges for 3D Electromagnetic Calculations", *IEEE Transactions on Magnetics*, Vol. 28, No. 2, March 1992
- [30] F. Bouillault et al, "Calculation of 3D Eddy Current Problems by an Hybrid T-Method", *IEEE Transactions on Magnetics*, Vol. 26, No. 2, March 1990
- [31] Y. Tanaka, "Three-Dimensional Eddy Current Analysis by the Finite Element Method with Integral Equations Using T- Ω ", *IEEE Transactions on Magnetics*, Vol. 28, No. 2, March 1992
- [32] R. Albanese, "Finite Element Methods for the Solution of 3D Eddy Current Problems", *Advances in Imaging and Electron Physics*, Vol. 102, Academic Press, 1998
- [33] R. Albanese et al, "A Nonlinear Eddy Current Integral Formulation in Terms of a Two-Component Current Density Vector Potential", *IEEE Transactions on Magnetics*, Vol. 32, No. 3, May 1996
- [34] R. Albanese et al, "Analysis of a Transient Nonlinear 3-D Eddy Current Problem with Differential and Integral Methods", *IEEE Transactions on Magnetics*, Vol. 32, No. 3, May 1996

- [35] R. Albanese et al, "A Nonlinear Eddy-Current Integral Formulation for Moving Bodies", *IEEE Transactions on Magnetics*, Vol. 34, No. 5, September 1998
- [36] M. Koizumi et al, "Computational Method of Three Dimensional Eddy Current by Using Volume Integral Equation Method", *IEEE Transactions on Magnetics*, Vol. 27, No. 5, September 1991
- [37] Y. Maréchal, "Some Meshless Methods For Electromagnetic Field Computations", *IEEE Transactions on Magnetics*, Vol. 34, No. 5, September 1998.
- [38] C. Hérault and Y. Maréchal, "Boundary And Interface Conditions In Meshless Methods", *IEEE Transactions on Magnetics*, Vol. 35, No. 3, May 1999.
- [39] S. A. Viana, R. C. Mesquita, "Moving Least Square Reproducing Kernel Method for Electromagnetic Field Computation", *IEEE Transactions on Magnetics*, Vol. 35, No. 3, May 1999.
- [40] V. Čingoski, N. Miyamoto, H. Yamashita, "Element-Free Galerkin Method for Electromagnetic Field Computations", *IEEE Transactions on Magnetics*, Vol. 34, No. 5, September 1998.
- [41] H. Fukutomi, H. Huang, T. Takagi, J. Tani, "Identification of Crack Depths from Eddy Current Testing Signal", *IEEE Transactions on Magnetics*, Vol. 34, No. 5, September 1998.
- [42] T. Belytschko, Y. Kronggauz, D. Organ, M. Fleming, P. Krysl, "Meshless methods: An overview and recent developments", *Comput. Methods Appl. Mech. Engrg.*, 139 (1996) pp. 3-47.
- [43] S. Beissel, T. Belytschko, "Nodal integration of the element-free Galerkin method", *Comput. Methods Appl. Mech. Engrg.*, 139 (1996) pp. 49-74.

- [44] L. W. Cordes, B. Moran, "Treatment of material discontinuity in the Element-Free Galerkin method", *Comput. Methods Appl. Mech. Engrg.*, 139 (1996) pp. 75-89.
- [45] I. Babuška and J. M. Melenk, "The Partition of Unity Method", *Int. J. Num. Meths. Eng.*, 40 (1997) pp.727-758.
- [46] J. M. Melenk et al, "The Partition of Unity Method: Basic Theory and Applications", *Comput. Methods Appl. Mech. Engrg.*, 139 (1996) 289-314
- [47] L. Fraštia, "On Certain Improvements of Element-Free Galerkin Method", *8th International Conference on Numerical Methods in continuum Mechanics*, Sept. 2000
- [48] Y. Krongauz and T. Belytschko, "Enforcement of Essential Boundary Conditions in Meshless Approximations Using Finite Elements", *Comput. Methods Appl. Mech. Engrg.*, 131, (1996) 133--145.
- [49] J. Dolbow and T. Belytschko, "An Intoduction to Programming the Meshless Element Free Galerkin Method", *Archives of Comput. Methods in Engrg.* , Vol 5, No 3, pp. 207-241, 1998
- [50] J. Gosz and W. K. Liu, "Admissible Approximations for Essential Boundary Conditions in the Reproducing Kernel Particle Method", *Computational Mechanics*, Vol. 19, pp. 120-135, 1996
- [51] T. Belytschko et al, "A Three-Dimensional Explicit Element-Free Galerkin Method", *International Journal for Numerical Methods in Fluids*, Vol. 24, pp. 1253-1270, 1997
- [52] T. J. Liszka et al, "hp-Meshless Cloud Method", *Comp. Meth. Appl. Mech. Eng.*, 139, pp. 263-288, 1996

- [53] C. S. Chen, "The Method of Fundamental Solutions and Compactly Supported Radial Basis Functions - A Meshless Approach in 3D Problems", *Boundary Element Methods*, WIT Press, Boston, Southampton, pp 313-322, 1999
- [54] G. J. Wagner and W. K. Liu, "Application of Essential Boundary Conditions in Mesh-Free Methods: A Corrected Collocation Method", *International Journal for Numerical Methods in Engineering*, Vol. 47, pp. 1367-1379, 2000
- [55] X. Zhang et al, "Meshless Methods Based on Collocation with Radial Basis Functions", *Computational Mechanics*, 26, pp. 333-343, 2000
- [56] L. Xuan, Z. Zeng, B. Shanker, L. Udpa, "Meshless Element-Free Galerkin Method in NDT Applications", *Review of Progress in Quantitative Nondestructive Evaluation*, Maine, USA, July 2001
- [57] L. Xuan, Z. Zeng, B. Shanker, L. Udpa, "Development of a Meshless Finite Element Model for NDE Applications", *18th Annual Review of Progress in Applied Computational Electromagnetics*, California, USA, March 2002
- [58] C. A. Balanis, *Advanced Engineering Electromagnetics*, John Wiley & Sons, 1989
- [59] F. P. Andrew, *Computational Methods for Electromagnetics*, IEEE Press, 1998
- [60] R. F. Harrington, "Origin and Development of the Method of Moments for Field Computation", *IEEE Antennas and Propagation Magazine*, 1990
- [61] D. R. Wilton and C. M. Butler, "Effective Methods for Solving Integral and Integro-Differential Equations", *Electromagnetics*, Vol. 1, pp. 289-308, 1981
- [62] S. S. Udpa and W. Lord, "Finite Element Modeling of Residual Magnetic Phenomenon", *International Magnetics Conference*, Boston, April 1980

- [63] W. Lord and R. Palanisamy, "Magnetic Probe Inspection of Steam Generator Tubing", *Materials Evaluation*, Vol. 38, No. 5, pp. 478-485, May 1980
- [64] R. Palanisamy and W. Lord, "Finite Element Analysis of Eddy Current Phenomena", *International Bibliography, Information and Documentation*, Vol.38, No. 10, pp. 901-913, October 1980
- [65] R. Palanisamy and W. Lord, "Finite Element Analysis of Axisymmetric Geometries in Quantitative NDE", *In Review of Progress in Quantitative NDE*, San Diego, July 1979
- [66] N. Ida, *Three Dimensional Finite Element Modeling of Electromagnetic NDT Phenomena*, PhD Dissertation, Colorado State University, 1983
- [67] N. Ida and W. Lord, "3-D Finite Element Prediction of Magnetostatic Leakage Fields", *IEEE Transactions on Magnetics*, pp. 2260-2265, September 1983
- [68] J. Jin, *The Finite Element Method in Electromagnetics*, John Wiley & Sons, 1993
- [69] R. Palanisamy, *Finite Element Modeling of Eddy Current Nondestructive Testing Phenomena*, PhD Dissertation, Colorado State University, 1980
- [70] Y. Zhao and Y. Wang, "Three-Dimensional Finite Element Computation of Electromagnetics for Nondestructive Testing", *Antennas and Propagation Society International Symposium*, Vol. 1, pp. 166 -169, 1996
- [71] T. Nakata et al, "Improvement of the T- Ω Method for 3-D Eddy Current Analysis", *IEEE Transactions on Magnetics*, Vol. 24, No. 1, January 1988
- [72] N. Ida, *A Three Dimensional Computer Code for Eddy Current NDT Application*, *Technical Report*, Colorado State University, 1984
- [73] W. L. Briggs, *A Multigrid Tutorial*, SIAM, Philadelphia, 1987

- [74] S. F. McCormick, *Multigrid Method*, SIAM, Philadelphia, 1987
- [75] C. C. Douglas, "Multigrid Methods in Science and Engineering", *IEEE Computational Science and Engineering*, 1996, pp.55-68
- [76] S. V. Polstyanko et al, "Algebraic Multigrid Method for Solving FEM Matrix Equations for 3D Static Problems", *IEEE Trans. Magn.*, vol. 35, pp. 1183-1186, 1999
- [77] M. Kaltenbacher et al, "Algebraic Multigrid Method for Solving 3D Nonlinear Electrostatic and Magnetostatic Field Problems", *IEEE Trans. Magn.*, vol. 36, pp. 1561-1564, 2000
- [78] D. Lahaye et al, "Algebraic Multigrid for Complex Symmetric Systems", *IEEE Trans. Magn.*, vol. 36, pp. 1535-1538, 2000
- [79] R. Mertens, "An Algebraic Multigrid Method for Solving Very Large Electromagnetic Systems", *IEEE Trans. Magn.*, vol. 34, pp. 3327-3330, 1998
- [80] V. Čingoski et al, "Investigation of the Efficiency of the Multigrid Method for Finite Element Electromagnetic Field Computations Using Nested Meshes", *IEEE Trans. Magn.*, vol. 35, pp. 3751-3753, 1999
- [81] C. Koh et al, "An Adaptive Finite Element Scheme using Multi-grid Method for Magnetostatic Problems", *IEEE Trans. Magn.*, vol. 25, pp. 2959-2961, 1989
- [82] I. Tsukerman, "Fast Finite Element Solvers for Problems with Magnetic Materials", *IEEE Trans. Magn.*, vol. 29, pp. 2365-2367, 1993
- [83] V. Cingoski et al, "Fast Multigrid Solution Method for Nested Edge-Based Finite Element Meshes", *IEEE Trans. Magn.*, vol. 36, pp. 1539-1542, 2000
- [84] M. Schinnerl et al, "Nested Multigrid Methods for the Fast Numerical Computation of 3D Magnetic Fields", *IEEE Trans. Magn.*, vol. 36, pp. 1557-1560, 2000

- [85] L. Stals, "Adaptive Multigrid in Parallel", *Algorithms and Architectures for Parallel Processing*, 1995
- [86] K. Goverdhanam et al, "Applications of Multiresolution Based FDTD Multigrid", *1997 IEEE MTT-S Digest*, pp. 333-336
- [87] K. Goverdhanam et al, "An FDTD Multigrid Based on Multiresolution Analysis", *Antennas and Propagation Society International Symposium, 1996. AP-S Digest*, Vol. 1, pp. 352-355, 1996
- [88] B. Z. Steinberg et al, "On the Use of Wavelet Expansions in the Method of Moments", *IEEE Transactions on Antennas and Propagation*, Vol. 41, No. 5, pp. 610-619, May 1993
- [89] M. Wall, "Modeling of NDT Reliability (POD) and Applying Corrections for Human Factors", *7th European Conference on Non-destructive Testing*, Vol. 3, No. 7, September 1998
- [90] M. Wall et al, "Economic Assessment of Inspection - the Inspection Value Method", *7th European Conference on Non-destructive Testing*, Vol. 3, No. 12, September 1998
- [91] L. Schaefer, "Whole R Considerations for NDE in American Aerospace", *15th World Conference on Non-Destructive Testing*, October 2000
- [92] M. Wall et al, "Worth of Modelling for Assessing the Intrinsic Capability of NDT", *15th World Conference on Non-Destructive Testing*, October 2000
- [93] M. J. Golis, "Application Parameters - A Definition and Their Role in NDE Reliability", *15th World Conference on Non-Destructive Testing*, October 2000
- [94] H. M. Stephens, "NDE Reliability - Human Factors - Basic Considerations", *15th World Conference on Non-Destructive Testing*, October 2000

- [95] P. L. Meyer, *Introductory Probability and Statistical Applications*, Addison-Wesley, 1970
- [96] G. K. Subramanya, *Probability of Detection Model for Magnetostatic Nondestructive Evaluation*, MS Thesis, Iowa State University, 1994
- [97] S. N. Rajesh, L. Udpa and S. S. Udpa, "Numerical model based approach for estimating probability of detection in NDE applications", *IEEE Trans. Magn.*, vol. 29, pp. 1857-1860, March 1993
- [98] S. N. Rajesh, L. Udpa, S. S. Udpa and N. Nakagawa, "Probability of Detection (POD) Models for Eddy Current NDE Methods", *Review of Progress in Quantitative Nondestructive Evaluation*, Vol. 11, pp. 265-272, 1992
- [99] S. N. Rajesh, *Probability of Detection Models for Eddy Current NDE Methods*, MS Thesis, Iowa State University, 1993
- [100] S. N. Rajesh, L. Udpa and S. S. Udpa, "Estimation of Eddy Current Probability of Detection (POD) Using Finite Element Method", *Review of Progress in Quantitative Nondestructive Evaluation*, Vol. 12, pp. 2365-2372, 1993
- [101] J. R. Martinez and A. J. Bahr, "Statistical Detection Model for Eddy-Current Systems", *Review of Progress in Quantitative Nondestructive Evaluation*, Vol. 3A, pp. 499-510, 1994
- [102] P. W. Hovey and A. P. Berens, "Statistical Evaluation of NDE Reliability in the Aerospace Industry", *Review of Progress in Quantitative Nondestructive Evaluation*, Vol. 7B, pp. 1761-1768, 1987

- [103] I. Elshafiey, L. Udpa and S. S. Udpa, "Implementation of Probability of Detection Models for Eddy Current NDE Techniques on Parallel Computers", *Review of Progress in Quantitative Nondestructive Evaluation*, Vol. 13, pp. 2167-2174, 1994
- [104] Z. Zhang, Y. Zhang, L. Udpa and S. S. Udpa, "Probability of detection model for Pipeline inspection", *Review of Progress in Quantitative Nondestructive Evaluation*, Vol. 16, pp. 1307-1314, 1997
- [105] Z. Zeng et al, *Perturbation Analysis and Probability of Detection*, Technical Report, Iowa State University, 2000
- [106] M. Wall, "Modelling of Inspection Reliability", *Engineering Science and Education Journal*, Vol. 6, Issue 2, pp. 63-72, April 1997
- [107] C. Nockemann et al, "How to Treat the Reliability of Defect Detection and Assessment in Nondestructive Testing?", *IEEE 7th SP Workshop on Statistical Signal and Array Processing*, pp. 449-452
- [108] W. Hoppe et al, "Results from the Hidden Corrosion Detection Evaluation on the Automated Corrosion Detection Program – Probability of Detection"
- [109] W. D. Feist et al, "Determination of the POD for High Resolution Eddy Current Inspection on Turbine Disks", *7th European Conference on Non-destructive Testing*, Vol. 3, No. 9, September 1998
- [110] R. Osegueda et al, "Multi-Resolution Methods in Non-Destructive Testing of Aerospace Structures and in Medicine", *Proceedings of the 1999 IEEE International Symposium on Intelligent Control/Intelligent Systems and Semiotics*, Cambridge, MA, September 1999, pp. 207-212

- [111] G. Y. Dymkin, "Systematics of NDE Reliability: A Practical Point of View", *15th World Conference on Non-Destructive Testing*, October 2000
- [112] C. Pairazaman, "Reliability Assurance for Automated Eddy Current Inspection Systems", *15th World Conference on Non-Destructive Testing*, October 2000
- [113] M. Krishna et al, "Fuzzy Logic in Non-Destructive Testing of Aerospace Structures", *IEEE Midwest Symposium on Circuits and Systems*, August 1999
- [114] B. J. T. Morgan, *Elements of Simulation*, Chapman and Hall, 1984
- [115] S. Mandayam, L. Udpa, S. S. Udpa, and W. Lord, "Monte Carlo Methods for Modeling Magnetostatic NDE Phenomena: A Feasibility Study", *IEEE Transactions on Magnetics*, Vol. 32, No. 3, May 1996, pp. 1425-1428
- [116] K. L. Judd, *Numerical Methods in Economics*, MIT Press, 1998, pp. 286-306
- [117] G. Orsak et al, "On the Theory of Importance Sampling Applied to the Analysis of Detection Systems", *IEEE Transactions on Communications*, Vol. 37, No. 4, April 1989, pp. 332-339
- [118] G. C. Orsak, "A Note on Estimating False Alarm Rates Via Importance Sampling", *IEEE Transactions on Communications*, Vol. 41, No. 9, September 1993, pp. 1275-1277
- [119] K. Gerlach, "New Results in Importance Sampling", *IEEE Transactions of Aerospace and Electronic Systems*, Vol. 35, No. 3, July 1999, pp. 917-925
- [120] D. LU and K. Yao, "Importance Sampling Simulation Techniques Applied to Estimating False Alarm Probabilities", *IEEE International Symposium on Circuits and Systems*, 1989, Vol. 1, pp. 598-601

- [121] A. Dekorsy and V. Kühn, "Applicability of Importance Sampling for Rayleigh Fading Mobile Radio Channels", *IEEE 4th International Symposium on Spread Spectrum Techniques and Applications Proceedings*, vol. 1, pp. 224-228, 1996
- [122] J. S. Stadler and S. Roy, "Adaptive Importance Sampling", *IEEE Journal on Selected Areas in Communications*, Vol. 11, No. 3, April 1993, pp. 309-316
- [123] C. G. Bucher, "Adaptive Sampling – An Iterative Fast Monte Carlo Procedure", *Structural Safety*, 5 (1988) 119-126
- [124] R. K. Roy, *A primer on the Taguchi method*, Van Nostrand Reinhold, 1990
- [125] K. Dehnad, *Quality control, robust design, and the Taguchi method*, Pacific Grove, Calif., 1989
- [126] G. S. Peace, *Taguchi methods: a hands-on approach*, Addison-Wesley, 1993
- [127] R. H. Lochner and J. E. Matar, *Designing for quality: an introduction to the best of Taguchi and Western methods of statistical experimental design*, Chapman and Hall, 1990
- [128] V. N. Nair et al, "Taguchi's Parameter Design: A Panel Discussion", *Technometrics*, Vol. 34, No. 2, May 1992
- [129] Z. Zeng et al, *Taguchi Method for Selection of Optimal Sensor Set*, Technical Report, Iowa State University, 2000
- [130] S. E. Kruger et al, "Factorial Design of Experiments Applied to Reliability Assessment in Discontinuity Mapping by Ultrasound", *7th European Conference on Non-destructive Testing*, Vol. 3, No. 11, September 1998

- [131] Z. Zeng, P. Ramuhalli, L. Udpa and S. S. Udpa, "Optimization of Pipeline Inspection Tool using Taguchi Method", *7th International Workshop on Electromagnetic Nondestructive Evaluation*, May 2001
- [132] S. M. Sanchez, "A Robust Design Tutorial", *Proceedings of the 1994 Winter Simulation Conference*, pp. 106-113, 1994
- [133] S. Brisset et al, "Optimization with Experimental Design: An Approach Using Taguchi's Methodology and Finite Element Simulations", *IEEE Transactions on Magnetics*, Vol. 37, No. 5, pp. 3700-3702 September 2001
- [134] M. Chen, "Robust Design for VLSI Process and Device", *International Workshop on Statistical Methodology*, 2001 6yh., pp. 7-16, 2001
- [135] H. Wang, "Application of Taguchi Method to Robust Design of BLDC Motor Performance", *IEEE Transactions on Magnetics*, Vol. 35, No. 5, pp. 3700-3702 September 1999
- [136] H. Fusayasu et al, "Optimization of a Magnetic Actuator with Taguchi Method and Multivariate Analysis Method", *IEEE Transactions on Magnetics*, Vol. 34, No. 4, pp. 2138-2140, July 1998
- [137] S. Chen et al, "The Robust Design Approach for Reducing Cogging Torque in Permanent Magnet Motors", *IEEE Transactions on Magnetics*, Vol. 34, No. 4, pp. 2135-2137, July 1998
- [138] A. R. Khoei et al, "Design Optimisation of Aluminum Recycling Process Using the Taguchi Approach", *Proceedings of the Second International Conference on Intelligent Processing and Manufacturing of Materials*, Vol. 1, pp. 513-518, 1999

- [139] A. Donnarumma et al, "A Fuzzy Design Evaluation Based on Taguchi Quality Approach", *Proceedings of the Second International Conference on Intelligent Processing and Manufacturing of Materials, IPMM'99*, Vol. 1, pp. 185-189, 1999
- [140] K. E. Bullington et al, "A Simple Method for Obtaining Resolution IV Designs for Use with Taguchi's Orthogonal Arrays", *Journal of Quality Technology*, Vol. 22, No. 4, 1990, pp.260-264
- [141] M. Fallon et al, "A Comparison of Taguchi Methods and Response Surface Methodolgy for Optimising a CMOS Process", *IEE Colloquium on Improving the Efficiency on IC Manufacturing Technology*, pp. 8/1-8/4, 1995
- [142] K. Jones et al, "The Comparison of Response Surface and Taguchi Methods for Multiple-Response Optimization Using Simulation", *Thirteenth IEEE/CHMT International Electronics Manufacturing Technology Symposium*, pp. 15-18, 1992
- [143] J. S. Ramberg et al, "Designing Simulation Experiments: Taguchi Methods and Response Surface Metamodels", *Proceedings of the 1991 Winter Simulation Conference*, pp. 167-176, 1991
- [144] X. Gao et al, "Robust Design for Torque Optimization Using Response Surface Methodology", *IEEE Transactions on Magnetics*, Vol. 38, No. 2, pp. 1141-1144, March 2002
- [145] S. Hadjihassan et al, "Model-Based Approach to Robust Design, with Application to Microwave Power Transistors", *IEEE Transactions on Circuits and Systems – I: Fundamental Theory and Applications*, Vol. 49, No. 1, pp. 76-80, January 2002
- [146] P. G. Alotto et al, "Stochastic Algorithms in Electromagnetic Optimization", *IEEE Transactions on Magnetics*, Vol. 34, No. 5, pp. 3674-3684, September 1998

- [147] A. Gottvald, "Global Optimization Methods for Computational Electromagnetics", *IEEE Transactions on Magnetics*, Vol. 28, No. 2, pp. 1537-1540, March 1992
- [148] G. J. Posakony et al, *Assuring the Integrity of Natural Gas Transmission Pipelines*, Technical Report, Gas Research Institute, November 1992
- [149] A. E. Crouch, *In-Line Inspection of Natural Gas Pipelines*, Technical Report, Gas Research Institute, May 1993
- [150] S. Yang, *Finite element modeling of current perturbation method of nondestructive evaluation application*, PhD Thesis, Iowa State University, 2000
- [151] P. Campbell et al, "Three-Dimensional Finite Element Solution of Permanent Magnet Machines", *IEEE Transactions on Magnetics*, Vol. MAG-17, No. 6, November 1981, pp. 2997-2999
- [152] R. H. Vander Heiden et al, "Utilizing Permanent Magnets in Nonlinear Three-Dimensional Finite Element Models", *IEEE Transactions on Magnetics*, Vol. 24, No. 6, November 1988, pp. 2931-2933
- [153] M. A. Alhamadi et al, "Vector Potential 3D-Finite Element Modeling of Magnetic Fields in Permanent Magnet Devices", *IEEE Transactions on Magnetics*, Vol. 27, No. 6, November 1991, pp. 5016-5018
- [154] T. A. Bubenik, J. B. Nestleroth, R. J. Eiber and B. F. Saffell, *Topical Report: Magnetic Flux Leakage (MFL) Technology for Natural Gas Pipeline Inspection*, Gas Research Institute, Nov. 1992, pp.16 and pp. 21
- [155] Z. Zhang, L. Udpa, S. S. Udpa, Y. Sun and J. Si, "An Equivalent Linear Model for Magnetostatic Nondestructive Evaluation", *IEEE Transactions on Magnetics*, Vol. 32, No. 3, May 1996, pp. 718-721

- [156] J. B. Nestleroth and A. E. Crouch, *Variation of Magnetic Properties in Pipeline Steels*, Technical Report, U.S. Department of Transportation, March 1998
- [157] W. R. Sheppard et al, "Low Frequency Eddy Current Array Assessment at the FAA NDI Validation Center", *Materials Evaluation*, July 1995, pp. 844-847
- [158] C. Chen, *Finite Element Modeling of MOI for NDE Applications*, M.S. Thesis, Iowa State University, 2000
- [159] W. C. L. Shih et al, "Aircraft Inspection with the Magneto-Optic/Eddy Current Imager"
- [160] B. L. Fitzpatrick et al, "magneto-Optic/Eddy Current Imaging of Aging Aircraft: A New NDI Technique", *Materials Evaluation*, December 1993, pp. 1402-1407
- [161] L. Xuan et al, "Finite Element Model for MOI Applications Using A-v Formulation", *Review of Progress in Quantitative Nondestructive Evaluation*, Iowa, USA, July 2000
- [162] R. Albanese et al, "A Comparative Study of Finite Element Models for Magneto Optic Imaging Applications", *6th International Workshop on Electromagnetic Nondestructive Evaluation*, Budapest, Hungary, June 2000
- [163] G. Rubinacci, A. Tamburrino, A. Ventre, F. Villone, L. Udpa, L. Xuan, Z. Zeng, "Numerical Simulation of Magneto-Optic Eddy Current Imaging", *8th International Workshop on Electromagnetic Nondestructive Evaluation*, Saarbrücken, Germany, June 2001
- [164] G. Fitzpatrick et al, *Advanced Magneto-Optic/Eddy Current Techniques for Detection of Hidden Corrosion Under Aircraft Skins*, report submitted by Physical Research Inc. to Naval Surface Warfare Center, 1995

- [165] S. B. Vardeman et al, *Basic Engineering Data Collection and Analysis*, Pacific Grove, CA: Brooks/Cole, 2001
- [166] A. C. Shoemaker et al, "Economical Experimentation Methods for Robust Design", *Technometrics*, Vol. 33, No. 4, 1991
- [167] W. J. Welch et al, "Computer Experiments for Quality Control by Parameter Design", *Journal of Quality Technology*, Vol. 22, 1990, pp. 15-22

ACKNOWLEDGMENTS

I would like to express my sincere appreciation to the following people who encouraged and helped me with continual enthusiasm to complete this study.

I would like to express my sincere gratitude to my major professor, Dr. Lalita Udpa, for her guidance and support during my PhD study. Her continuous encouragement, moral and financial support, were of great help to me during my research.

I would like to thank Dr. Satish Udpa, Dr. Yushi Sun and Dr. Balasubramaniam Shanker, for introducing me to the world of non-destructive evaluation and numerical modeling. I am grateful to them for invaluable help during this research.

I would also sincerely thank to Dr. Huaiqing Wu and Dr. Dogandžić Aleksandar for being the committee members of my program and for their advices.

Finally, I would like to thank my beloved parents, brothers and friends for encouragement and help.